CR160127



Axiomatix

# SHUTTLE KU-BAND AND S-BAND COMMUNICATIONS IMPLEMENTATION STUDY

FINAL REPORT

Contract No. NAS 9-15240C

Prepared for

NASA Lyndon B. Johnson Space Center
Houston, Texas 77058

Prepared by

Gaylord K. Huth
Teferi Nessibou
Peter W. Nilsen
Marvin K. Simon
Charles L. Weber

Axiomatix
9841 Airport Boulevard, Suite 912
Los Angeles, California 90045

Axiomatix Report No. R7902-3
February 28, 1979

TABLE OF CONTENTS


| | | Page |
|---|---|---|
| LIST OF TABLES | | iv |
| LIST OF FIGURES | | v |
| 1.0 | INTRODUCTION | 1 |
| 1.1 | Statement of Work | 1 |
| 1.1.1 | Objectives | 1 |
| 1.1.2 | Stipulated Tasks | 1 |
| 1.1.3 | General Approach | 2 |
| 1.1.4 | Continuity With Previous Work | 2 |
| 1.1.5 | Relationship to Parallel Work | 3 |
| 1.2 | Scope of the Final Report | 3 |
| 2.0 | NARROWBAND BENT-PIPE PERFORMANCE | 5 |
| 2.1 | Problem Statement of Narrowband Bent-Pipe Performance | 5 |
| 2.2 | Coherent Tracking of Noise in the Bent-Pipe Channel | 8 |
| 2.2.1 | Coherent References for the Bent-Pipe Signal Format | 9 |
| 2.2.2 | Models for Bent-Pipe Noise | 11 |
| 2.2.3 | Bent-Pipe Analyses Without Desired Signal | 14 |
| 2.2.4 | Statistical Characterization of the Total Equivalent Additive Noise | 18 |
| 2.2.5 | Effective Loop Signal-to-Noise Ratio and Phase Jitter | 20 |
| 2.2.6 | RMS Phase Jitter When the Bent-Pipe Noise is Represented by Model 1 | 21 |
| 2.2.7 | Evaluation of the Coefficients in Phase Jitter When the Bent-Pipe Noise is Modeled as the Random Telegraph Signal, Model 1 | 23 |
| 2.2.8 | RMS Phase Jitter When the Bent-Pipe Noise is Represented by Model 2 | 27 |
| 2.2.9 | RMS Phase Error Computations When the Bent-Pipe Signal is Noise Only | 29 |
| 2.3 | Biphase Costas Loop Tracking of a High SNR Bent-Pipe Signal | 39 |
| 2.4 | Discussion of Possible Alterations and Our Recommendations | 39 |
| 3.0 | EVALUATION OF KU-BAND TDRSS USER CONSTRAINTS | 45 |
| 3.1 | Analysis of Cumulative Effect of 14 Parameters on BER Performance | 47 |
| 3.1.1 | Upper Bound on $\Delta E_b/N_0$ for a Given User Parameter | 47 |

Page

3.1.2 Application of Upper Bound to the Parameters Under Consideration . . . . . 48
3.2 Computations and Discussion of Results . . . . . 55
3.3 Degradation Introduced by the QPSK Modulation for the Subcarrier (Channels 1 and 2) . . . . . 60

4.0 S-BAND TDRSS GROUND STATION FALSE LOCK EVALUATION . . . . 63
4.1 Continuous Loop Model . . . . . 64
4.2 An Alternate Form for the Normalized S-Curve $f(\phi)$ . . . . . 75
4.3 Sampled Data Loop Model . . . . . 77
4.4 Periodicity of False Lock Behavior . . . . . 82
4.5 Comparison with Previous Experimental Results . . . 83

5.0 S-BAND ANTENNA MEASUREMENT . . . . . 86
5.1 Introduction and Statement of Problem . . . . . 86
5.2 General Technical Approach . . . . . 86
5.3 Antenna Data Processing Algorithm . . . . . 92
5.4 Derivation of Antenna Gain Filtering Algorithm . . . . . 94

6.0 S-BAND RFI MEASUREMENT . . . . . 97

7.0 PAYLOAD INTERFACE INTEGRATION . . . . . 104
7.1 Attached Payload Communication . . . . . 104
7.2 Detached Payload Communication . . . . . 110
7.3 Orbiter Avionic Equipment Serving Payloads . . . . . 115
7.3.1 Payload Interogator . . . . . 115
7.3.2 Payload Signal Processor . . . . . 118
7.3.3 Communication Interface Unit . . . . . 120
7.3.4 Ku-Band Signal Processor . . . . . 122
7.3.5 FM Signal Processor . . . . . 129
7.3.6 Multiplexer/Demultiplexer . . . . . 134
7.3.7 PCM Master Unit . . . . . 140
7.3.8 Payload Data Interleaver . . . . . 142
7.3.9 Payload Experiment Recorder . . . . . 145
7.4 Payload Interface Issues . . . . . 146
7.4.1 Payload Interrogator and Payload Signal Processor Interface . . . . . 146
7.4.2 Payload Interrogator and Ku-Band Signal Processor Interface . . . . . 148
7.4.3 Commonality of Payload Signal Processor and Communication Interface Unit Functions . 149

REFERENCES . . . . . 150

## LIST OF TABLES


| | | Page |
|---|---|---|
| 1. | Comparison of TDRSS User Constraints and HAC Specifications with Corresponding Degradations . . . . . | 56 |
| 2. | NASA Command System Parameters . . . . . | 118 |
| 3. | Standard Payload Telemetry Modulation Characteristics . . | 120 |
| 4. | Ku-Band Signal Processor Data Characteristics . . . . . | 124 |
| 5. | S-Band FM Performance Specifications . . . . . | 130 |
| 6. | Input and Output Signal Characteristics of FM-SP Payload Data . . . . . | 133 |
| 7. | Peak-to-RMS Values of Various Waveforms . . . . . | 146 |

LIST OF FIGURES


| | | Page |
|---|---|---|
| 1. | Narrowband Bent-Pipe Test Block Diagram Implemented at NASA-JSC | 6 |
| 2. | Candidate Model of Noise Signal for Bent-Pipe | 10 |
| 3. | Costas Loop for Ku-Band Demodulation of the Bent-Pipe Signal | 15 |
| 4. | Plot of $B_i/2B_N$ Versus $B_iT_1$ When the Phase Tracking Error Approaches Infinity and the Bent-Pipe Signal is Noise Only | 31 |
| 5a. | RMS Phase Error of the Costas Loop When the Bent-Pipe Signal Consists of Model 1 Noise | 33 |
| 5b. | RMS Phase Error of the Costas Loop When the Bent-Pipe Signal Consists of Model 1 Noise | 34 |
| 5c. | RMS Phase Error of the Costas Loop When the Bent-Pipe Signal Consists of Model 1 Noise | 35 |
| 6a. | RMS Phase Error of the Costas Loop When the Bent-Pipe Signal Consists of Model 2 Noise | 36 |
| 6b. | RMS Phase Error of the Costas Loop When the Bent-Pipe Signal Consists of Model 2 Noise | 37 |
| 6c. | RMS Phase Error of the Costas Loop When the Bent-Pipe Signal Consists of Model 2 Noise | 38 |
| 7. | Squaring Loss in a Costas Loop Versus $B_iT_2$ for Various Levels of Signal-to-Noise Ratio | 41 |
| 8. | Block Diagram of the I Channel (Channel 3) With Associated Hardware Parameters | 46 |
| 9. | Variation of Degradation in SNR as a Function of Asymmetry When Data Transition Time Dominates Data Asymmetry | 58 |
| 10. | Variation of Cumulative Degradation in SNR as a Function of Asymmetry When Data Transition Time Dominates Data Asymmetry | 59 |
| 11. | A Continuous-Type Decision-Directed I-Q Loop | 65 |
| 12a. | S-Curve for False Lock at nth Multiple of Half the Data Rate | 71 |
| 12b. | True Lock S-Curve | 71 |
| 13. | A Sampled Data Type Decision-Directed I-Q Loop | 78 |
| 14. | Data-Aided Loop False Lock Ranges for $\delta = 10$ | 84 |
| 15. | Link Relationships for Determination of Shuttle Antenna Gain During OFT | 88 |
| 16. | Information Flow for Gain Pattern Determination of Shuttle Antenna During OFT | 90 |

Page

17. Unprocessed Gain Matrix . . . . . 91

18. Flow Chart for Preliminary Antenna Data Processing Algorithm. . 93

19. TDRSS/Shuttle/RFI Operational Scenario . . . . . 98

20. RFI Test Scenario . . . . . 99

21. Shuttle Visibility at East Germany RFI Location . . . . . 100

22. Shuttle Visibility at Madrid for Simultaneous RFI Visibility for BRM2 . . . . . 101

23. Madrid STDN Elevation Angle During Simultaneous Shuttle Visibility with RFI . . . . . 102

24. East Germany RFI Visibility of Shuttle . . . . . 103

25. Attached Payload Scientific Data Interface . . . . . 105

26. Attached Payload Engineering Data Interface . . . . . 107

27. Attached Payload Caution and Warning Interface . . . . . 109

28. Attached Payload Data Recording Interface . . . . . 111

29. Attached Payload Guidance, Navigation, and Attitude Control Interface . . . . . 112

30. Payload/Orbiter Subsystems and Interfaces . . . . . 113

31. Payload Interrogator Functional Block Diagram . . . . . 116

32. NASA Payload Signal Processor Functional Block Diagram . . . . 119

33. Communication Interface Unit for DOD Payloads . . . . . 121

34. Ku-Band Signal Processor Forward Link Functional Block Diagram. 125

35. Ku-Band Mode 1 Three Channel Modulation . . . . . 126

36. Ku-Band Mode 2 Three Channel Modulation . . . . . 127

37. FM Signal Processor Functional Block Diagram . . . . . 132

38. MDM System Block Diagram . . . . . 135

39. Serial Digital Input/Output Channel Interface . . . . . 136

40. Serial Word Format . . . . . 137

41. Data Code . . . . . 137

Page

42. Data Word Synchronization, Nonvalid Manchester Code . . . . . 138

43. Serial Channel Data Transfer . . . . . 139

44. PCMMU Block Diagram . . . . . 141

45. PDI Block Diagram . . . . . 143

# 1.0 INTRODUCTION

This Final Report summarizes the system implementation studies of the Ku-band radar/communication system and S-band communication system.

## 1.1 Statement of Work

### 1.1.1 Objectives

The overall objective of the effort has been to analyze the interfaces between the Ku-band system and the TDRSS, between the S-band system and the TDRSS, GSTDN and SGLS networks, and between the S-band payload communication equipment and the other Orbiter avionic equipment. The principal activities to accomplish these objectives have been:

(1) Performance analysis of the payload narrowband bent-pipe through the Ku-band communication system.

(2) Performance evaluation of the TDRSS user constraints placed on the S-band and Ku-band communication systems.

(3) Assessment of the Shuttle-unique S-band TDRSS ground station false lock susceptibility.

(4) Development of procedure to make S-band antenna measurements during orbital flight.

(5) Development of procedure to make RFI measurements during orbital flight to assess the performance degradation to the TDRSS S-band communication link.

(6) Analysis of the payload interface integration problem areas.

### 1.1.2 Stipulated Tasks

The contract Statement of Work calls out the following tasks:

"Task #1 - Evaluation of Ku-band System Implementation - The contractor shall evaluate the Orbiter Ku-band system implementation and analyze issues regarding the Ku-band system interfaces with TDRSS. From this evaluation the contractor shall make recommendations concerning the Ku-band system implementation alternatives and design changes to resolve interface problems.

Task #2 - Evaluation of S-band System Implementation - The contractor shall evaluate the Orbiter S-band system implementation and analyze issues regarding the S-band system interfaces with the TDRSS, GSTDN, and SGLS networks. From this evaluation the contractor shall make recommendations concerning S-band system implementation alternatives and design changes to resolve interface problems.

Task #3 - Payload Interface Integration - The contractor shall perform analyses of technical issues related to payload interface integration for the payload S-band communications interfaces including the payload interface with the Payload Data Interleaver. Recommendations concerning resolution of problem areas associated with the Payload interrogator, Payload signal processor, and the payload interleaver and the associated interfaces with payloads, shall be made."

The activities performed to accomplish these tasks are noted in the previous section. Activities (1) and (2) were in response to Task 1, activities (3) through (5) were in response to Task 2, and activity (6) was in response to Task 3.

### 1.1.3 General Approach

The general approach has been to work with cognizant NASA personnel and individuals at the principal prime contractors (Rockwell International for the Orbiter and Western Union for TDRSS) and subcontractors (TRW, Hughes Aircraft Company, Harris, and Motorola) to ascertain directions taken. A vital part of this activity has involved Axiomatix attendance and participation in the regular monthly program reviews and all special meetings. These latter gatherings usually involved detailed discussions on design and specification issues. Apart from attendance at meetings, monthly reviews, and analysis activities, Axiomatix also acted in a technical consulting role to NASA.

Each month, Axiomatix prepared a Monthly Technical Report which contained a brief summary of all relevant technical activity. Many of the Axiomatix in-process analysis activities and results were appended to these reports.

### 1.1.4 Continuity With Previous Work

The activity on the Ku-band and S-band communication systems was a continuation of contracts NAS 9-13467 and NAS 9-15240A, both of which were entitled "Integrated Source and Channel Encoded Digital Communication System Design Study." Also, the activity on NAS 9-13467 and NAS 9-15240A was related to analyses performed to optimize the S-band and Ku-band communication equipment carried out under contract NAS 9-14614, "Study to Investigate and Evaluate Means of Optimizing the Communication Functions."

### 1.1.5 Relationship to Parallel Work

The work performed under the subject contract was strongly interrelated to parallel work. Contract NAS 9-15514A, "Shuttle Orbiter S-Band Communication Equipment Design Evaluation," provided support to critique the design and assess the performance of the individual Orbiter S-band communication equipment. Contract NAS 9-15515A, "Shuttle Orbiter Ku-Band Radar/Communications System Design Evaluation," provided support to critique the design and assess the performance of the Orbiter Ku-band radar/communication equipment. In terms of the payload interface integration task, contract NAS 9-15409B, "Orbiter/IUS Communications Hardware Evaluation," provided support to evaluate the DOD and NASA Inertial Upper Stage (IUS) communication system design, hardware specifications, and interfaces to determine their compatibility with the Orbiter payload communication equipment and the Orbiter operational equipment. Also, contract NAS 9-15240D is the systems contract to identify, evaluate, and make recommendations concerning the functions and interfaces of those Orbiter avionic subsystems which are dedicated to, or play some part in, handling communication signals (telemetry and command) to and from the payloads (spacecraft) that will be carried into orbit by the Shuttle.

## 1.2 Scope of the Final Report

There are six sections following which address the six major activities performed during this study to accomplish the three stipulated tasks.

Section 2.0 describes the narrowband bent-pipe performance and recommends a simple modification for the ground equipment to correct a loss-of-lock tracking problem which has been experimentally observed. The analysis using realistic system parameters determined the cause of the problem and, after exploring various possible alternatives, subsequently resulted in the recommended fix which consists of widening the bandwidth of the arm filters in the 8.5 MHz Costas loop on the ground.

Section 3.0 evaluates the Ku-band TDRSS user constraints and compares them with the HAC specifications. The cumulative degradation effects are analyzed and summarized in tabular form for both cases.

Section 4.0 presents the analysis of the false lock susceptibility of the Shuttle-unique S-band demodulator proposed by Motorola. Because

of the false lock susceptibility found for the hard-limited loop proposed by Motorola, Axiomatix believes the implementation should be reviewed. At the moment it seems that, in the loop proposed by Motorola, there is little impact for not hard-limiting the in-phase channel. Therefore, a better implementation would be to eliminate the hard-limiter, which would leave the first false lock point outside the acquisition sweep range.

Section 5.0 proposes a method of measuring the Shuttle S-band antenna patterns in orbit by statistical means, taking into consideration such factors as Shuttle orientations, distances, and ground station antenna calibrations. A more realistic antenna pattern measurement will result, since the influences of adjacent Shuttle appendages, which are difficult to simulate using mock-ups, will be directly measured under actual orbital conditions.

Section 6.0 outlines a procedure to evaluate the effects of RFI on the TDRSS S-band communication system. Since orbital trajectory analyses indicated that the exposure to RFI from East Germany and Madrid would be less than a few minutes at most, it is recommended that a portable S-band ground transmitter be positioned such that RFI effects can be adequately studied under controlled conditions.

Finally, Section 7.0 describes the Orbiter avionics equipment serving attached and detached payloads. The interrelationships and interfaces between the Orbiter avionic equipment are delineated. Also, the capabilities and requirements of each Orbiter avionic subsystem involved with the payload signal handling functions are presented. After reviewing the interfaces between the payload equipment and the Orbiter avionic equipment, a number of areas of concern were found. The interfaces that still require specification modifications are between the Payload Interrogator and the Payload Signal Processor, between the Payload Interrogator and the Ku-band Signal Processor, and between the DOD Communication Interface Unit and the Orbiter MDM. The details of these areas of concern are presented in Section 7.4.

## 2.0 NARROWBAND BENT-PIPE PERFORMANCE

The performance of the narrowband bent-pipe signal processor is developed. Tests conducted at the NASA-JSC laboratories show that, at certain sets of system parameters, the 8.5 MHz Costas loop on the ground would lose lock. The results of the analysis of this section predict under what conditions loss of lock can be expected.

Heuristically, a Costas loop will not track a balanced QPSK signal. Even though the power split in the bent-pipe mode is 4:1, when the bandwidth of the bent-pipe signal gets too large, the arms of the Costas loop both see the same amount of power. Therefore, in the eyes of the Costas loop, it sees a balanced QPSK signal, and tracking capability is lost.

The results of the analysis presented herein substantiate and predict the loss of lock phenomena observed in the NASA-JSC laboratory tests. With the aid of the analysis, several fixes are proposed to alleviate this problem. All of the fixes have disadvantages, except one which we recommend.

Specifically, we recommend that the bandwidth of the arm filters in the 8.5 MHz Costas loop on the ground be widened to a two-sided noise bandwidth of $B_N = 3.8$ MHz (a 3 dB cutoff frequency of 1.2 MHz). This alteration requires no changes on-board the Orbiter and no additional hardware on the ground, only filter component changes. In addition, in terms of performance, there is a slight increase in squaring loss in the RMS phase error which is negligible. Finally, none of the other fixes considered have any advantages which this fix does not have. Therefore, we recommend this simple alteration to alleviate the loss of lock problem of the 8.5 MHz Costas loop in the narrowband bent-pipe mode.

### 2.1 Problem Statement of Narrowband Bent-Pipe Performance

The signal processing for the narrowband bent-pipe mode of operation of the Ku-band communication system is described. This signal processing for the bent-pipe demodulation problem is presently in the development stage. In order to obtain preliminary design information, a test configuration was assembled at NASA-JSC. A block diagram of this test setup, which simulates the hardware being built for the Ku-band system which pertains to the bent-pipe mode, is shown in Figure 1.

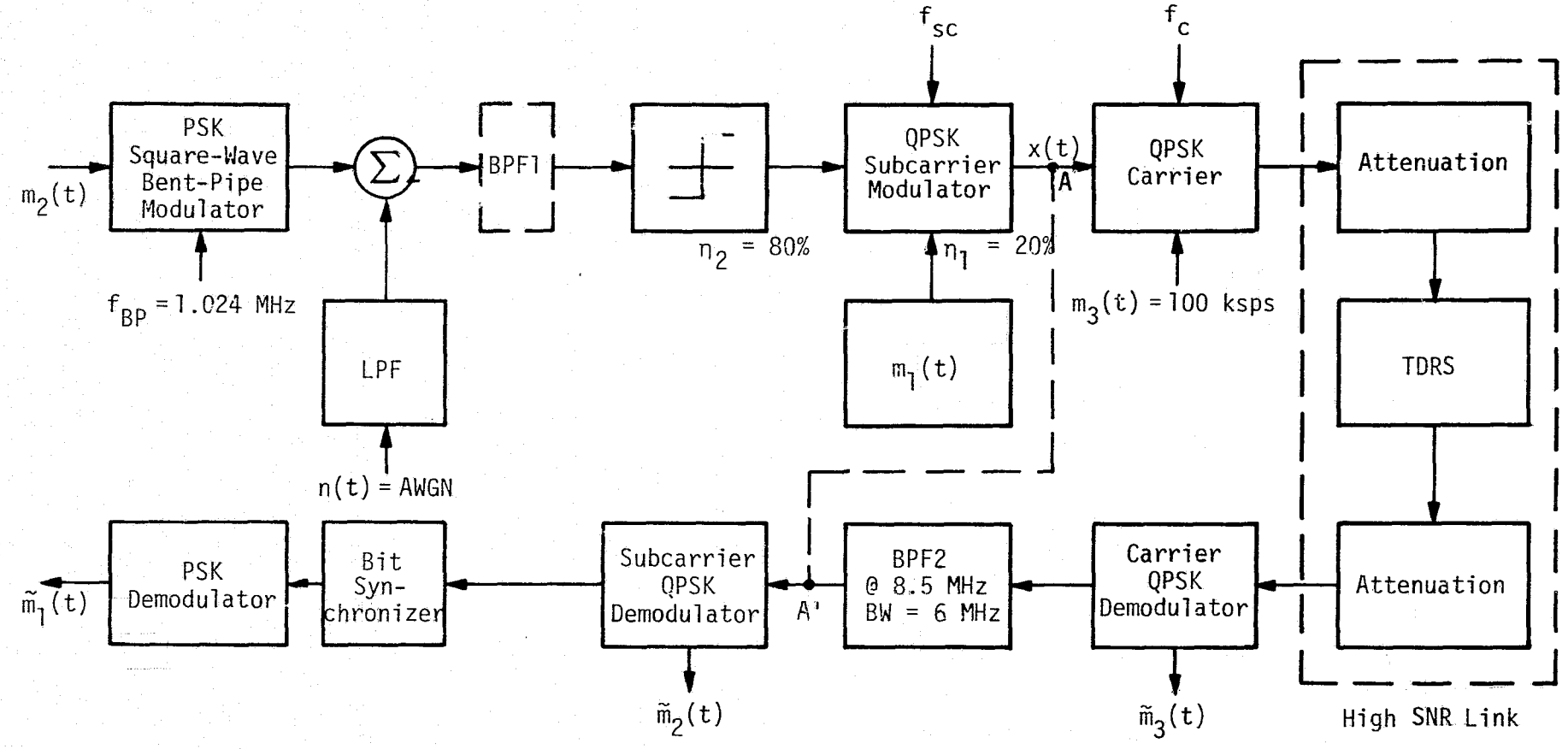


Figure 1. Narrowband Bent-Pipe Test Block Diagram Implemented at NASA-JSC

In the test set-up, it was noted that when the bent-pipe channel consisted of noise only, the Costas loop which is tracking the unbalanced QPSK signal at 8.5 MHz eventually would lose lock, flip 90°, and begin tracking the 192 kbps low-powered signal. When the Costas loop tracks while using as its primary input the 192 kbps signal, loss of lock did not occur at high values of signal-to-noise ratio. At the time, it was thought that this phenomenon was due to equipment malfunctions in the laboratory set-up.

As a result of the conclusions of the analysis in this section (2.0), it is shown that the existence of this phenomenon is not due to equipment malfunction. In fact, the analysis supports and predicts such occurrences. In addition, it is explained why this phenomenon occurs and under what conditions it can happen.

A previous analysis [1] did not support the observations of the laboratory set-up, because the values of the parameters used in [1] were not commensurate with those used in the laboratory nor with those envisioned in the actual bent-pipe communication link. When values are used for parameters which are consistent with those in the laboratory set-up, then the analysis correctly agrees with and predicts the observations in the laboratory.

There is therefore a fundamental problem with the bent-pipe channel. It is necessary that the Costas loop track without ambiguity, even in the absence of a bent-pipe signal, since the lower-powered 192 kbps operations data link is always on. When the bent-pipe signal is off, the Costas loop eventually tracks the 192 kbps signal, because this is what it now observes. The Costas loop always tracks the largest powered signal that it sees.

The sets of system parameters which cause the Costas loop to not track are determined. There is agreement of these results with the tests conducted by NASA-JSC. Several proposed alternatives to system parameters are considered which will avoid this problem, and the best of these is recommended.

We begin by describing the bent-pipe channel in the next section.

## 2.2 Coherent Tracking of Noise in the Bent-Pipe Channel

In this section, the performance of the bent-pipe channel is developed when the signal in the bent-pipe channel consists of noise only. The block diagram of the narrowband bent-pipe test implemented at NASA-JSC is shown in Figure 1. Referring to the figure,

$m_2(t)$ = the desired bent-pipe signal, which is NRZ data (in the high-power channel) with data rate $R_2$, where 16 kbps $\leq R_2 \leq$ 2 Mbps

BPF1 = a bandpass filter which is a candidate fix for the bent-pipe tracking problem that will be subsequently described

$n(t)$ = additive white Gaussian noise

LPF = lowpass filter with a 4.0 MHz bandwidth

$m_1(t)$ = 192 kbps biphase-L data (low power), operations data link

$\eta_i$ = power ratio of the $i$th channel ($i = 1,2$)

$m_3(t)$ = 100 Mbps NRZ data

$\tilde{m}_i(t)$ = the $i$th recovered signal ($i = 1,2,3$)

$f_{BP}$ = bent-pipe signal subcarrier frequency = 1.024 MHz

$f_{sc}$ = lower rate channels QPSK subcarrier frequency = 8.5 MHz

$f_c$ = carrier frequency

BPF2 = bandpass filter with a center frequency of 8.5 MHz and a bandwidth of 6 MHz.

Two levels of unbalanced quadriphase modulation are implemented to modulate the three existing channels. A filtered additive white Gaussian noise is added to the PSK modulated bent-pipe signal, which is then hard-limited and QPSK modulated with $m_1(t)$ on a subcarrier $f_{sc}$. The combined signal, which models the bent-pipe waveform received on the Orbiter, is then QPSK modulated with $m_3(t)$ on a carrier $f_c$ and passed through a high SNR link. The link is simulated via two attenuators and a TDRS nonlinearity simulation block. The demodulation is performed using two Costas loops to recover the carrier ($f_c$) and the subcarrier ($f_{sc}$) before bit synchronization and recovery of the bent-pipe subcarrier takes place.

In order to obtain a direct evaluation of the effects of the bent-pipe signal, the block diagram of Figure 1 is simplified and the bent-pipe signal processing is isolated by eliminating both the high rate channel $m_3(t)$ and the RF channel. This is achieved by connecting points A and A' in Figure 1. Since it is believed that the high rate channel $m_3(t)$ has little effect on the performance of the subcarrier demodulation and that

the existing RF channel is a high SNR channel, this step will greatly simplify and isolate the bent-pipe signal processing for analysis. It will also simplify initial laboratory testing and eliminate any additional hardware complications without greatly disturbing the circuit performance.

### 2.2.1 Coherent References for the Bent-Pipe Signal Format

One of the key issues regarding the bent-pipe channel Ku-band return link is the generation of a coherent reference. This is the case both when the bent-pipe signal is present and when it is absent. In this section, we concentrate on those periods of time when the desired bent-pipe signal is absent. In particular, a conventional Costas loop is used for tracking of the unbalanced quadriphase modulation consisting of 192 kbps biphase data (operations data link) on the low power (20%) channel and the bent-pipe signal on the high power (80%) channel. As a worst-case, the loop is required to provide a coherent reference for tracking when the desired bent-pipe signal is absent, in which case the bent-pipe channel input consists of noise only. When this is the case, it is still desired to obtain a coherent reference. Specifically, the bent-pipe is assigned one channel of the QPSK signal on the 8.5 MHz subcarrier.

When the bent-pipe mode is operating, the high power channel is processed by a hard-limiter before entering the QPSK modulator. The performance of the bent-pipe channel with signal present has recently been determined [2]. The bent-pipe signal was assumed to be either NRZ or biphase-L. The bent-pipe signal processing consisted of two candidates: (1) linear BPF and (2) linear BPF followed by a hard-limiter. The two cases performed similarly, therefore justifying the use of the hard-limiter for the purpose of controlling signal strength. It was also shown that (1) the RMS tracking error increases as the data rate in the bent-pipe channel increases and (2) the RMS tracking error increases as the SNR in the bent-pipe channel decreases.

The QPSK signal which includes the bent-pipe (see Figure 1) is of the form

$$x(t) = \sqrt{2P_1}\, m_1(t) \cos \Phi(t) + \sqrt{2P_2}\, m_2(t) \sin \Phi(t), \qquad (1)$$

where $\Phi(t) = \omega_0 t + \theta(t)$, and $P_i$ $(i = 1,2)$ is the average power in Channels 1 and 2, respectively. $\theta(t)$ represents any existing doppler frequency shift, oscillator instabilities, and an arbitrary phase reference $\theta_0$. The low

powered signal is $m_1(t)$, which is biphase-L at 192 kbps. The high powered signal is modeled as white Gaussian noise passed through an LPF and then a hard-limiter, as shown in Figure 2. The LPF is assumed to be first-order Butterworth (RC) with noise bandwidth of approximately 4 MHz.

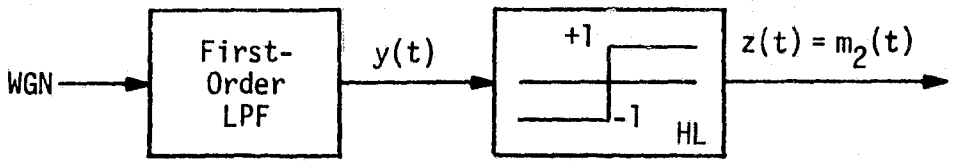


Figure 2. Candidate Model of Noise Signal for Bent-Pipe

When the bent-pipe channel noise is filtered and hard-limited, it appears to the tracking loop as a digital (binary) "data" waveform on the high power channel which differs from a true data waveform in that its zero crossings occur randomly rather than uniformly distributed. The average rate of zero crossings is related to the filtered noise bandwidth. More important than this difference, however, is the fact that the two have different autocorrelation functions. In fact, insofar as determining loop tracking performance, only the autocorrelation function of the high power channel "data" waveform is needed, irrespective of whether this waveform corresponds to true data or hard-limited filtered noise or even, for that matter, hard-limited filtered bent-pipe signal plus noise.

When such a model is employed for the resulting bent-pipe signal in Figure 2, it can be shown [3] that the autocorrelation function of $m_2(t)$ is equal to

$$R_x(\tau) = \frac{2}{\pi} \sin^{-1}\left[\frac{R_y(\tau)}{R_y(0)}\right], \qquad (2)$$

where $R_x(\tau)$ is the autocorrelation function of the process $x(t)$ at the output of the LPF.

An alternate model for $m_2(t)$ is to assume that it is a random telegraph signal. The advantages and disadvantages of both models are developed and discussed in the next section. With either model of $m_2(t)$,

it will be shown that the error signal in the Costas loop has a spectral component at DC which is proportional to the difference in power of $m_2(t)$ and $m_1(t)$. It is also proportional to the sine of twice the phase error, namely, sin $[2\phi(t)]$, where $\phi(t)$ is the difference between the received signal phase and its estimate in the tracking loop.

### 2.2.2 Models for Bent-Pipe Noise

Two different models are considered for the noise signal in the bent-pipe. In either case, the resulting signal takes on only the values of ±1, as shown in Figure 2.

Model 1 - Random Telegraph Model

In this model, we assume the process changes from +1 to -1, and vice versa, at random points in time which are controlled by the Poisson process. For the Poisson process, the probability of k events in $t_e$ sec is given by

$$P[k \text{ in } t_e] = \frac{[\lambda t_e]^k}{k!} \exp(-\lambda t_e) . \tag{3}$$

Whenever an event occurs, the noise changes value. The result is the random telegraph signal [4], which has an autocorrelation function given by

$$R_{m_2}(\tau) = \exp(-2\lambda|\tau|) , \tag{4}$$

where $\lambda$ in (4) is equal to $\lambda$ in (3), which is the average number of events per unit time. The corresponding power spectral density is

$$S_{m_2}(f) = \frac{4\lambda}{4\lambda^2 + (2\pi f)^2} = \frac{1}{\lambda[1 + (\pi f/\lambda)^2]} . \tag{5}$$

This has the same form as white noise through a first-order filter, although the sample waveforms from the two processes do not resemble each other at all. The one-sided noise bandwidth of the random telegraph signal (including hard-limiting) is $B_{N1} = \lambda/2$, where "1" represents Model 1.

Model 2 - Hard-Limited Gaussian Model

This model consists of the one shown in Figure 2. In [3], for example, it is shown that the autocorrelation function of the output of a hard-limiter can be expressed in terms of the autocorrelation at the input, namely,

$$R_{m_2}(\tau) = \frac{2}{\pi} \sin^{-1}\left[\frac{R_y(\tau)}{R_y(0)}\right], \tag{6}$$

when the input is Gaussian.

The normalized autocorrelation function of $y(t)$, $\rho_y(\tau)$, is obtained from passing white noise through a lowpass filter (LPF), as shown in Figure 2. The transfer function of the LPF is assumed to be first-order Butterworth, so that

$$F(j2\pi f) = \frac{1}{1 + j(f/f_3)}, \tag{7}$$

where $f_3$ is the 3 dB cutoff frequency.

The one-sided noise bandwidth, $B_{Ny}$, before the hard-limiter is equal to

$$B_{Ny} = \frac{\pi}{2} f_{32}, \tag{8}$$

where the "2" represents Model 2. The normalized autocorrelation function is then given by

$$\rho_y(\tau) \triangleq \frac{R_y(\tau)}{R_y(0)} = \exp(-\alpha|\tau|), \tag{9}$$

when

$$\alpha = 2\pi f_{32} = 4B_{Ny}. \tag{10}$$

In some of the computations which follow, it is desirable to employ an approximation to $R_{m_2}(\tau)$ in (6) which is more tractable. For this, we consider the approximation

$$R_{m_2}(\tau) \approx \exp(-a|\tau|), \tag{11}$$

where "a" is chosen to be the best least-squares fit. This is actually the least-squares fit of the random telegraph autocorrelation function to that of Model 2. The mean square error between the two is given by

$$\varepsilon^2_{\min} = \min_a \int_0^\infty \left[\frac{2}{\pi} \sin^{-1} \left[\exp(-\alpha\tau)\right] - \exp(-a\tau)\right]^2 d\tau \,. \tag{12}$$

After simplification, we obtain

$$\varepsilon^2_{\min} = \min_a \left\{\frac{1}{2a} - \frac{2}{a}\left[1 - \frac{\left(\frac{a}{\alpha} - 1\right)\Gamma\left(\frac{\frac{a}{\alpha} - 1}{2}\right)}{2\sqrt{\pi}\,\Gamma\left(\frac{a}{2\alpha} + 1\right)}\right] + \frac{4}{\pi^2}\int_0^\infty \left[\sin^{-1}\left(\exp(-\alpha\tau)\right)\right]^2 d\tau\right\} . \tag{13}$$

Letting $\eta = a/\alpha$, then for a given value of $B_{Ny}$, $\varepsilon^2$ is minimized by minimizing its first two terms. (Note: the third term in $\varepsilon^2$ is always positive.) Thus, we desire the solution of

$$f(\eta) = \min_\eta \left\{\frac{1}{\eta}\left[-\frac{3}{2} + \frac{(\eta - 1)\,\Gamma\left(\frac{\eta - 1}{2}\right)}{\sqrt{\pi}\,\Gamma\left(\frac{\eta + 2}{2}\right)}\right]\right\} . \tag{14}$$

Since (14) is transcendental, it must be solved iteratively, with the solution being* $\eta = 1.13$, or $a = 1.13\,\alpha = 1.13\,(4\,B_{Ny})$.

Therefore, we can approximate $R_{m_2}(\tau)$ for Model 2 by

$$R_{m_2}(\tau) \approx \exp(-a|\tau|) \,, \tag{15}$$

where $a = 1.13\alpha = (1.13)(4B_{Ny})$.

The corresponding approximate power spectral density for Model 2 is given by

$$S_{m_2}(f) = \frac{2a}{a^2 + (2\pi f)^2} \tag{16a}$$

*If $\sin^{-1}(\cdot)$ is expanded in a power series and the first two terms are normalized and used to obtain the least-squares fit, for an approximation of the form in (11), the result is $\eta = 1.12$, which is negligibly different from that shown above using the exact representation of $R_{m_2}(\tau)$.

or

$$S_{m_2}(f) = \frac{1}{(2.26\,B_{Ny})\left[1+\left(\frac{\pi}{2.26}\right)^2\left(\frac{f}{B_{Ny}}\right)^2\right]} . \tag{16b}$$

When the approximate PSD obtained for Model 2 in (16) is compared to that obtained for Model 1 in (5), it is noted that they are identical if we set

$$2B_{N1} = \lambda = 2.26\,B_{Ny} . \tag{17}$$

The 3 dB bandwidth and the one-sided noise PSD, $B_{N2}$, for the approximation of Model 2 are given by [from (16)]

$$f_{32} = \frac{2.26}{\pi} B_{Ny} = \frac{2B_{N2}}{\pi} . \tag{18}$$

Equivalently stated, when (17) is satisfied, the 3 dB cutoff frequencies and the noise bandwidths of the noise process, $m_2(t)$, are identical for both models.

The exact representation, as well as the approximations of the second-order statistics of both models, will be used in the development which follows. Alternate descriptions of the output signal and noise statistics of the bent-pipe payload processor are given by [5].

### 2.2.3 Bent-Pipe Analyses Without Desired Signal

When the bent-pipe channel is being used, whether or not a bent-pipe signal is present, a coherent reference must be maintained in the Costas loop in Figure 3 so that the 192 kbps low power (20%) signal (operations data link) can be extracted.

In order to obtain a preliminary assessment of the tracking capability of the Costas loop when the bent-pipe signal consists of noise only, the additive channel noise, $n_i(t)$, in Figure 3 is assumed to be zero. This is a reasonable assumption since that link has a high signal-to-noise ratio. The development in this section is independent of the choice of model for the noise in the bent-pipe channel. The received signal into the Costas loop, $x(t)$, is then given by (1) and is demodulated by the quadrature reference signals:

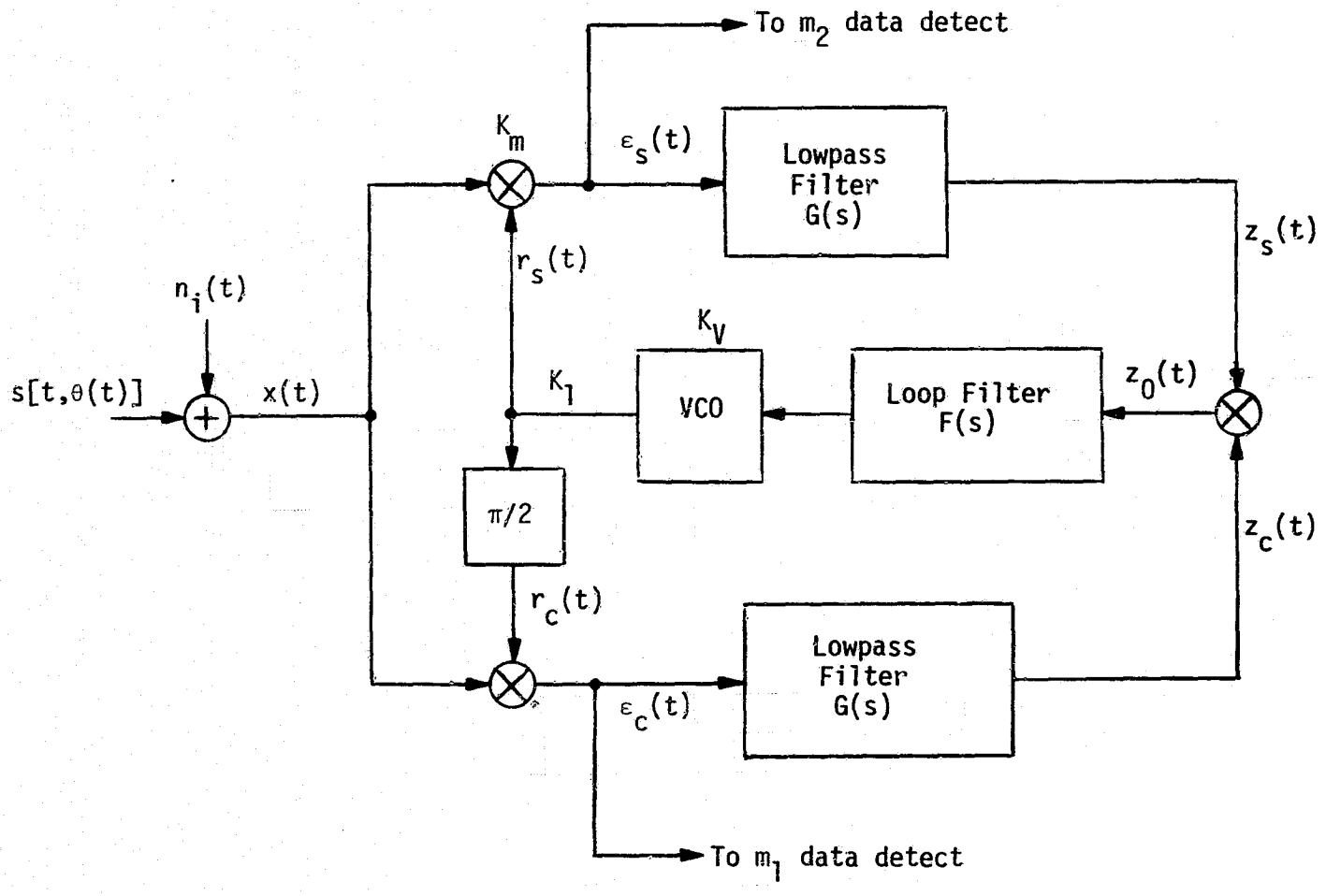


Figure 3. Costas Loop for Ku-Band Demodulation of the Bent-Pipe Signal

$$r_s(t) = \sqrt{2}\, K_1 \sin \hat{\Phi}(t)$$

$$r_c(t) = \sqrt{2}\, K_1 \cos \hat{\Phi}(t)\ ; \tag{19}$$

where $\hat{\Phi}(t) = \omega_0(t) + \hat{\theta}_0(t)$,

and $\phi(t) \triangleq \theta_0(t) - \hat{\theta}_0(t)$ is the loop phase error. (20)

The following development is similar to that in [6]. The corresponding phase detector outputs, after ignoring second-order harmonic terms, are given by

$$\varepsilon_s(t) = K_m x(t)\, r_s(t)$$

$$= K_1 K_m \left[\sqrt{P_2}\, m_2(t) \cos \phi(t) - \sqrt{P_1}\, m_1(t) \cos \phi(t)\right] \tag{21a}$$

and

$$\varepsilon_c(t) = K_m x(t)\, r_c(t)$$

$$= K_1 K_m \left[\sqrt{P_2}\, m_2(t) \sin \phi(t) + \sqrt{P_1}\, m_1(t) \cos \phi(t)\right]. \tag{21b}$$

After the signals $\varepsilon_s(t)$ and $\varepsilon_c(t)$ are lowpass filtered by the arm filters G(s), these signals become, respectively,

$$z_s(t) = G(p)\, \varepsilon_s(t)$$

$$= K_1 K_m \left[\sqrt{P_2}\, \hat{m}_2(t) \cos \phi(t) - \sqrt{P_1}\, \hat{m}_1(t) \sin \phi(t)\right] \tag{22a}$$

and

$$z_c(t) = G(p)\, \varepsilon_c(t)$$

$$= K_1 K_m \left[\sqrt{P_2}\, \hat{m}_2(t) \sin \phi(t) + \sqrt{P_1}\, \hat{m}_1(t) \cos \phi(t)\right], \tag{22b}$$

where the "hats" denote lowpass filtering of the corresponding signals by G(p), i.e.,

$$\hat{m}_i(t) \triangleq G(p)\, m_i(t)\ ; \quad i = 1,2. \tag{23}$$

The output of the third multiplier, which is the loop phase detector, is the dynamic error signal

$$z_0(t) = z_s(t)\, z_c(t)$$

$$= \frac{K_1^2 K_m^2}{2}\left\{\left[P_2(\hat{m}_2(t))^2 - P_1(\hat{m}_1(t))^2\right]\sin(2\phi(t)) + 2\sqrt{P_1 P_2}\,\hat{m}_1(t)\,\hat{m}_2(t)\cos(2\phi(t))\right\} \tag{24}$$

The instantaneous frequency of the VCO output is related to $z_0(t)$ by

$$\frac{d\hat{\Phi}(t)}{dt} = K_v[F(p)\, z_0(t)] + \omega_0 . \tag{25}$$

As a result, the stochastic integro-differential equation describing the loop operation becomes

$$2\frac{d\phi(t)}{dt} = 2\Omega_0 - KF(p)\left\{\left[P_2(\hat{m}_2(t))^2 - P_1(\hat{m}_1(t))^2\right]\sin(2\phi(t)) + 2\sqrt{P_1 P_2}\,\hat{m}_1(t)\,\hat{m}_2(t)\cos(2\phi(t))\right\}, \tag{26}$$

where $\Omega_0 = \omega_{rec} - \omega_{VCO}$ is the difference between the received carrier frequency and the VCO rest frequency in rad/sec, and

$$K = K_v K_1^2 K_m^2 \tag{27}$$

is the equivalent loop gain. Inspection of (27) indicates that any imbalance in the arm gains of the Costas loop is not a problem. The effect is only to vary the overall equivalent loop gain K.

It is convenient in problems of this nature to decompose each of the signal terms $m_i(t)$; $i = 1,2$, in (26) into its mean value plus the variation about the mean, i.e.,

$$[\hat{m}_k(t)]^2 = \left\langle E\left\{[\hat{m}_k(t)]^2\right\}\right\rangle + [\hat{m}_k(t)]^2 - \left\langle E\left\{[\hat{m}_k(t)]^2\right\}\right\rangle; \quad k = 1,2 \tag{28}$$

where E denotes ensemble averaging and $\langle\ \rangle$ denotes time averaging. The additional time averaging is necessary for $m_2(t)$, since it is a cyclostationary process [7]. It is not necessary for $m_2(t)$, since we have

assumed it is a stationary noise process. It can be shown directly that

$$\left\langle E\left\{[m_k(t)]^2\right\}\right\rangle \triangleq D_k = \int_{-\infty}^{\infty} S_{m_k}(f)\,|G(j2\pi f)|^2\,df\,; \quad k=1,2\,. \tag{29}$$

Also, since $m_1(t)$ and $m_2(t)$ are independent,

$$E[\hat{m}_1(t)\,\hat{m}_2(t)] = 0\,. \tag{30}$$

In (29), $S_{m_k}(f)$ denotes the power spectral density of $m_k(t)$, $k=1,2$, and $|G(j2\pi f)|^2$ is the magnitude squared of the arm filter transfer function. Rewriting (26) using the above decompositions, we obtain

$$2\,\frac{d\phi(t)}{dt} = 2\Omega_0 - KF(p)\left\{(P_2D_2 - P_1D_1)\,\sin\,(2\phi(t)) + n_e(t)\right\}\,, \tag{31}$$

where the total equivalent additive noise $n_e(t,\phi)$ is given by

$$n_e(t,\phi) = [P_2\,n_2(t) - P_1\,n_1(t)]\,\sin\,(2\phi(t)) + 2\sqrt{P_1P_2}\,n_{12}(t)\,\cos\,(2\phi(t))\,. \tag{32}$$

The self-noise terms $n_k(t)$, $k=1,2$, and the cross-modulation noise $n_{12}(t)$ are defined by

$$n_k(t) \triangleq [\hat{m}_k(t)]^2 - \left\langle E\left\{[\hat{m}_k(t)]^2\right\}\right\rangle; \quad k=1,2 \tag{33}$$

and

$$n_{12}(t) \triangleq \hat{m}_1(t)\,\hat{m}_2(t)\,. \tag{34}$$

### 2.2.4 Statistical Characterization of the Total Equivalent Additive Noise

The self-noise process in (33) and the cross-modulation noise process in (34) all have zero mean and only a continuous component of power spectral density. Since the bandwidth of these processes is very wide with respect to the loop bandwidth, it is sufficient to find only the power spectral density at the origin for each one which, when multiplied by the loop bandwidth, gives the contribution of the total noise power of that modulation component. From (32), the autocorrelation function of $n_e(t,\phi)$ is given by

$$R_e(\tau,\phi) \triangleq \left\langle E\left[n_e(t,\phi)\, n_e(t+\tau,\phi)\right]\right\rangle$$

$$= \left[P_1^2 R_{n_1}(\tau) + P_2^2 R_{n_2}(\tau)\right][\sin(2\phi)]^2 + 4P_1P_2R_{n_{12}}(\tau)[\cos(2\phi)]^2 , \tag{35}$$

where $$R_{n_k}(\tau) = \left\langle E\left[n_k(t)\, n_k(t+\tau)\right]\right\rangle ; \qquad k = 1,2 , \tag{36}$$

and $$R_{n_{12}}(\tau) = \left\langle E\left[n_{12}(t)\, n_{12}(t+\tau)\right]\right\rangle = R_{\hat{m}_1}(\tau)\, R_{\hat{m}_2}(\tau) . \tag{37}$$

In (37), the autocorrelation functions $R_{\hat{m}_k}(\tau)$, $k = 1,2$, are given by

$$R_{\hat{m}_k}(\tau) = \int_{-\infty}^{\infty} S_{m_k}(f)\, |G(j2\pi f)|^2 \exp(j2\pi f\tau)\, df ; \qquad k = 1,2 . \tag{38}$$

The equivalent one-sided noise power spectral density at the origin of $n_e(t,\phi)$ is then equal to

$$N_e(\phi) = 2\int_{-\infty}^{\infty} R_e(\tau,\phi)\, d\tau$$

$$= 2\left[P_1^2 S_{n_1}(0) + P_2^2 S_{n_2}(0)\right][\sin(2\phi)]^2 + 8P_1P_2S_{n_{12}}(0)\cos^2(2\phi) . \tag{39}$$

The first term in (39) is the self-noise term which can be ignored with negligible error [8], particularly when the phase error is small. When $\phi$ is small, we upper-bound the $\cos^2(2\phi)$ factor by unity in the second term; therefore,

$$N_e(\phi) = 8P_1P_2D_{12} , \tag{40}$$

where

$$D_{12} \triangleq S_{m_{12}}(0) = S_{\hat{m}_1}(f) * S_{\hat{m}_2}(f)\Big|_{f=0}$$

$$= \int_{-\infty}^{\infty} S_{m_1}(f)\, S_{m_2}(f)\, |G(j2\pi f)|^4\, df . \tag{41}$$

### 2.2.5 Effective Loop Signal-to-Noise Ratio and Phase Jitter

From the stochastic integro-differential equation of operation given in (31), we can see that the effective loop signal-to-noise ratio [9] is given by

$$\rho_e = \frac{[P_2 D_2 - P_1 D_1]^2}{N_e B_L}, \tag{42}$$

where $B_L$ is the single-sided noise bandwidth of the linearized tracking loop. The variance of the phase jitter is therefore given by [9]:

$$\sigma_{2\phi}^2 = \rho_e^{-1} \ (\text{rad})^2 \tag{43}$$

or, equivalently,

$$\sigma_\phi^2 = \frac{1}{4}\sigma_{2\phi}^2 = \frac{1}{4\rho_e} \ (\text{rad})^2 . \tag{44}$$

Substituting (40) and (42) into (44), the RMS phase jitter can be expressed as

$$\sigma_\phi = \frac{\sqrt{2}\ \sqrt{D_{12}}\ \sqrt{B_L}}{|\sqrt{P_2/P_1}\ D_2 - \sqrt{P_1/P_2}\ D_1|} \ (\text{rad}) . \tag{45}$$

A normalized RMS phase jitter can also be expressed as

$$\frac{\sigma_\phi}{\sqrt{B_L}} = \frac{\sqrt{2}\ \sqrt{D_{12}}}{|\sqrt{P_2/P_1}\ D_2 - \sqrt{P_1/P_2}\ D_1|} \ (\text{rad}/\sqrt{\text{Hz}}) . \tag{46}$$

In (46), the terms $D_1$, $D_2$ and $D_{12}$ are dependent on the data format and the arm filters type. This result is general in that the modulation and noise in x(t) (Figure 3) affect the evaluation of $D_1$, $D_2$ and $D_{12}$ but do not affect the basic structure of (45) and (46). Only a cursory examination of the normalized RMS phase jitter performance prediction given by (46) indicates that there may be need for concern. The

denominator of (46) consists of the absolute value terms. Clearly, as the values of these two terms approach each other, the Costas loop cannot be expected to adequately provide a satisfactory coherent reference signal.

Heuristically, this result is not surprising, since a Costas loop will not track a balanced QPSK waveform. Equivalently stated, when the denominator in (46) goes to zero, the power in the error signal being processed into the Costas loop also goes to zero. Alternatively, when the denominator in (45) goes to zero, the signal powers in the arms of the Costas loop are equal.

In the next section, specific examples relevant to the Shuttle Ku-band subsystem are investigated, wherein the values of the two terms in the denominator do indeed approach each other.

### 2.2.6 RMS Phase Jitter When the Bent-Pipe Noise is Represented by Model 1

The general result developed in the previous section for RMS phase error is applied to the specific case where the bent-pipe noise is modeled as the random telegraph signal.

In particular, the bent-pipe example consists of:

(a) $m_1(t)$ = 192 kbps biphase-L data (operations data link),

and (b) $m_2(t)$ = the random telegraph signal with parameter $\lambda$ discussed in Model 1 in Section 2.2.2.

The power spectral density of $m_1(t)$ is equal to

$$S_1(f) = T_1 \frac{\sin^4(\pi f T_1/2)}{(\pi f T_1/2)^2} . \tag{47}$$

Assume further that the arm filters are first-order Butterworth (RC) filters with transfer function

$$G(j2\pi f) = \frac{1}{1 + j(\frac{f}{f_3})} , \tag{48}$$

where $f_3 = (1/\pi)B_i$ is the one-sided 3 dB bandwidth and $B_i$ is the two-sided noise bandwidth. The factor $D_1$ in (29) is then given by

$$D_1 = D_1(\text{biphase-L}) = \int_{-\infty}^{\infty} S_{m_1}(f) \, |G(j2\pi f)|^2 \, df \tag{49a}$$

or $$D_1 = \int_{-\infty}^{\infty} \left[\frac{T_1 \sin^4(\pi f T_1/2)}{(\pi f T_1/2)^2}\right]\left[\frac{1}{1+(\frac{f}{f_3})^2}\right] df . \quad (49b)$$

It is shown in the next section that

$$D_1(\text{biphase-L}) = 1 - (2B_i T_1)^{-1}[3 - 4\exp(-B_i T_1) + \exp(-2B_i T_1)] . \quad (50)$$

The power spectral density of the noise process $m_2(t)$ is developed in Section 2.2.2, where it is concluded that

$$S_{m_2}(f) = \lambda^{-1}[1+(\frac{\pi f}{\lambda})^2]^{-1} , \quad (51)$$

where $\lambda$ is the average number of zero crossings of the random telegraph signal per unit time, and $B_{NR} \triangleq \lambda/2$ is its one-sided noise bandwidth. From (29), therefore,

$$D_2 = \int_{-\infty}^{\infty} S_{m_2}(f)\,|G(j2\pi f)|^2\, df$$

$$= \int_{-\infty}^{\infty} \lambda^{-1}\left[1+(\frac{\pi f}{\lambda})^2\right]^{-1}\left[1+(\frac{f}{f_3})^2\right]^{-1} df . \quad (52)$$

This can be integrated via partial fraction expansion:

$$D_2 = \frac{\frac{\pi f_3}{\lambda}}{1+\frac{\pi f_3}{\lambda}} = \frac{\frac{1}{2}\left(\frac{B_i}{B_{N1}}\right)}{1+\frac{1}{2}\left(\frac{B_i}{B_{N1}}\right)} . \quad (53)$$

The remaining coefficient is

$$D_{12} = \int_{-\infty}^{\infty} S_{m_1}(f)\, S_{m_2}(f)\,|G(j2\pi f)|^4\, df , \quad (54)$$

which, in this case, is given by

$$D_{12} = \int_{-\infty}^{\infty} \left[\frac{T_1 \sin^4(\pi f T_1/2)}{(\pi f T_1/2)^2}\right]\left[\frac{1}{\lambda\left(1+(\frac{\pi f}{\lambda})^2\right)}\right]\left[\frac{1}{1+(\frac{f}{f_3})^2}\right]^2 df . \quad (55)$$

This integral is evaluated in the next section. We have that

$$D_{12} = \frac{1}{2B_{NR}}\left\{\frac{1}{1-\left(\frac{B_i}{2B_{NR}}\right)^2}\left\{1-\frac{1}{4B_iT_1}[9-4(3+B_iT_1)\exp(-B_iT_1)+(3+2B_iT_1)\exp(-2B_iT_1)]\right\}\right.$$

$$-\frac{1}{\left(\left(\frac{2B_{NR}}{B_i}\right)-\frac{B_i}{2B_{NR}}\right)^2}\left\{1-\frac{1}{2B_iT_1}[3-4\exp(-B_iT_1)+\exp(-2B_iT_1)]\right\}$$

$$\left.+\frac{1}{\left(1-\left(\frac{2B_{NR}}{B_i}\right)^2\right)^2}\left\{1-\frac{1}{4B_NT_1}[3-4\exp(-2B_{NR}T_1)+\exp(-4B_{NR}T_1)]\right\}\right\} . \quad (56)$$

In the next section, the techniques used to evaluate these necessary coefficients are presented when the bent-pipe noise is modeled as the random telegraph signal. The results of numerical computation are then presented.

### 2.2.7 Evaluation of the Coefficients in Phase Jitter When the Bent-Pipe Noise is Modeled as the Random Telegraph Signal, Model 1

Referring to the coefficients developed in the previous section, we first consider NRZ data, for which the power spectral density (PSD) is

$$S_m(f) = T_1\left(\frac{\sin(\pi f T_1)}{\pi f T_1}\right)^2 , \quad (57)$$

where $T_1$ is the symbol time. When the arm filter is first-order Butterworth and the data is NRZ, then

$$D_1 = \int_{-\infty}^{\infty} S_m(f)\,|G(j2\pi f)|^2\,df = \int_{-\infty}^{\infty} T_1\left(\frac{\sin(\pi f T_1)}{\pi f T_1}\right)^2\left[\frac{1}{1+(\frac{f}{f_3})^2}\right] df . \quad (58)$$

This integral can be evaluated via Parseval's Theorem. Using the Fourier transform pairs

$$\mathcal{F}\left\{T_1\left(\frac{\sin(\pi f T_1)}{\pi f T_1}\right)^2\right\} = \begin{cases} 1 - \frac{|\tau|}{T_1}\,; & |\tau| \le T_1 \\ 0\,; & \text{otherwise} \end{cases} \tag{59}$$

and

$$\mathcal{F}\left\{\frac{1}{1+\left(\frac{f}{f_3}\right)^2}\right\} = \pi f_3 \exp(-2\pi f_3|\tau|)\,, \tag{60}$$

the coefficient $D_1$ can be written as

$$D_1(\text{NRZ}) = 2\int_0^{T_1}\left(1 - \frac{\tau}{T_1}\right)(\pi f_3)\exp(-2\pi f_3\tau)\,d\tau\,. \tag{61}$$

This can be integrated directly, with the result that

$$D_1(\text{NRZ}) = 1 - (2\pi f_3 T_1)^{-1}\left(1 - \exp(-2\pi f_3 T_1)\right)\,. \tag{62}$$

In terms of the two-sided noise bandwidth of the arm filter, $B_i = \pi f_3$, the coefficient $D_1$ becomes

$$D_1(\text{NRZ}) = 1 - (2B_i T_1)^{-1}\left(1 - \exp(-2B_i T_1)\right)\,, \tag{63}$$

which is the same result obtained in [6]. For biphase-L data,

$$S_m(f) = T_1\,\frac{\sin^4(\pi f T_1/2)}{(\pi f T_1/2)^2}\,. \tag{64}$$

Employing the trigonometric identity,

$$\sin^4 x = \sin^2 x - \frac{1}{4}\sin^2(2x)\,, \tag{65}$$

the PSD in (64) can be expressed as

$$S_m(f) = 2\left(\frac{T_1}{2}\right)\frac{\sin^2(\pi f T_1/2)}{(\pi f T_1/2)^2} - T_1\frac{\sin^2(\pi f T_1)}{(\pi f T_1)^2} . \qquad (66)$$

Spectrally, this looks like the difference of two NRZ spectra of different data rates. Taking (66) and the result for NRZ data obtained above, we have that

$$D_1(\text{biphase-L}) = 2D_1(\text{NRZ})\Big|_{T_1 \to T_1/2} - D_1(\text{NRZ})\Big|_{T_1 \to T_1} . \qquad (67)$$

Substituting (62) into (66) and simplifying yields

$$D_1(\text{biphase-L}) = 1 - (2B_iT_1)^{-1}[3 - 4\exp(-B_iT_1) + \exp(-2B_iT_1)] , \qquad (68)$$

which also agrees with that in [6].

The remaining integral for the random telegraph signal is $D_{12}$, as given by (55) in the previous section. This integral can also be evaluated via partial fraction expansion of the last two bracketed terms in (55), with the result that $D_{12}$ can be written as

$$D_{12} = 2\pi^3 T_1 B_{N1} f_3^4 \left\{ \frac{1}{(2B_{N1})^2 - (\pi f_3)^2} \int_{-\infty}^{\infty} \frac{\sin^4(xT_1/2)}{(xT_1/2)^2} \frac{dx}{[(\pi f_3)^2 + x^2]^2} \right.$$

$$- \left[\frac{1}{(2B_{N1})^2 - (\pi f_3)^2}\right]^2 \int_{-\infty}^{\infty} \frac{\sin^4(xT_1/2)}{(xT_1/2)^2} \frac{dx}{[(\pi f_3)^2 + x^2]}$$

$$\left. + \frac{1}{[(2B_{N1})^2 - (\pi f_3)^2]^2} \int_{-\infty}^{\infty} \frac{\sin^4(xT_1/2)}{(xT_1/2)^2} \frac{dx}{[(2B_{N1})^2 + x^2]} \right\} . \qquad (69)$$

From (58) and (62),

$$\int_{-\infty}^{\infty} \frac{\sin^4(xT_1/2)}{(xT_1/2)^2} \frac{dx}{[(\pi f_3)^2 + x^2]} = \frac{\pi}{T_1 B_i^2}\left\{1 - \frac{1}{2B_iT_1}[3 - 4\exp(-B_iT_1) + \exp(-2B_iT_1)]\right\}$$

(70)

where $B_i = \pi f_3$ .

$$\int_{-\infty}^{\infty} \frac{\sin^4 (x T_1/2)}{(x T_1/2)^2} \frac{dx}{[(2B_{N1})^2 + x^2]}$$

$$= \frac{\pi}{4T_1 B_{N1}^2} \left\{1 - \frac{1}{2B_{N1}T_1}[3 - 4\ \exp(-2B_{N1}T_1) + \exp(-4B_{N1}T_1)]\right\} \tag{71}$$

and

$$\int_{-\infty}^{\infty} \frac{\sin^4 (x T_1/2)}{(x T_1/2)^2} \frac{dx}{[(\pi f_3)^2 + x^2]^2}$$

$$= \frac{1}{\pi^3 T_1 f_3^4} \left\{1 - \frac{1}{4\pi f_3 T_1}[9 - 4(3 + \pi f_3 T_1) \exp(-\pi f_3 T_1) + (3 + 2\pi f_3 T_1) \exp(-2\pi f_3 T_1]\right\} . \tag{72}$$

Upon substitution of (70) and (72) into (69), we obtain

$$\begin{aligned} D_{12} = \frac{2}{\pi} (T_1 B_i^4 B_{N1}) \Bigg\{ & \left[\frac{1}{(2B_{N1})^2 - B_i^2}\right] \frac{\pi}{T_1 B_i^4} \\ & \times \left\{1 - \frac{1}{4B_i T_1}[9 - 4(3 + B_i T_1) \exp(-B_i T_1) + (3 + 2B_i T_1) \exp(-2B_i T_1)]\right\} \\ & - \left[\frac{1}{(2B_{N1})^2 - B_i^2}\right]^2 \left[\frac{\pi}{T_1 B_i^2}\right] \left\{1 - \frac{1}{B_i T_1}[3 - 4 \exp(-B_i T_1) + \exp(-2B_i T_1)]\right\} \\ & + \left[\frac{1}{(2B_{N1})^2 - B_i^2}\right]^2 \frac{\pi}{4B_{N1}^2 T_1} \\ & \times \left\{1 - \frac{1}{4B_{N1}T_1}[3 - 4 \exp(-2B_{N1}T_1) + \exp(-4B_{N1}T_1)]\right\}\Bigg\} . \end{aligned} \tag{73}$$

The results of this section, when substituted into the expression for the RMS phase error (45), can now be used to predict tracking performance of the Costas loop associated with the bent-pipe channel. The results of numerical computations are presented in Section 2.2.9.

### 2.2.8 RMS Phase Jitter When the Bent-Pipe Noise is Represented by Model 2

As pointed out previously, the structure of the general result for the RMS phase jitter in (45) is independent of the modulation and noise formats in $x(t)$. They affect only the evaluation of $D_1$, $D_2$ and $D_{12}$. In the bent-pipe model, the biphase-L assumption for Channel 1 remains unchanged. Therefore, $D_1 = D_1(\text{biphase-L})$ remains as given by (50).

The coefficients $D_2$ and $D_{12}$ are different, however. First consider the exact evaluation of $D_2$ for Model 2, the hard-limited, filtered Gaussian noise model.

The power spectral density for the hard-limited, filtered noise model is obtained by taking the Fourier transform of $R_{m_2}(\tau)$ in (60) and (63), namely,

$$\begin{aligned} S_{m_2}(f) &= \mathcal{F}\{R_{m_2}(\tau)\} = \int_{-\infty}^{\infty} R_{m_2}(\tau)\exp[-j2\pi f\tau]\,d\tau \\ &= 2\int_0^{\infty} R_{m_2}(\tau)\cos 2\pi f\tau\,d\tau \\ &= \frac{4}{\pi}\int_0^{\infty} \sin^{-1}[\exp(-4B_{Ny}\tau)]\cos 2\pi f\tau\,d\tau\,. \end{aligned} \tag{74}$$

Although (74) resists a closed-form solution, we shall see that this is not necessary to obtain a closed-form solution for the corresponding coefficient $D_2$. In fact, substituting (74) and the squared magnitude of (48) into the definition of $D_2$ in (29) gives

$$D_2 = \frac{8}{\pi}\int_0^{\infty} \sin^{-1}[\exp(-\alpha\tau)]\left\{\int_0^{\infty}\frac{\cos 2\pi f\tau}{1+\left(\frac{f}{f_3}\right)^2}\,df\right\}d\tau\,. \tag{75}$$

From Equation 3.723-2 (p. 406) of [10], we have that

$$\int_0^\infty \frac{\cos(\gamma x)}{\beta^2 + x^2} = \frac{\pi}{2\beta} e^{-\gamma\beta}; \qquad (\gamma > 0,\ \beta > 0)\ . \tag{76}$$

Thus,

$$D_2 = \frac{4}{\pi} B_i \int_0^\infty \sin^{-1}\left[\exp(-\alpha\tau)\right] \exp(-2B_i\tau)\, d\tau\ . \tag{77}$$

Letting

$$x = \exp(-\alpha\tau); \quad dx = -\alpha x\, d\tau; \tag{78}$$

and

$$\exp(-2B_i\tau) = \left[\exp(-\alpha\tau)\right]^{B_i/(2B_{Ny})} = x^{B_i/(2B_{Ny})}, \tag{79}$$

then, using (10)

$$D_2 = \frac{1}{\pi} \frac{B_i}{B_{Ny}} \int_0^1 x^{\left((B_L/2B_{Ny})-1\right)} (\sin^{-1} x)\, dx\ . \tag{80}$$

The integral in (80) can be integrated by parts. Letting $\gamma = (B_i/B_{Ny}) - 1$, then

$$\begin{aligned}\int_0^1 \underbrace{x^\gamma}_{u} \underbrace{\sin^{-1} x\, dx}_{dv} &= x^\gamma \left[x \sin^{-1} x + \sqrt{1-x^2}\right]\Big|_0^1 \\ &\quad - \int_0^1 \gamma x^{\gamma-1} (x \sin^{-1} x)\, dx - \int_0^1 \gamma x^{\gamma-1}\sqrt{1-x^2}\, dx \\ &= \frac{\pi}{2} - \gamma\int_0^1 x^\gamma \sin^{-1} x\, dx - \gamma\int_0^1 x^{\gamma-1}\sqrt{1-x^2}\, dx\ . \end{aligned} \tag{81}$$

Thus,

$$\int_0^1 x^\gamma \sin^{-1} x\, dx = \left(\frac{1}{1+\gamma}\right)\left[\frac{\pi}{2} - \gamma\int_0^1 x^{\gamma-1}\sqrt{1-x^2}\, dx\right]\ . \tag{82}$$

But, from equation 3.251-1 (p. 294) of [10],

$$\int_0^1 x^{\mu-1}(1-x^{\lambda})^{\nu-1}\,dx = \frac{1}{\lambda} B\left(\frac{\mu}{\lambda},\nu\right); \qquad (\mu,\nu,\lambda > 0) \tag{83}$$

where

$$B(x,y) = \frac{\Gamma(x)\,\Gamma(y)}{\Gamma(x+y)} \tag{84}$$

is the beta function. Thus, letting $\mu = \gamma$, $\lambda = 2$, and $\nu = 3/2$, we get the desired result

$$\int_0^1 x^{\gamma} \sin^{-1} x\,dx = \left(\frac{1}{1+\gamma}\right)\left[\frac{\pi}{2} - \frac{\gamma}{2}\,\frac{\Gamma\left(\frac{\gamma}{2}\right)\Gamma\left(\frac{3}{2}\right)}{\Gamma\left(\frac{\gamma+3}{2}\right)}\right]. \tag{85}$$

Finally, letting $\gamma = (B_i/B_{Ny}) - 1$, and using $\Gamma(3/2) = \sqrt{\pi}/2$, we have from (85) and (80) that

$$D_2 = 1 - \left(\frac{1}{2\sqrt{\pi}}\right)\left(\frac{B_i}{2B_{Ny}} - 1\right)\frac{\Gamma\left(\frac{B_i}{4B_{Ny}} - \frac{1}{2}\right)}{\Gamma\left(\frac{B_i}{4B_{Ny}} + 1\right)}\,. \tag{86}$$

The remaining term to be evaluated for Model 2 is the cross-correlation coefficient $D_{12}$, defined by (41). This is considerably more difficult to compute when $R_{m_2}(\tau)$ is given by (6) and (9). Since this cross-correlation coefficient does not appear to be attainable in closed form, we alternatively employ the least-squares approximation of the autocorrelation function of Model 2 by that of the random telegraph signal. This is discussed in Section 2.2.2. The net effect of this approximation is to replace $B_{N1}$ in (73) by

$$B_{N1} \rightarrow \frac{2.26}{2} B_{Ny}\,. \tag{87}$$

### 2.2.9 RMS Phase Error Computations When the Bent-Pipe Signal is Noise Only

The analytical results of the previous sections have been computed for typical parameters when the bent-pipe signal is noise only. When the power ratio is

$$\frac{P_2}{P_1} = 4 , \tag{88}$$

then the denominator in the RMS phase error expression goes to zero when

$$4D_2 - D_1 = 0 . \tag{89}$$

The conditions under which this occurs for Models 1 and 2 are shown in Figure 4. For Model 1, $D_1$ is given by (50) and $D_2$ by (53). The relationship between $B_i/(2B_{N1})$ and $B_iT_1$ which satisfies (89) is shown in Figure 4. The symbol time $T_1$ is that of the 192 kbps operations data link. Therefore,

$$T_1 = [192 \text{ kbps}]^{-1} = 5.2 \text{ sec} .$$

The bandwidth $B_i$ is the two-sided noise bandwidth of the arm filters in the Costas loop. The bandwidth $B_{N1}$ is the one-sided noise bandwidth of the random telegraph model of the bent-pipe noise after the hard-limiter.

The arm bandwidth $B_i$ of the Costas loop has an optimum value [8] depending on the anticipated data rate and choice of signal format in Channel 2, the high power channel. For example, if we assume the range of data rates in the bent-pipe channel (Channel 2) is (16 kbps, 2 Mbps), and if we assume the biphase-L waveform, the optimum value of $B_i$ is approximately twice the data rate. Therefore, $B_iT_1$ roughly ranges over the interval (0.1,20).

Examination of Figure 4 shows that, for each value of $B_iT_1$, there is a choice of $B_i/(2B_{N1})$, and therefore $B_{N1}$, which will cause the powers in the arms of the Costas loop to be equal, with the result that the loop will not operate. For Model 2, $D_1$ is again given by (50), but $D_2$ is now given by (86).

The argument of the gamma function in the numerator is between (-1,0). The reflection formula [11] can be used to obtain a gamma function with positive argument which is then amenable to polynomial approximations. The results are labeled Model 2 in Figure 4, where the noise bandwidth is $B_{Ny}$. This bandwidth is for the signal y(t) in Figure 2 after the LPF and before the hard-limiter.

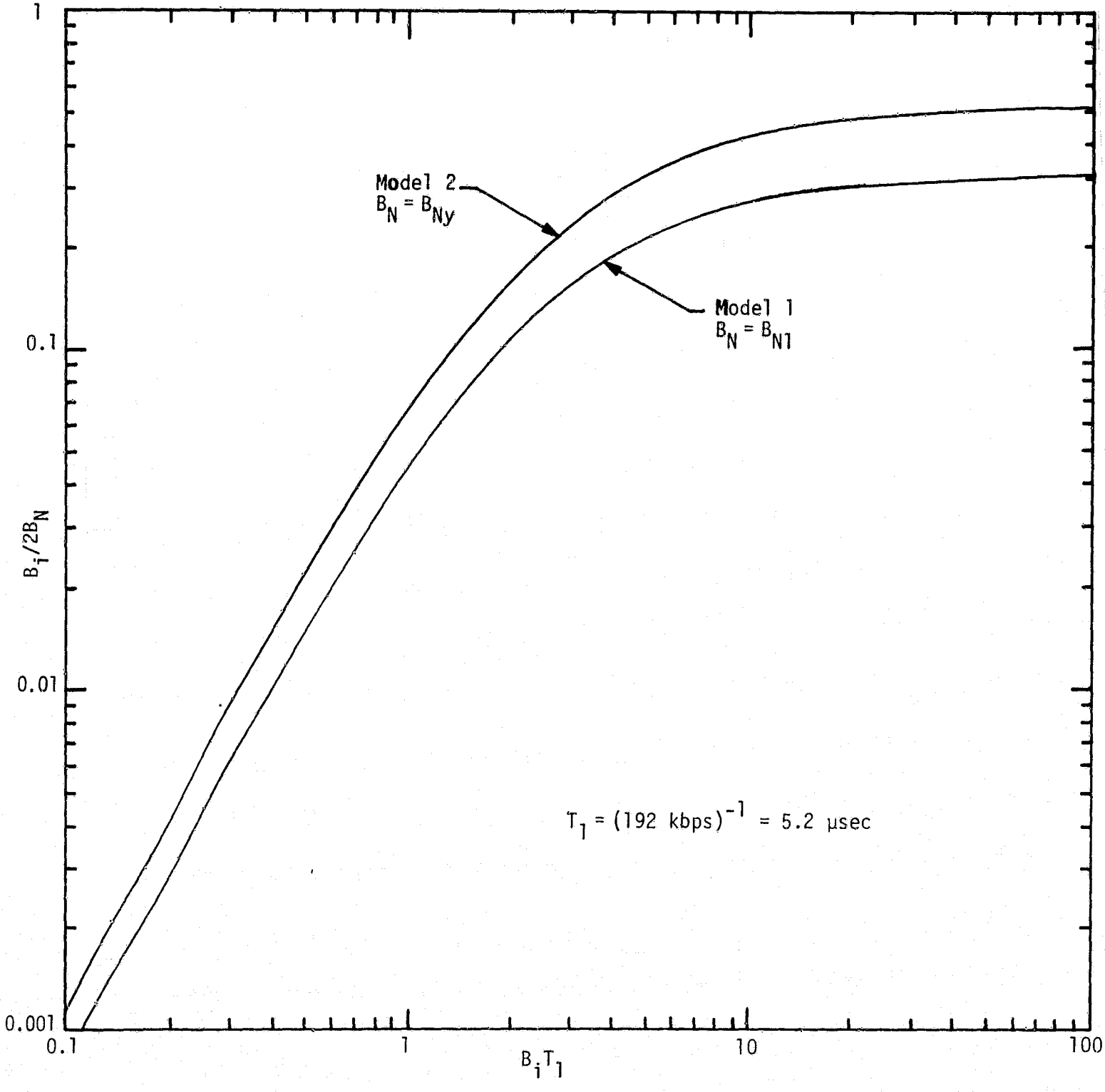


Figure 4. Plot of $B_i/2B_N$ Versus $B_iT_1$ When the Phase Tracking Error Approaches Infinity and the Bent-Pipe Signal is Noise Only

Inspection of Figure 4 reveals that the results for both models are similar. Since the two models are very dissimilar, however, it can be concluded that the phenomena described in Figure 4 are independent of the choice of model for the bent-pipe noise.

For each value of $B_iT_1$, when the bent-pipe signal consists of noise only, there is a noise bandwidth of the bent-pipe noise which is such that the Costas loop has the same power in both arms. The result is that the power in the error signal goes to zero, and the loop will not track.

For the random telegraph signal, the cross-correlation coefficient $D_{12}$ defined by (41) has been evaluated in closed form. The result is given by (73). Along with exact expressions for $D_1$ and $D_2$ given in (68) and (53), respectively, an exact closed-form expression for the RMS phase error is obtained for Model 1.

The results are shown in Figure 5, where the RMS phase error is plotted against $B_iT_1$ for various values of $B_{N1}$ that are considered typical for the bent-pipe mode. The RMS phase error is shown for $B_L$, the Costas loop noise bandwidth, equal to 300, 500, and 700 Hz, in Figures 5a, 5b, and 5c, respectively. It is observed that, for each value of $B_{N1}$, there is a value of $B_iT_1$ where $\sigma_\phi \to \infty$. Also note that, as the value of $B_{N1}$ is increased, the value of $B_iT_1$ where $\sigma_\phi \to \infty$ also increases. Finally, observe that, on either side of this critical value of $B_iT_1$, satisfactory tracking is attained.

For the Gaussian noise model through the hard-limiter (Model 2), the cross-correlation coefficient $D_{12}$ has been approximated as described at the end of Section 2.2.8. When the exact expressions for $D_1$ and $D_2$ and the approximate result for $D_{12}$ are substituted into (45) for $\sigma_\phi$, the result is as shown in Figure 6. The RMS phase error performance of the Costas loop for Model 2 is similar to that for Model 1. The variation in performance with respect to the loop bandwidth $B_L$ and the noise bandwidth is similar in both cases. The noise bandwidth $B_{Ny}$ in Figure 6 is for the noise model after being filtered by the first-order Butterworth filter and before the hard-limiter in the bent-pipe signal processor.

In Section 2.4, these results are used to explain the tracking anomalies in the laboratory setup at NASA-JSC. In addition, various alterations are discussed and our recommendations are given.

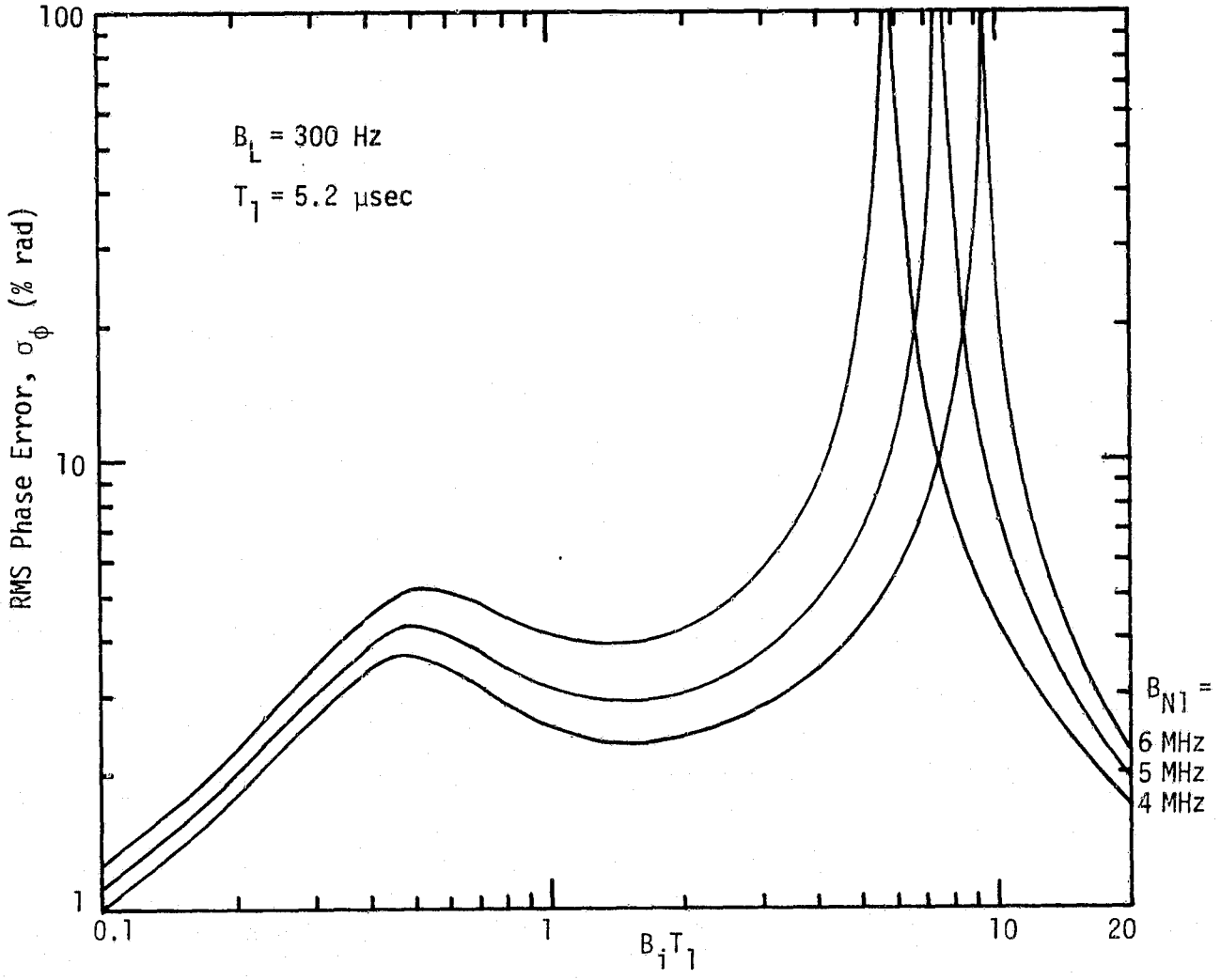


Figure 5a. RMS Phase Error of the Costas Loop When the Bent-Pipe Signal Consists of Model 1 Noise

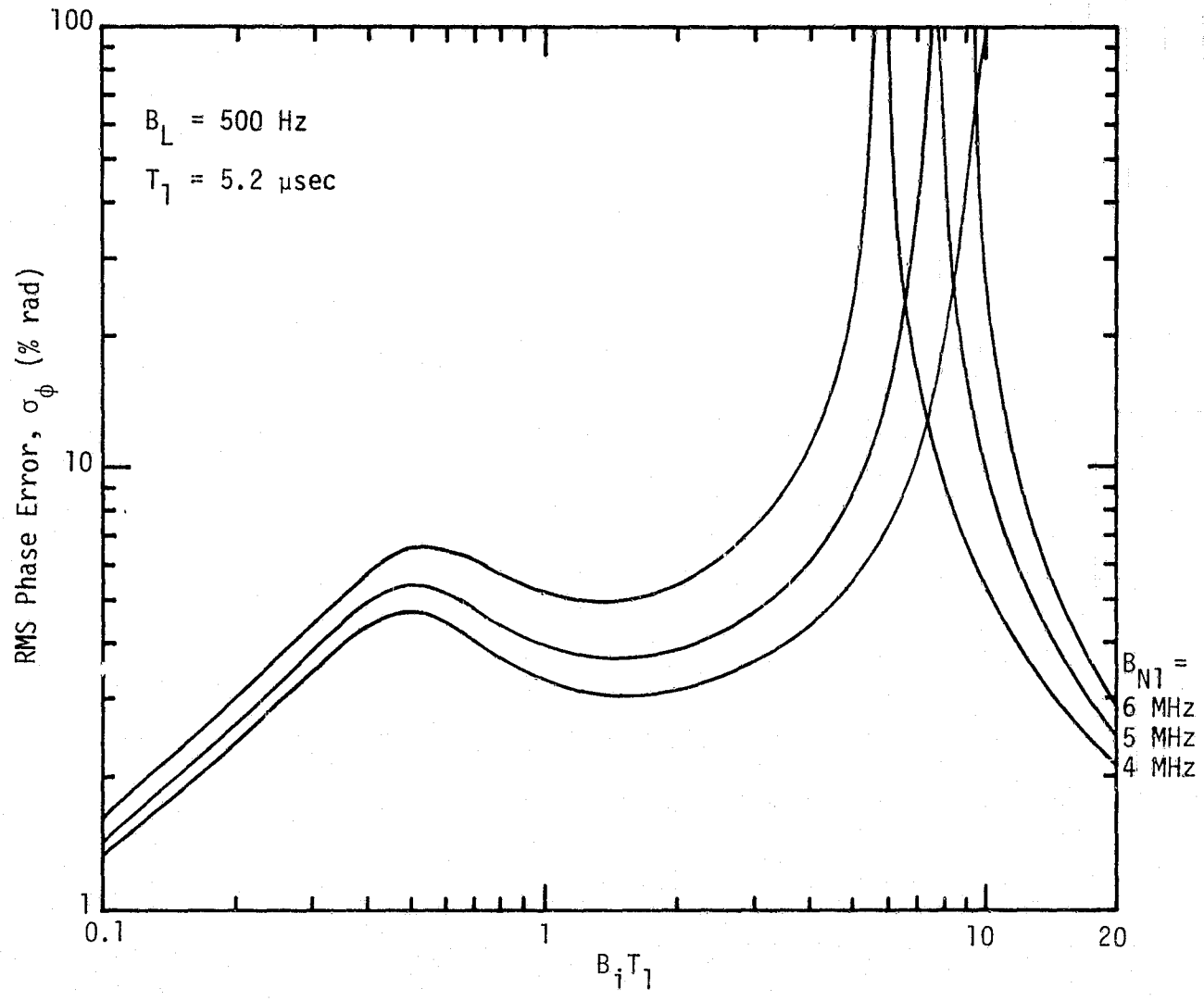


Figure 5b. RMS Phase Error of the Costas Loop When the Bent-Pipe Signal Consists of Model 1 Noise

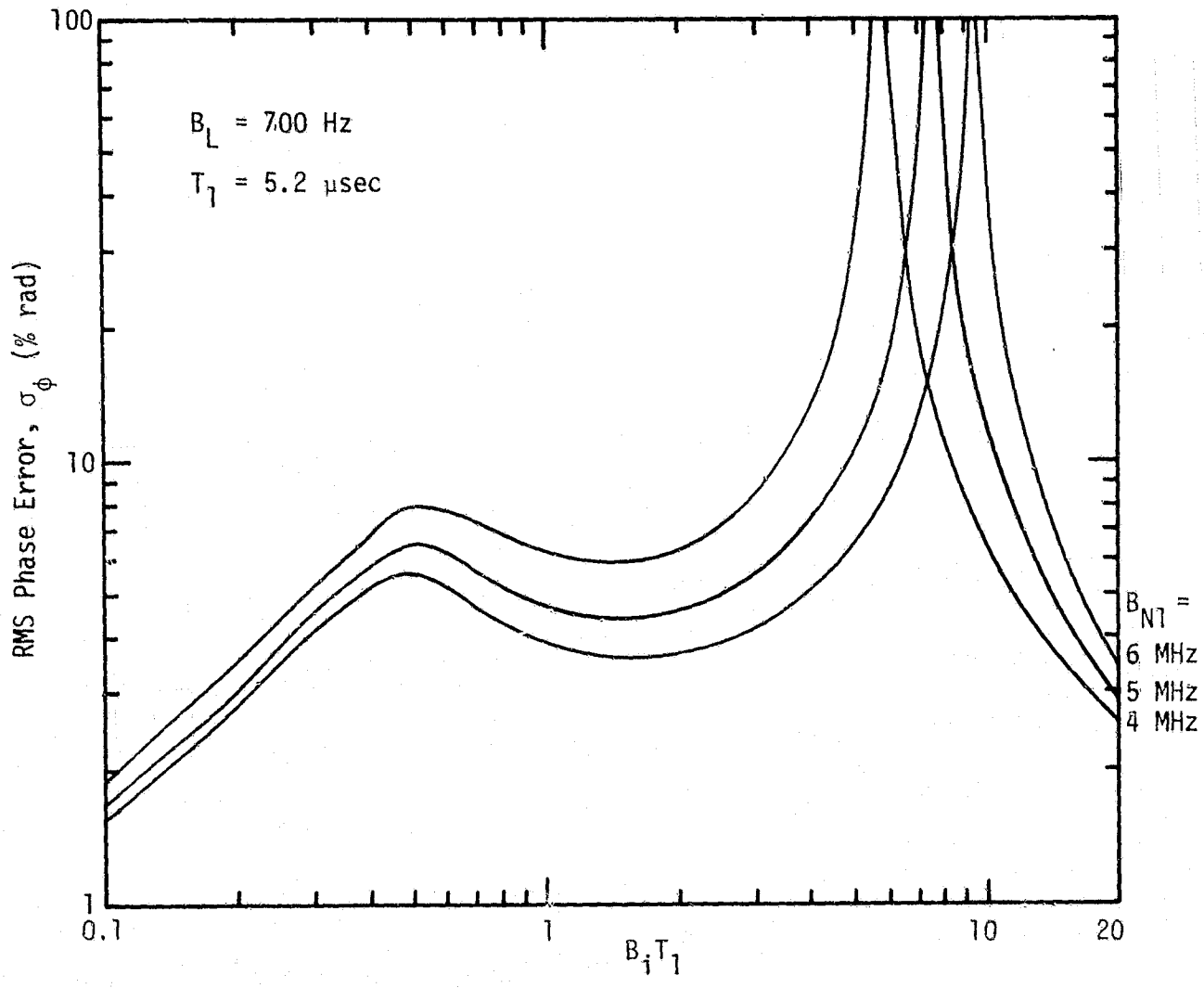


Figure 5c. RMS Phase Error of the Costas Loop When the Bent-Pipe Signal Consists of Model 1 Noise

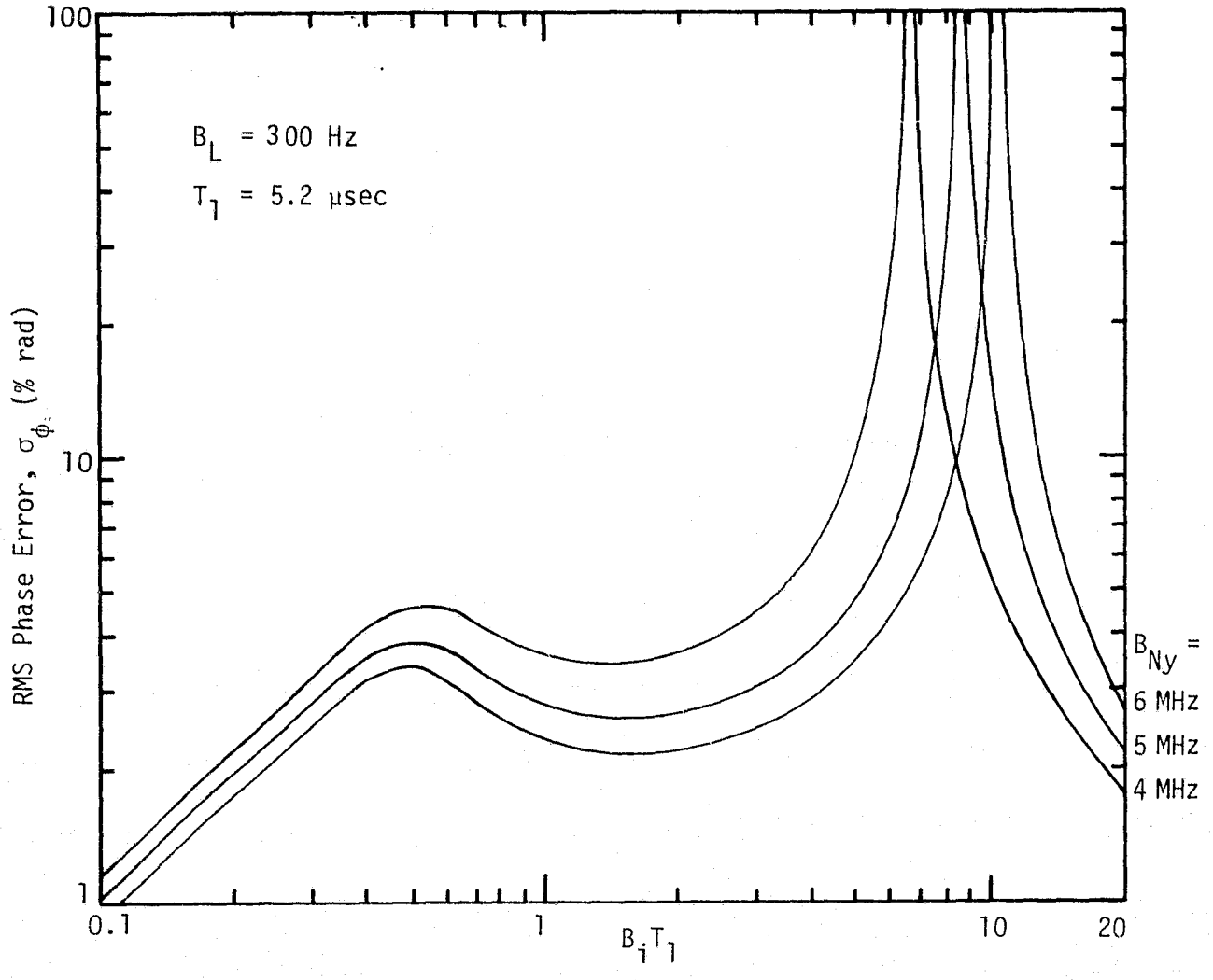


Figure 6a. RMS Phase Error of the Costas Loop When the Bent-Pipe Signal Consists of Model 2 Noise

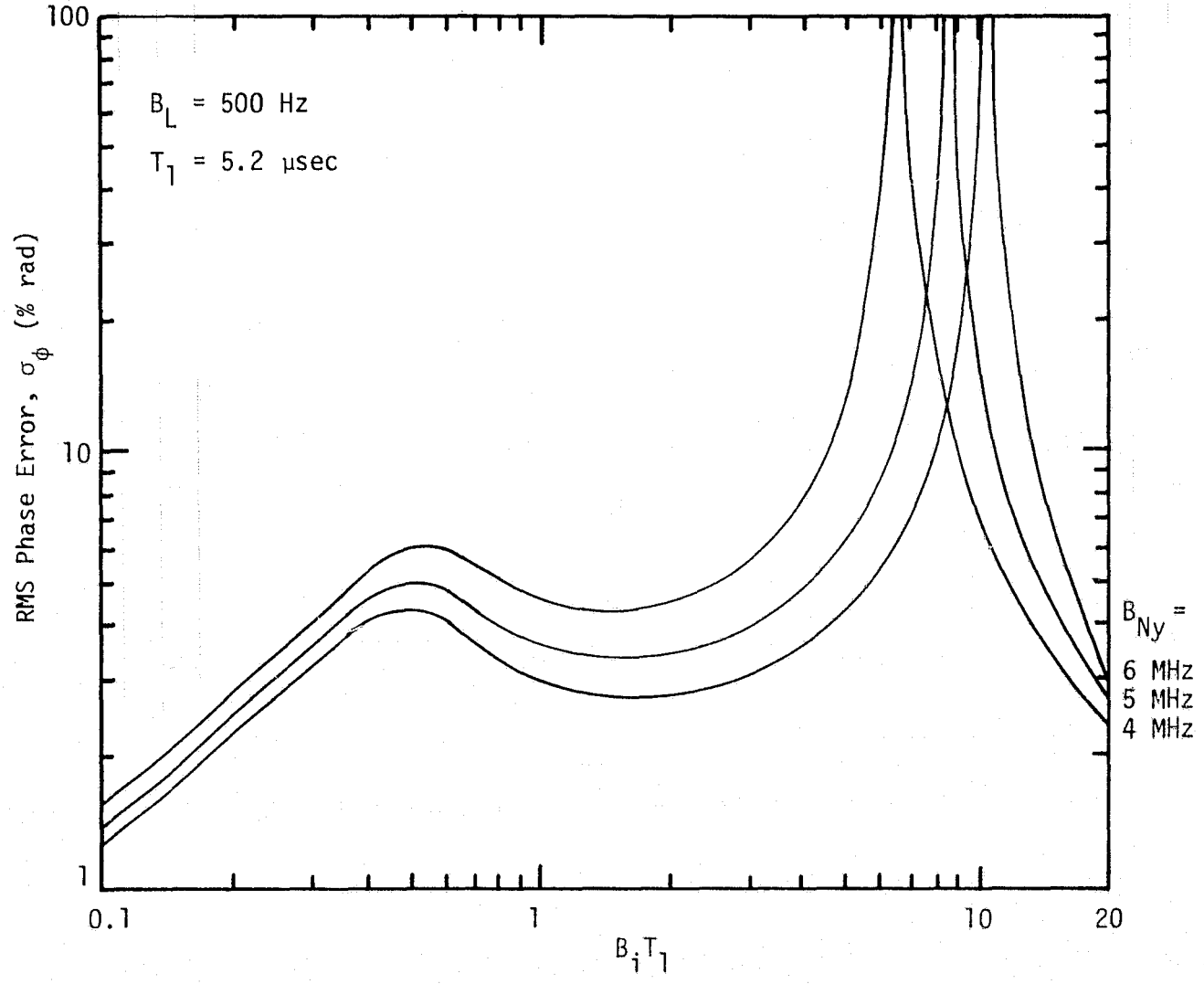


Figure 6b. RMS Phase Error of the Costas Loop When the Bent-Pipe Signal Consists of Model 2 Noise

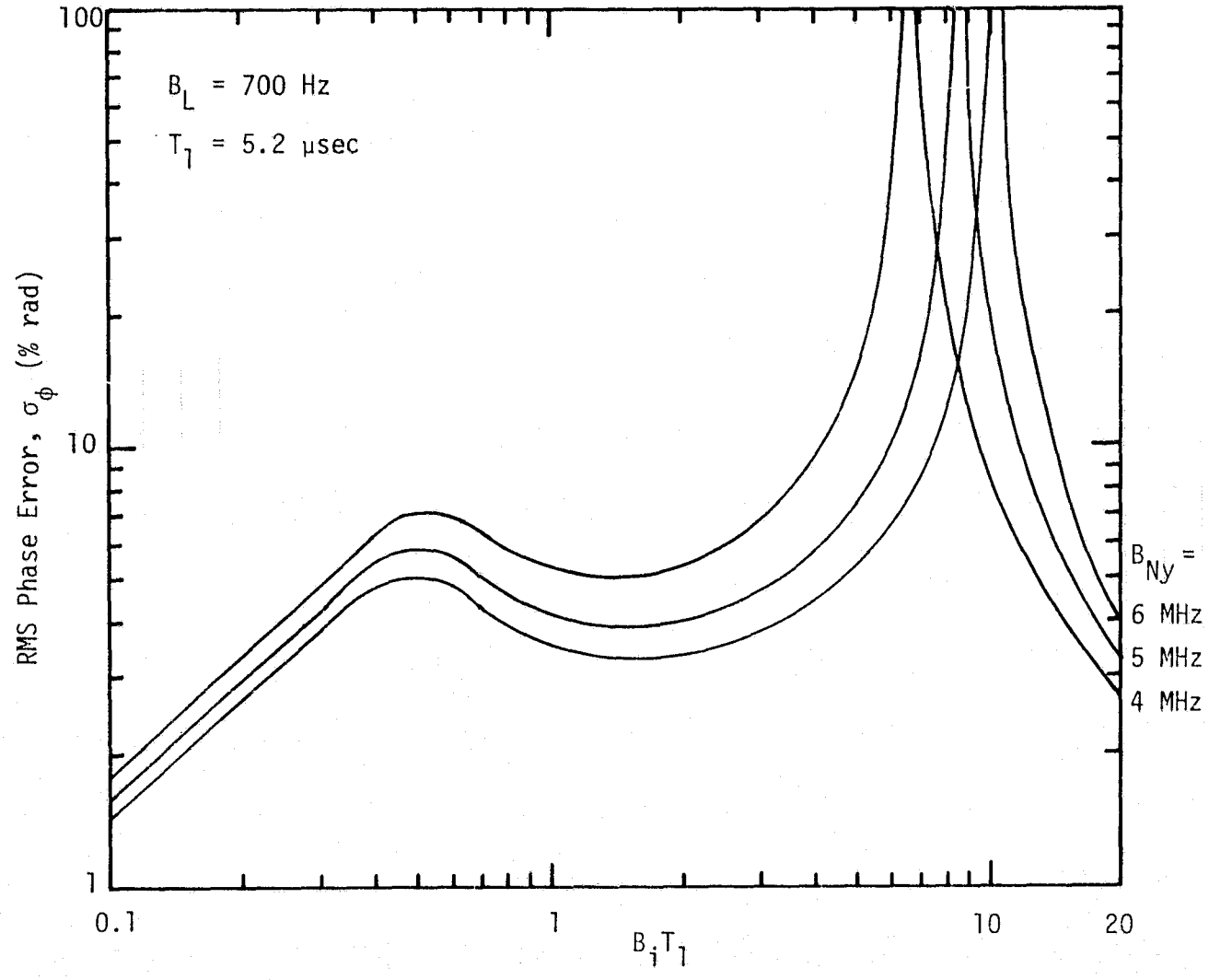


Figure 6c. RMS Phase Error of the Costas Loop When the Bent-Pipe Signal Consists of Model 2 Noise

## 2.3 Biphase Costas Loop Tracking of a High SNR Bent-Pipe Signal

When the bent-pipe channel to the PI operates at high values of signal-to-noise ratio, it can be assumed that the received waveform consists of the desired signal only. When this is the case, the combinations of signal formats, data rates, and signal-to-noise ratios which give satisfactory performance have been addressed by Simon and Alem [6].

The design of the bent-pipe signal processor needs to emphasize the case when the bent-pipe channel consists of noise only. When the design has been chosen so that the bent-pipe channel provides a satisfactory reference even in the absence of a data signal, then the range of data rates and data formats that are acceptable for the bent-pipe channel can be determined. In this report, we emphasize the design parameters so that the channel operates satisfactorily in the absence of a bent-pipe signal.

## 2.4 Discussion of Possible Alterations and Our Recommendations

The possible alterations which will avoid the situation where the Costas loop will not track are best described by first relating our analytical results to the results of the NASA-JSC laboratory tests described in [12].

Example - NASA-JSC Laboratory Test of Bent-Pipe Noise

The NASA-JSC test is very similar to the system description given in Figure 1, with

$m_2(t)$ = 51.2 kbps bent-pipe NRZ data modulating a 1.024 MHz squarewave subcarrier

$n(t)$ = additive white Gaussian noise

LPF = lowpass filter (which shapes the PSD of the noise) with a 3 dB bandwidth of 4 MHz (see Figures 1 and 2)

$m_1(t)$ = 192 kbps biphase-L data (operations data link).

The signal-to-noise ratio in the bent-pipe signal at the input to the hard-limiter in Figure 2 was varied in the laboratory test setup over a range of values of signal-to-noise ratios [12]. We will look at both the high and low signal-to-noise ratio cases.

As indicated above, the lowpass filter which shapes the spectrum of the bent-pipe noise is first-order Butterworth with 3 dB bandwidth

$$f_3 = 4 \text{ MHz} . \tag{90}$$

Therefore,

$$B_{Ny} = \frac{\pi}{2} f_3 = 6.3 \text{ MHz} \tag{91}$$

$$= \text{one-sided noise bandwidth} .$$

Also, the Costas loop sees the 51.2 kbps NRZ data on the 1.024 squarewave subcarrier as NRZ data with symbol rate approximately given by

$$1.024 + 0.051 = 1.075 \text{ Mbps} . \tag{92}$$

At large values of signal-to-noise ratio, the bent-pipe signal can then be effectively modeled using either Model 1 or Model 2.

When a Costas loop develops a coherent reference from NRZ data, there is an optimal arm bandwidth [13-14] which is dependent on signal-to-noise ratio and filter shape. The optimal bandwidth is shown in Figure 7 using the results developed in [13]. For the bent-pipe NRZ signal at 1.024 Mbps, and an RC arm filter, the optimal choice of arm filter two-sided noise bandwidth is within the interval

$$1.5 \text{ MHz} \leq B_{i_{opt}} \leq 2.5 \text{ MHz} . \tag{93}$$

At higher values of signal-to-noise ratio, the optimal value of $B_i$ is not very sensitive, which can be seen from inspection of Figure 7. With $B_i$ as in (93), then,

$$7.8 \leq B_i T_1 \leq 13 . \tag{94}$$

Consider the following conditions:

(a) $B_i T_1$ as in (94) (namely, [7.8,13])

(b) $B_{Ny}$ as in (91) (namely, 6.3 MHz)

(c) The SNR drops so that the bent-pipe noise dominates Channel 2.

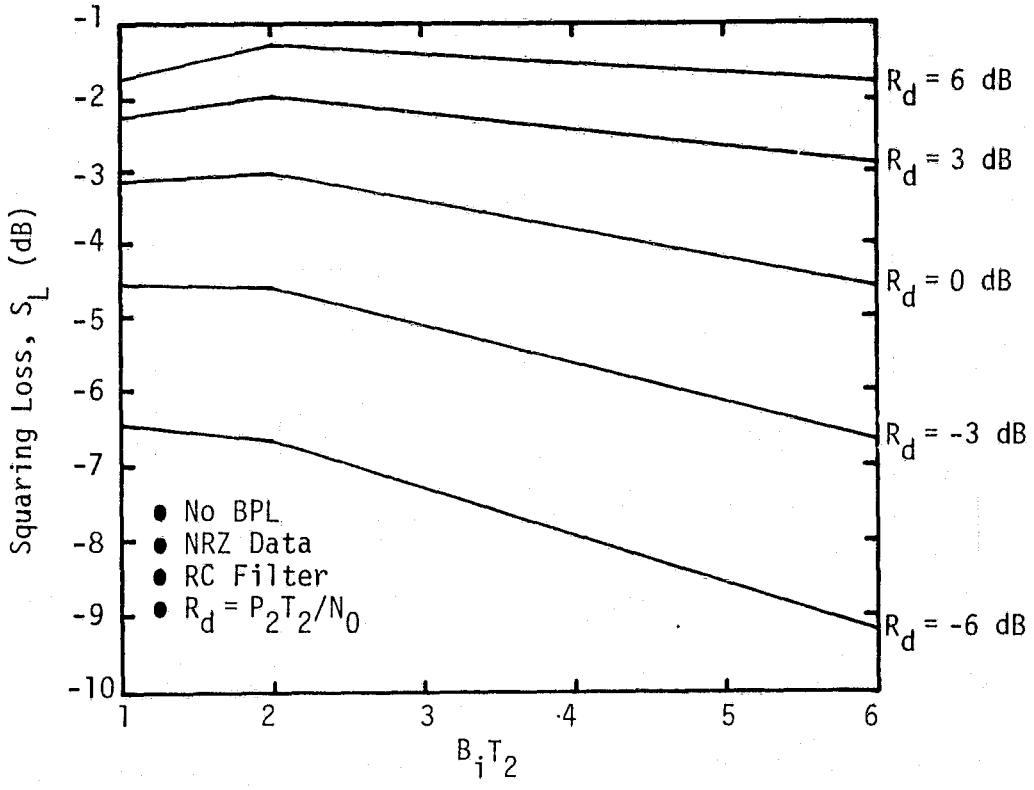


Figure 7. Squaring Loss in a Costas Loop Versus $B_iT_2$ for Various Values of Signal-to-Noise Ratio

Then, inspection of Figures 5 and 6 reveals that, within the entire interval of $B_iT_1$ in (94) and $B_{Ny} \approx 6$ MHz, the Costas loop performance is poor to not tracking at all. This particular set of parameters used for the NASA-JSC test is therefore not satisfactory. The analysis presented herein therefore coincides with the tracking difficulties encountered in the NASA-JSC test.

Also, at high values of signal-to-noise ratio in the bent-pipe channel, the squaring loss from Figure 7 is less than 2 dB, and this situation prevails over a large range of high values of signal-to-noise ratio. This also agrees with NASA-JSC test results. Equivalently stated, with a power ratio of 4:1, a data rate ratio of 5:1, the RMS error is approximately 2% of a radian [1] when the signal-to-noise ratio is 10 dB in the downlink channel.

Returning to the noise-only case of this bent-pipe example, we also note from Figures 5 and 6 that $B_iT_1 = 20$ is a satisfactory operating point for both noise models when

$$B_N < 6 \text{ MHz} . \tag{95}$$

The value of $B_iT_1 = 20$ corresponds to a two-sided noise bandwidth of

$$B_i = 3.8 \text{ MHz} \tag{96}$$

and a 3 dB cutoff frequency for an RC arm filter of

$$f_3 = 1.2 \text{ MHz} . \tag{97}$$

Also, for the range of $B_N$ shown in Figures 5 and 6, a smaller value of $B_iT_1$ would also produce satisfactory values of RMS phase error.

With these results in mind, we now consider various fixes so as to avoid this problem and then make our recommendation.

Fix 1. This fix consists in setting the two-sided noise bandwidth of the arm filters $B_i$ to be such that

$$B_iT_1 = 20 . \tag{98}$$

This corresponds to

$$B_i = 3.8 \text{ MHz}$$

and a 3 dB cutoff frequency of the arm filters of 1.2 MHz. At high values of signal-to-noise ratio in the downlink channel, there is negligible increase in squaring loss incurred by this widening of the arm filters of the 8.5 MHz Costas loop [1, 8, 13]. This assumes that there is adequate design margin in the Orbiter-TDRSS-ground link. The present filter in the PI link has a noise bandwidth of $B_N = 5.5$ MHz. From Figures 5 and 6, it is seen that, at $B_i T_1 = 20$, any noise bandwidth in the bent-pipe channel which is less than 6 MHz will not cause any tracking difficulties in the 8.5 MHz Costas loop. The RMS phase error will be less than 3% of a radian (less than 1.75 deg).

This fix has the advantage that no changes are required on-board the Shuttle and that no new hardware needs to be added on the ground. Only arm filter changes need to be made.

Fix 2. This fix consists of narrowing the noise bandwidth of the bent-pipe noise by placing a lowpass filter in front of the limiter in the bent-pipe signal processor on the Orbiter, while keeping the arm bandwidth $B_i$ fixed at its present value.

Examination of Figures 5 and 6 shows that, as $B_N$ is decreased, the value of $B_i T_1$ at which $\sigma_\phi \to \infty$ also decreases. Therefore, by narrowing $B_N$ sufficiently, say to 2 MHz, then the present value of $B_i$ could be used.

This fix has two disadvantages:

(a) It will significantly constrain the allowable data rate in the bent-pipe channel.

(b) It requires additional hardware on the Orbiter (namely, the added filter).

Fix 3. It has been noted in Figures 5 and 6 that, for a given noise bandwidth $B_N$, satisfactory tracking performance can be attained on either side of the critical value of $B_i T_1$. The present value of $B_N$ is approximately 5.5 MHz. This fix is to reduce $B_i$ so that $B_i T_1$ is well below the critical value of approximately within the interval 8 to 10. From Figures 5 and 6, a value in the interval 1 to 2 would be satisfactory. This fix has the significant disadvantage that, if the actual bent-pipe noise bandwidth is less than the maximum value it can be because of $B_N$ filtering, this lower value may correspond to the new critical interval for $B_i T_1$. Equivalently stated, even though $B_N = 5.5$ MHz, there is no

guarantee that all bent-pipe noises will be at $B_N = 5.5$ MHz. There is nothing to prevent a smaller value, if that is the statistic of the noise which is present.

Recommendation: Of the candidates, we recommend the first fix. The payload interrogator must have a maximum allowable bandwidth which is now set at $B_N = 5.5$ MHz. If we narrow $B_N$, a fix is obtained, but at the expense of a smaller maximum data rate allowable through the bent-pipe channel. The arm filters on the ground already exist, however. It is therefore an easy and inexpensive fix to increase the arm filter bandwidth to a noise bandwidth (two-sided) of 3.8 MHz, or a 3 dB cutoff value of 1.22 MHz. Since the increase in squaring loss incurred is negligible when increasing $B_i$, nothing is gained in Fixes 2 and 3 that is not also obtained by Fix 1.

Last Fix. This entire discussion was based on the assumption that the arm filters are passive. In the event that it is decided to implement the arm filters by active filters [14], then the noise bandwidth of the arm filters is variable. For each of the arm filter bandwidths, there is a bent-pipe noise bandwidth which will cause the Costas loop to not track. To overcome this difficulty, a variable lowpass filter would be necessary on-board in front of the hard-limiter in the bent-pipe signal processor. Since there is sufficient margin in signal-to-noise ratio that an active arm filter is not justified, we strongly recommend that active arm filters in the Costas loop not be considered. It clearly would substantially complicate the bent-pipe signal processing problem.

# 3.0 EVALUATION OF KU-BAND TDRSS USER CONSTRAINTS

To transmit data to the TDRS, the Shuttle Ku-band return link uses one of two selectable modes, a phase modulation mode (Mode 1) and a frequency modulation mode (Mode 2). In either mode, the information bearing signal is obtained by multiplexing two low data rate channels (Channel 1 and Channel 2) and one high data rate channel (Channel 3).

In Mode 1, Channels 1, 2 and 3 are double quadriphase (QDSB) modulated, resulting in a nominal power distribution of 4%, 16%, and 80%, respectively.

The following subsections present a comparison of the TDRSS user constraints and the Hughes Aircraft (HAC) specifications as they apply to Mode 1.

Since most of the degradations in Mode 1 occur in the high data rate channel (Channel 3), the analysis is done considering this channel as independent.

The additional effect of the QPSK modulator for the subcarrier (Channels 1 and 2) is briefly treated at the end of this section.

A simplified model of the system under consideration and the parameters causing degradations are shown in Figure 8.

For the return link services, 31 hardware parameters are constrained by NASA Goddard Space Flight Center. Of these, the four constraints that relate to PN codes, coherent phase noise, I/Q data skew, and short-term EIRP stability do not apply to the Shuttle Ku-band return link.

Also, the analysis does not deal with the nine parameters listed below:

- Parameters associated with the subcarrier oscillator (2).
- Parameters associated with EIRP (4).
- Axial ratio for autotrack (1).
- Minimum 3 dB bandwidth prior to power amplification (1).
- Gain slope (because gain flatness yields worst-case).
- I/Q phase (applicable to QPSK only).

The remaining 14 parameters and their combined effect on an independent BPSK channel are discussed in the next subsection.

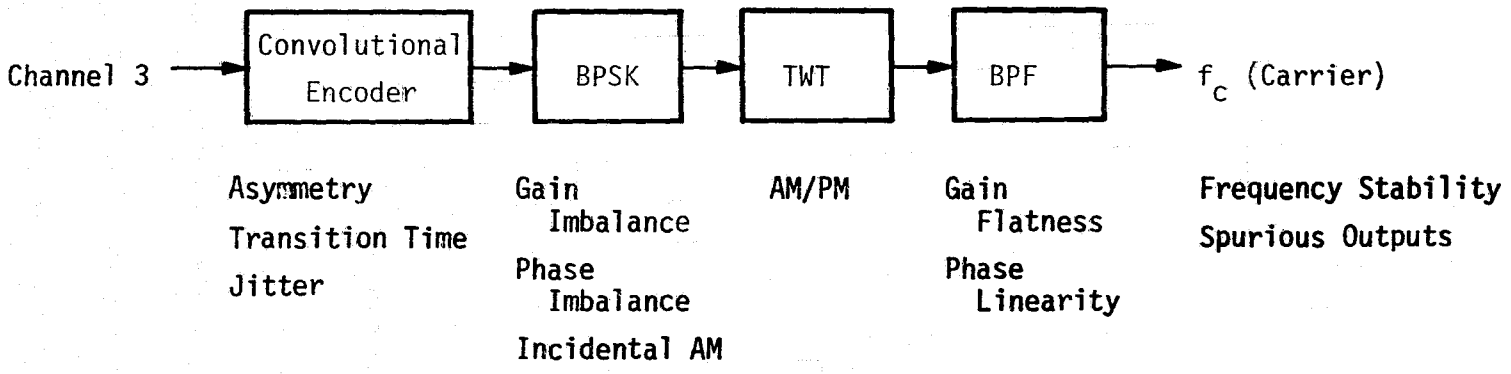


Figure 8. Block Diagram of the I Channel (Channel 3) With Associated Hardware Parameters

The analysis presented in this section was originally developed by STI [15-16] and was checked by Axiomatix. Using this analysis, the effects on performance by choosing system parameters equal to the Rockwell specifications or the Hughes design are discussed. The performance of the QDSB modulation on the Ku-band return link will be analyzed under a follow-on effort to this contract.

## 3.1 Analysis of Cumulative Effect of 14 Parameters on BER Performance

In the following derivation, the data format is assumed to be NRZ-L.

### 3.1.1 Upper Bound on $\Delta E_b/N_0$ for a Given User Parameter

The basis of this BER analysis is the upper bound to the probability of error (or equivalently, $\Delta E_b/N_0$) below.

Let $\{p_i\}$ constitute a probability distribution and $\{u_i\}$ a set of functions of the user parameter. The unconditional bit error probability in the presence of the user parameter degradation is expressed as

$$P_E = \sum_{i=1}^{N} p_i Q\left\{\sqrt{\frac{2E_b}{N_0} u_i}\right\}; \tag{99}$$

$$\sum_{i=1}^{N} p_i = 1.$$

$E_b/N_0$ is the bit-energy-to-noise ratio; we define

$$\rho \triangleq 2E_b/N_0 ; \tag{100}$$

$$Q(x) \triangleq \frac{1}{\sqrt{2\pi}} \int_x^{\infty} \exp(-t^2/2)\, dt ; \tag{101}$$

then,

$$P_E \leq \frac{\exp\left[-(E_b/N_0)D\right]}{\sqrt{2\pi(2E_b/N_0)D}} , \tag{102}$$

where

$$D = \frac{1}{(1+2E_b/N_0)}\left\{1 - 2\ln \sum_{i=1}^{N} p_i \frac{\exp\left(-(E_b/N_0)\,u_i\right)}{\sqrt{u_i}}\right\} \qquad (103)$$

and the SNR degradation is defined as

$$\frac{\Delta E_b}{N_0} \leq 10 \log_{10} (1/D) . \qquad (104)$$

3.1.2 Application of Upper Bound to the Parameters Under Consideration

We now proceed to use the results above by taking the parameters of interest, starting with the gain imbalance and adding one or more parameter at a time. The resulting degradation represents the cumulative effect of the parameters considered up to a given step.

3.1.2.1 Modulator Gain Imbalance ($\eta$)

If G is the channel gain parameter, we have

$$\eta = G_1/G_0 ; \qquad \eta > 1 \text{ (arbitrarily)} ,$$

where the subscripts 0 and 1 denote whether the data bit is -1 or +1, respectively.

Since the average power is fixed at the modulator output,

$$G_0 = \frac{2}{1+\eta} \quad \text{and} \quad G_1 = \frac{2\eta}{1+\eta} .$$

We now use (102) to get an expression for the probability of error:

$$P_E = \frac{1}{2} Q\{\sqrt{\rho G_1}\} + \frac{1}{2} Q\{\sqrt{\rho G_0}\} ;$$

thus,

$$N = 2$$

$$p_1 = 1/2 \qquad u_1 = \frac{2\eta}{1+\eta}$$

$$p_2 = 1/2 \qquad u_2 = \frac{2}{1+\eta}$$

For a nominal probability of error $P_E = 10^{-5}$, $E_b/N_0 = 9.6$ dB (these values are used throughout this section). We can now calculate D in (103) and,

consequently, $\Delta E_b/N_0$.

The other parameters are incorporated and evaluated (insofar as their impact on BER performance is concerned) in a similar fashion.

3.1.2.2 Addition of Data Asymmetry (A)

$N = 4$

$$p_1 = \frac{1}{2} \qquad u_1 = \frac{2\eta}{1+\eta}$$

$$p_2 = \frac{1}{8} \qquad u_2 = \frac{2}{1+\eta}$$

$$p_3 = \frac{1}{4} \qquad u_3 = \left[\left(1 - \frac{A}{2}\right)\sqrt{\frac{2}{1+\eta}} - \frac{A}{2}\sqrt{\frac{2\eta}{1+\eta}}\right]^2$$

$$p_4 = \frac{1}{8} \qquad u_4 = \left[(1 - A)\sqrt{\frac{2}{1+\eta}} - A\sqrt{\frac{2\eta}{1+\eta}}\right]^2$$

where A is the amount of asymmetry present ($A \times 100$ = % asymmetry).

3.1.2.3 Addition of Data Transition Time ($t_r$)

The parameter representing data transition time is the ratio of transition time to bit duration: $\mu = t_r/T$. Two cases arise:

Case A: Data Transition Time Dominates Data Asymmetry

$N = 6$

$$p_1 = \frac{1}{4} \qquad u_1 = \frac{2\eta}{1+\eta}(1 - \beta_1)^2$$

$$p_2 = \frac{1}{8} \qquad u_2 = \frac{2\eta}{1+\eta}(1 - 2\beta_1)^2$$

$$p_3 = \frac{1}{8} \qquad u_3 = \frac{2\eta}{1+\eta}$$

$$p_4 = \frac{1}{4} \qquad u_4 = \frac{2}{1+\eta}(1 - \beta_0)^2$$

$$p_5 = \frac{1}{8} \qquad u_5 = \frac{2}{1+\eta}(1 - 2\beta_0)^2$$

$$p_6 = \frac{1}{8} \qquad u_6 = \frac{2}{1+\eta}$$

with $$\beta_0 = \frac{1}{2}\left[\frac{5}{9}\mu\sqrt{\frac{2}{1+\eta}}\right]\left[1 + \frac{A/2}{\frac{5}{9}\mu\sqrt{\frac{2}{1+\eta}}}\right]^2$$

$$\beta_1 = \frac{1}{2}\left[\frac{5}{9}\mu\sqrt{\frac{2\eta}{1+\eta}}\right]\left[1 - \frac{A/2}{\frac{5}{9}\mu\sqrt{\frac{2\eta}{1+\eta}}}\right]^2$$

Case B: Data Asymmetry Dominates Data Transition Time

$N = 4$

$p_1 = \frac{1}{2}$ $\qquad u_1 = \frac{2\eta}{1+\eta}$

$p_2 = \frac{1}{8}$ $\qquad u_2 = \frac{2}{1+\eta}$

$p_3 = \frac{1}{4}$ $\qquad u_3 = \frac{2}{1+\eta}(1-\beta_3)^2$

$p_4 = \frac{1}{8}$ $\qquad u_4 = \frac{2}{1+\eta}(1-2\beta_3)^2$

with

$$\beta_3 = \frac{1}{2}\left[\frac{5}{9}\mu\sqrt{\frac{2}{1+\eta}}\left(1 + \frac{A}{5/9\,\mu\sqrt{2/(1+\eta)}}\right) + \frac{5}{9}\mu\sqrt{\frac{2\eta}{1+\eta}}\sqrt{\eta}\left(\frac{A}{5/9\,\mu\sqrt{2\eta/(1+\eta)}} - 1\right)\right].$$

Usually, data transition time effects are negligible when data asymmetry is dominant, but not necessarily otherwise.

3.1.2.4 Addition of AM/PM ($\phi_0$)

The AM/PM characteristic is assumed to be linear:

$$\phi_0 = \frac{10\,T_0}{\ln 10} = 4.34\,T_0\ ,$$

where $\phi_0$ represents the nominal AM/PM output phase at the nominal input power level, and $T_0$ is the specified AM/PM value. $T_0$ represents the slope of the AM/PM characteristic at the operating point.

Two cases are considered:

Case A: Data Transition Time Dominates Data Asymmetry

$N = 6$

$$p_1 = \frac{1}{4} \qquad u_1 = \left\{\left(\sqrt{G_1} - \frac{5}{9}\mu\,\beta_A\right)\cos\left[\phi_0(G_1-1)\right] + \frac{5\mu\cos\left[\phi_0(\beta_B-1)\right]\sin\left(\phi_0\beta_C\right)}{9\phi_0}\right\}^2$$

$$p_2 = \frac{1}{8} \qquad u_2 = \left\{\left(\sqrt{G_1} - \frac{10}{9}\mu\,\beta_A\right)\cos\left[\phi_0(G_1-1)\right] + \frac{10\mu\cos\left[\phi_0(\beta_B-1)\right]\sin\left(\phi_0\beta_C\right)}{9\phi_0}\right\}^2$$

$$p_3 = \frac{1}{8} \qquad u_3 = G_1\cos^2\left[\phi_0(G_1-1)\right]$$

$$p_4 = \frac{1}{4} \qquad u_4 = \left\{\left(\sqrt{G_0} - \frac{5}{9}\mu\,\gamma_A\right)\cos\left[\phi_0(G_0-1)\right] + \frac{5\mu\cos\left[\phi_0(\gamma_B-1)\right]\sin\left(\phi_0\gamma_C\right)}{9\phi_0}\right\}^2$$

$$p_5 = \frac{1}{8} \qquad u_5 = \left\{\left(\sqrt{G_0} - \frac{10}{9}\mu\,\gamma_A\right)\cos\left[\phi_0(G_0-1)\right] + \frac{10\mu\cos\left[\phi_0(\gamma_B-1)\right]\sin\left(\phi_0\gamma_C\right)}{9\phi_0}\right\}^2$$

$$p_6 = \frac{1}{8} \qquad u_6 = G_0\cos^2\left[\phi_0(G_0-1)\right]$$

with

$$\beta_A = G_1\left(1 - \frac{A/2}{\frac{5}{9}\mu\sqrt{G_1}}\right)$$

$$\beta_B = \frac{G_1}{2}\left[1 + \left(\frac{A/2}{\frac{5}{9}\mu\sqrt{G_1}}\right)^2\right]$$

$$\beta_C = \frac{G_1}{2}\left[1 - \left(\frac{A/2}{\frac{5}{9}\mu\sqrt{G_1}}\right)^2\right]$$

$$\gamma_A = G_0\left(1 + \frac{A/2}{\frac{5}{9}\mu\sqrt{G_0}}\right)$$

$$\gamma_B = \frac{G_0}{2}\left[1 + \left(\frac{-A/2}{\frac{5}{9}\mu\sqrt{G_0}}\right)^2\right]$$

$$\gamma_C = \frac{G_0}{2}\left[1 - \left(\frac{-A/2}{\frac{5}{9}\mu\sqrt{G_0}}\right)^2\right]$$

Case B: Data Asymmetry Dominates Data Transition Time

$N = 4$

$$p_1 = \frac{1}{2} \qquad u_1 = G_1 \cos^2 [\phi_0(G_1 - 1)]$$

$$p_2 = \frac{1}{8} \qquad u_2 = G_0 \cos^2 [\phi_0(G_0 - 1)]$$

$$p_3 = \frac{1}{4} \qquad u_3 = \left\{\sqrt{G_0} \cos [\phi_0(G_0-1)] + \frac{5\mu \cos [\phi_0(\delta_1-1)] \sin (\phi_0\delta_2)}{9\phi_0} + \frac{5}{9}\mu\,\delta_3 - \frac{A\delta_4}{2}\right\}^2$$

$$p_4 = \frac{1}{8} \qquad u_4 = \left\{\sqrt{G_0} \cos [\phi_0(G_0-1)] + \frac{10\mu \cos [\phi_0(\delta_1-1)] \sin (\phi_0\delta_2)}{9\phi_0} + \frac{10}{9}\mu\,\delta_3 - A\delta_4\right\}^2$$

with

$$\delta_1 = \frac{G_0}{2}\left[1 + \frac{G_1}{G_0}\right]$$

$$\delta_2 = \frac{G_0}{2}\left[1 - \frac{G_1}{G_0}\right]$$

$$\delta_3 = G_1 \cos [\phi_0(G_1 - 1)] - G_0 \cos [\phi_0(G_0 - 1)]$$

$$\delta_4 = \sqrt{G_1} \cos [\phi_0(G_1 - 1)] + \sqrt{G_0} \cos [\phi_0(G_0 - 1)]$$

3.1.2.5 Addition of Remaining Phase Parameters

The remaining phase parameters are divided into

- BPSK phase imbalance ($\phi_1$)
  $\phi_1$ is deterministic and bit dependent.
- Data transition induced PM ($\psi_1$); Spurious PM ($\psi_2$); Phase noise (noncoherent) ($\psi_3$); $\psi_1 + \psi_2 + \psi_3 = \phi_2$
  $\phi_2$ is random and bit independent.

- Phase offset due to carrier frequency instability ($\phi_3$)
  $\phi_3$ is deterministic and bit independent and is given by

$$\phi_3 = \frac{2\pi\Delta f}{K_L},$$

  where $\Delta f$ is the frequency instability term and $K_L$ is the receiver loop velocity gain ($K_L = 10^6$).

Again, two cases arise:

Case A: Data Transition Time Dominates Data Asymmetry

$N = 6$

$$p_1 = \frac{1}{8} \qquad u_1 = G_1 \cos^2 [\phi_0(G_1 - 1) + \phi_c + \phi_3]$$

$$p_2 = \frac{1}{4} \qquad u_2 = \left\{\left(\sqrt{G_1} - \frac{5}{9}\mu\beta_A\right) \cos [\phi_0(G_1 - 1) + \phi_c + \phi_3] + \frac{5\mu \cos [\phi_0(\beta_B - 1) + \phi_c + \phi_3] \sin (\phi_0\beta_C)}{9\phi_0}\right\}^2$$

$$p_3 = \frac{1}{8} \qquad u_3 = \left\{\left(\sqrt{G_1} - \frac{10}{9}\mu\beta_A\right) \cos [\phi_0(G_1 - 1) + \phi_c + \phi_3] + \frac{10\mu \cos [\phi_0(\beta_B - 1) + \phi_c + \phi_3] \sin (\phi_0\beta_C)}{9\phi_0}\right\}^2$$

$$p_4 = \frac{1}{8} \qquad u_4 = G_0 \cos^2 [\phi_0(G_0 - 1) - \phi_c + \phi_3]$$

$$p_5 = \frac{1}{4} \qquad u_5 = \left\{\left(\sqrt{G_0} - \frac{5}{9}\mu\gamma_A\right) \cos [\phi_0(G_0 - 1) - \phi_c + \phi_3] + \frac{5\mu\{\cos [\phi_0(\gamma_B - 1) + \phi_3] \sin (\phi_0\gamma_C - \phi_c) + \cos (\phi_3 - \phi_0) \sin (\phi_c)\}}{9\phi_0}\right\}^2$$

$$p_6 = \frac{1}{8} \qquad u_6 = \left\{\left(\sqrt{G_0} - \frac{10}{9}\mu\gamma_A\right) \cos [\phi_0(G_0 - 1) - \phi_c + \phi_3] + \frac{10\mu\{\cos [\phi_0(\gamma_B - 1) + \phi_3] \sin (\phi_0\gamma_C - \phi_c) + \cos (\phi_3 - \phi_0) \sin (\phi_c)\}}{9\phi_0}\right\}^2$$

with $\phi_c = \frac{\phi_1}{2} + \phi_2$

and $\beta_A$, $\beta_B$, $\beta_C$, $\gamma_A$, $\gamma_B$, $\gamma_C$ as given in Case A of 3.1.2.4.

Case B: Data Asymmetry Dominates Data Transition Time

N = 4

$$p_1 = \frac{1}{2} \quad u_1 = G_1 \cos^2 [\phi_0(G_1 - 1) + \phi_c + \phi_3]$$

$$p_2 = \frac{1}{8} \quad u_2 = G_0 \cos^2 [\phi_0(G_0 - 1) - \phi_c + \phi_3]$$

$$p_3 = \frac{1}{4} \quad u_3 = \left\{\sqrt{G_0} \cos [\phi_0(G_0 - 1) - \phi_c + \phi_3] + \frac{5}{9}\mu\,\delta_3' - \frac{A}{2}\,\delta_4' + \frac{5\mu\{\cos [\phi_0(\delta_1 - 1) + \phi_3] \sin (\phi_0\delta_2 - \phi_c) + \cos (\phi_3 - \phi_0) \sin (\phi_c)\}}{9\phi_0}\right\}^2$$

$$p_4 = \frac{1}{8} \quad u_4 = \left\{\sqrt{G_0} \cos [\phi_0(G_0 - 1) - \phi_c + \phi_3] + \frac{10}{9}\mu\,\delta_3' - A\,\delta_4' + \frac{10\mu\{\cos [\phi_0(\delta_1 - 1) + \phi_3] \sin (\phi_0\delta_2 - \phi_c) + \cos (\phi_3 - \phi_0) \sin (\phi_c)\}}{9\phi_0}\right\}^2$$

where $\delta_1$, $\delta_2$, $\delta_3$ are defined in Case B of 3.1.2.4

and $\delta_3' = G_1 \cos [\phi_0(G_1 - 1) + \phi_c + \phi_3] - G_0 \cos [\phi_0(G_0 - 1) - \phi_c + \phi_3]$

$$\delta_4' = \sqrt{G_1} \cos [\phi_0(G_1 - 1) + \phi_c + \phi_3] + \sqrt{G_0} \cos [\phi_0(G_0 - 1) - \phi_c + \phi_3]$$

3.1.2.6 Addition of Data Bit Jitter ($\Delta_D$)

($\Delta_D \times 100$ = peak value)

Data jitter is the random component of data asymmetry specified as being less than some peak value (in %). The results of 3.1.2.5 apply, with each A replaced by $A + \Delta_D$ in every $u_i$.

3.1.2.7 Addition of Gain Flatness ($G_f$) and Phase Nonlinearity (b)

Again, the results of 3.1.2.5 apply, with the following modifications:

For each $p_i$, we associate $p_{ij}$ $(j = 1,2)$ such that

$$p_{i1} = p_{i2} = p_i/2 .$$

Similarly, for each $u_i$, we associate

$$u_{i1} = \left(\sqrt{u_i} + \sqrt{(a^2 + b^2)/2}\right)^2$$

$$u_{i2} = \left(\sqrt{u_i} - \sqrt{(a^2 + b^2)/2}\right)^2$$

and, in the expression for D, the sum over N is replaced by the double sum below:

$$\sum_{i=1}^{N} \sum_{j=1}^{2} p_{ij} \frac{\exp\left(-(E_b/N_0)\, u_{ij}\right)}{\sqrt{u_{ij}}}$$

and $$a = \frac{G_f - 1}{G_f + 1} .$$

3.1.2.8 Addition of Incidental AM (m)

$(m \times 100 = m\%)$

The results of 3.1.2.5 apply, with each $u_i$ multiplied by

$$K_{AM} = \frac{1}{1 + (m^2/2)} .$$

3.1.2.9 Addition of Spurious Outputs ($P_s$)

The results of 3.1.2.5 apply, with each $u_i$ multiplied by

$$\frac{1}{1 + \pi(E_b/N_0)\, P_s} ,$$

where $P_s$ is the ratio of total power in the spurs to the desired signal power.

## 3.2 Computations and Discussion of Results

The results of Subsections 3.1.1 and 3.1.2 were numerically computed and are presented in Table 1. Each degradation represents the

Table 1. Comparison of TDRSS User Constraints and HAC Specifications With Corresponding Degradations

| Parameters | TDRSS User Constraint | Cumulative Degradation (dB) | HAC Specification | Cumulative Degradation (dB) | | Comments |
|---|---|---|---|---|---|---|
| | | | | $\mu > A$ | $A > \mu$ | |
| Modulator Gain Imbalance ($\eta$) | 0.25 dB | 0.017 | 0.5 dB | 0.067 | 0.067 | Peak |
| Data Asymmetry (A) | 3% | 0.224 | 5% | | 0.508 | * |
| | | | 3% | 0.303 | | |
| Data Transition ($\mu$) | 5% | 0.251 | 3% | | 0.497 | * |
| | | | 5% | 0.324 | | |
| AM/PM ($T_0$) | 10°/dB | 0.258 | 5°/dB | 0.327 | 0.570 | $\phi_0 = 4.34\ T_0$ |
| Modulator Phase Imbalance ($\phi_1$) | 3° | 0.407 | 5° | 0.481 | 0.647 | Peak |
| Data Transition Induced PM ($\psi_1$) | 3° | | 3° | | | At transition density = 100% |
| Spurious PM ($\psi_2$) | 2° | | 2° | | | RMS |
| Phase Noise Noncoherent ($\psi_3$) | 1 Hz - 10 Hz $\leq$ 15°<br>100 Hz - 50 MHz $\leq$ 2° | | 1 Hz - 1 kHz $\leq$ 17°<br>1 kHz - 50 MHz $\leq$ 3° | | | RMS |
| Frequency Stability ($\phi_3$) | $3 \times 10^{-7}$ | | $3 \times 10^{-7}$ | | | 48 hours Average time |
| Data Bit Jitter ($\Delta_D$) | 0.1% | 0.410 | 2% | 0.563 | 0.878 | * |
| Gain Flatness ($G_f$) | 0.3 dB | 0.551 | 0.3 dB | 1.042 | 0.922 | ±70 MHz |
| Phase Nonlinearity (b) | 3° | | 7° | | | Peak |
| Incidental AM (m) | 5% | 0.556 | 5% | 1.047 | 0.927 | Peak |
| Spurious Outputs ($P_s$) | -30 dBc | 0.684 | -50 dBc | 1.054 | 0.933 | Within Data BW |

*See text

addition of one more parameter or a group of parameters. The effect of the phase parameters is substantial because the analysis treats them as a single composite term.

For noncoherent phase noise, $\phi_3$, the smaller specification was used for computations because the tracking loop bandwidth will certainly be greater than 100 Hz and all phase noise below that range will be tracked out. Using the higher specification would result in a degradation of 1 dB greater than the tabulated value.

For the parameters associated with data bit timing (asymmetry, transition time, and jitter), the HAC specification of less than or equal to 10% is for a composite asymmetry which includes transition time and jitter as well:

$$A + \mu + \Delta_D \leq 10\%,$$

where $A$ = asymmetry (steady-state)

$\Delta_D$ = jitter

$\mu = t_r/T$, with $t_r$ = (0-90%) transition time and $T$ = symbol time.

The computations for the HAC specifications were done for both cases, namely, data asymmetry dominates data transition time ($A > \mu$) and vice versa.

Where $\mu > A$, the impacts of $\mu = 5\%$, $A = 3\%$ and $\Delta_D = 2\%$ are presented in Table 1; also, the effect of varying A is shown graphically in Figure 9 (the results are relative to a gain imbalance of 0.5 dB).

Figure 10 shows the effect of varying A on the cumulative degradation (relative to $\mu = 5\%$ and $\Delta_D = 2\%$); it can be seen that the two curves have approximately the same slope except at the high values of A where the individual impact is more pronounced than the impact in combination.

When $A > \mu$, the results for $A = 5\%$, $\mu = 3\%$ and $\Delta_D = 2\%$ are tabulated; varying $\mu$ (relative to $A = 5\%$) was found to have no appreciable effect.

From Table 1, we see that, in the case where data transition time dominates data asymmetry, the combined impact of gain flatness ($G_f$) and phase nonlinearity (b) is substantial and a net difference of 0.37 dB exists between the user constraints and the HAC specifications.

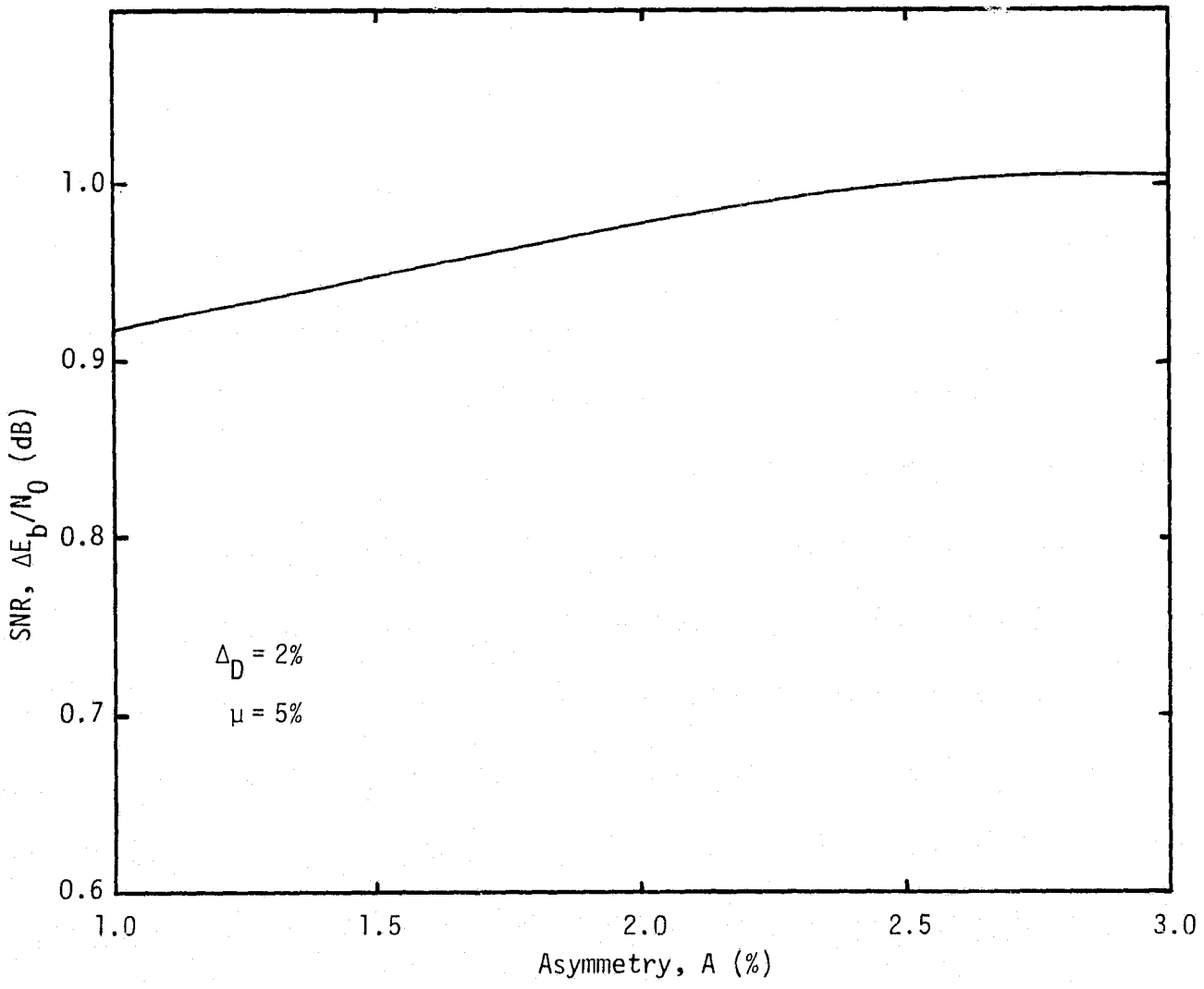


Figure 9. Variation of Degradation in SNR as a Function of Asymmetry When Data Transition Time Dominates Data Asymmetry (Relative to $\eta = 0.5$ dB)

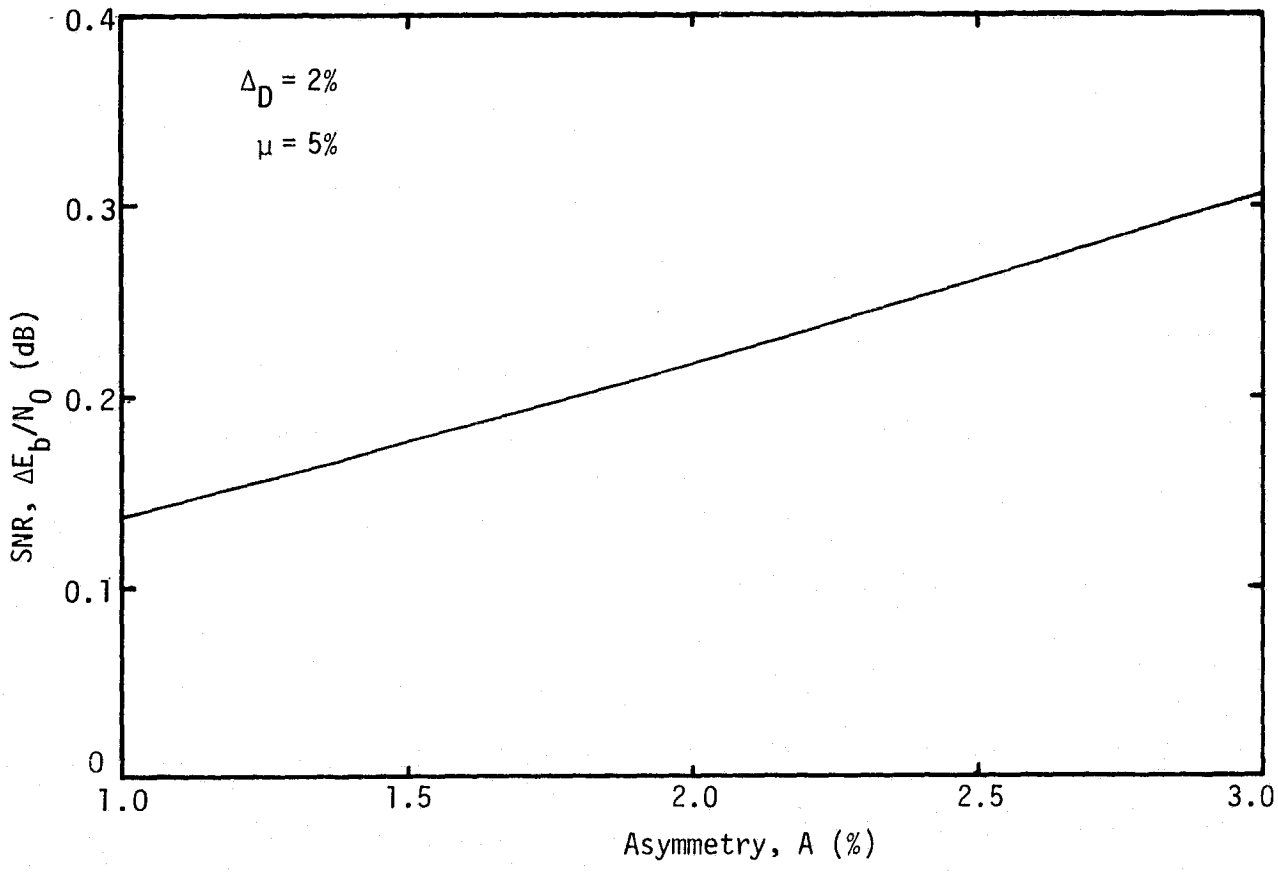


Figure 10. Variation of Cumulative Degradation in SNR as a Function of Asymmetry When Data Transition Time Dominates Data Asymmetry

In the case where data asymmetry dominates data transition time, the impacts of asymmetry (A) and data bit jitter ($\Delta_D$) are substantial, and the net difference between the constrained values and the HAC specification is 0.249 dB only.

Possible trade-off considerations can be based on these numbers.

## 3.3 Degradation Introduced by the QPSK Modulation for the Subcarrier (Channels 1 and 2)

We now consider degradation due to the subcarrier modulator. The procedure here is similar to that of Subsections 3.1.1 and 3.1.2 and differs only the expressions of the probabilities of error.

The parameters considered are:

- Modulator gain imbalance ($\eta$)
- BPSK phase imbalance ($\phi_I$,$\phi_Q$)
- I/Q phase imbalance ($\phi$).

The effects of these three parameters are derived in combination.

Let $\eta$ denote the I/Q gain imbalance from nominal, $G_I$ and $G_Q$ the I and Q channel gain parameters,

$$G_{I1} = \eta_I G_{I0} \qquad \eta_I > 1 \text{ (arbitrarily)}$$

$$G_{Q1} = \eta_Q G_{Q0} \qquad \eta_Q > 1 \text{ (arbitrarily)},$$

$\eta_I$ and $\eta_Q$ represent the individual channel gain imbalances and the subscripts 1 and 0 denote whether the data bit is -1 or +1. We have

$$r = A_Q/A_I$$

$$G_{I0} = \frac{2}{1+\eta_I} \quad ; \quad G_{I1} = \frac{2\eta_I}{1+\eta_I}$$

$$G_{Q0} = \frac{2}{1+\eta_Q} \quad ; \quad G_{Q1} = \frac{2\eta_Q}{1+\eta_Q}$$

For the I channel (Channel 2):

$$N = 4$$

$$p_1 = \frac{1}{4} \qquad u_1 = \left(\sqrt{G_{I1}}\, C_1 - r\sqrt{\eta G_{Q1}}\, S_1\right)^2$$

$$p_2 = \frac{1}{4} \qquad u_2 = \left(\sqrt{G_{I1}}\, C_1 + r\sqrt{\eta G_{Q0}}\, S_0\right)^2$$

$$p_3 = \frac{1}{4} \qquad u_3 = \left(\sqrt{G_{I0}}\, C_0 + r\sqrt{\eta G_{Q1}}\, S_1\right)^2$$

$$p_4 = \frac{1}{4} \qquad u_4 = \left(\sqrt{G_{I0}}\, C_0 - r\sqrt{\eta G_{Q0}}\, S_0\right)^2$$

where $C_0 = \cos\left(\frac{\phi}{2} - \frac{\phi_I}{2} + \theta_e\right)$

$$C_1 = \cos\left(\frac{\phi}{2} + \frac{\phi_I}{2} + \theta_e\right)$$

$$S_0 = \sin\left(\frac{\phi}{2} + \frac{\phi_Q}{2} - \theta_e\right)$$

$$S_1 = \sin\left(\frac{\phi}{2} - \frac{\phi_Q}{2} - \theta_e\right)$$

and $\theta_e = \frac{1}{4}\left[\theta_4(r\sqrt{\eta}\,;\phi) - \theta_4(r;0)\right]$,

with

$$\theta_4(r;\phi) = \tan^{-1}\left[\frac{(r^2 - r^{-2})\sin 2\phi - 4(r - r^{-1})\cos\phi}{(r^2 + r^{-2})\cos 2\phi + 4(r + r^{-1})\sin\phi - 6}\right].$$

Similarly, for the Q channel (Channel 1):

$$N = 4$$

$$p_1 = \frac{1}{4} \qquad u_1 = \left(r\sqrt{\eta G_{Q1}}\, \hat{C}_1 - \sqrt{G_{I1}}\, \hat{S}_1\right)^2$$

$$p_2 = \frac{1}{4} \qquad u_2 = \left(r\sqrt{\eta G_{Q1}}\, \hat{C}_1 + \sqrt{G_{I0}}\, \hat{S}_0\right)^2$$

$$p_3 = \frac{1}{4} \qquad u_3 = \left(r\sqrt{\eta G_{QO}}\,\hat{C}_0 + \sqrt{G_{I1}}\,\hat{S}_1\right)^2$$

$$p_4 = \frac{1}{4} \qquad u_4 = \left(r\sqrt{\eta G_{QO}}\,\hat{C}_0 + \sqrt{G_{IO}}\,\hat{S}_0\right)^2$$

where $\hat{C}_0 = \cos\left(\frac{\phi}{2} + \frac{\phi_Q}{2} - \theta_e\right)$

$$\hat{C}_1 = \cos\left(\frac{\phi}{2} - \frac{\phi_Q}{2} - \theta_e\right)$$

$$\hat{S}_0 = \sin\left(\frac{\phi}{2} - \frac{\phi_I}{2} + \theta_e\right)$$

$$\hat{S}_1 = \sin\left(\frac{\phi}{2} + \frac{\phi_I}{2} + \theta_e\right) .$$

An example computation was done for the I channel when

$$\eta_I = \eta_Q = 0.25 \text{ dB}$$

$$\phi_I = \phi_Q = \phi = 3°$$

$$r = 0.5 .$$

A degradation of 0.08 dB resulted from the parameters in combination.

The results presented above for BPSK and QPSK modulations will be extended to QDSB modulation in order to get the exact cumulative degradation for the Shuttle Ku-band return link in the follow-on effort.

# 4.0 S-BAND TDRSS GROUND STATION FALSE LOCK EVALUATION

For the Shuttle-unique S-band demodulator, Motorola has proposed an active arm filter I-Q loop in which the carrier tracking loop and the bit synchronizer are interactive. Furthermore, following the integrate-and-dump (I&D) arm filter, the in-phase channel is hard-limited before multiplication with the quadrature phase arm filter output. This type of loop is referred to as a decision-directed (or polarity-type) I-Q loop. While the polarity-type I-Q loop provides a simpler implementation of the multiplier (especially if it is implemented by a digital multiplier as is proposed by Motorola), the false lock susceptibility of the Costas loop is drastically changed. This section summarizes the results of an evaluation of the Motorola-proposed loop in terms of its false lock susceptibility.

The true lock tracking behavior of I-Q and decision-directed I-Q loops is well-documented [8,17]. The term "true lock" refers here to the situation where the loop locks up with the VCO frequency identical to that of the input signal. It is also possible to lock up a Costas or I-Q loop when the VCO frequency is offset from that of the input signal. This situation is referred to as false lock and, depending upon the particular loop configuration, can arise from data-dependent and/or data-independent causes. Data-dependent false lock or false lock to a data sideband has recently received considerable attention in the literature [18-25]. In particular, it has been shown that, for Costas or I-Q loops, false lock to a data sideband occurs when the frequency difference between the VCO and the input signal is an integer multiple of half the data rate. When the I-Q loop is of the decision-directed type, then a data-independent type of false lock occurs which is quite different in behavior than the data-dependent false lock discussed in [18-25]. This data-independent type of false lock has previously been observed in the data-aided loop [26] which was implemented as a sampled-data version of a decision-directed I-Q loop similar to the proposed Motorola loop.

In this section, the theory is developed for the false lock tracking behavior of decision-directed I-Q loops of both the continuous (integrate-and-dump arm filters followed by sample-and-hold circuits) and the sampled data (sampled phase detector outputs and accumulator-type arm filters) types. The results for the latter type are compared with the experimental results for the data-aided loop [26] and shown to produce good agreement.

## 4.1 Continuous Loop Model

We begin our analysis by considering the continuous-type decision-directed I-Q loop illustrated in Figure 11. By "continuous," we refer here to the fact that the in-phase and quadrature phase detector outputs are continuously applied to the integrate-and-dump arm filters as opposed to sampled versions of these outputs as would be the case in the sampled data I-Q loop to be discussed in the next section. The input signal $s[t,\theta(t)]$ is assumed to be a biphase modulated carrier of the form*

$$s[t,\theta(t)] = \sqrt{2S}\, m(t) \sin [\omega_0 t + \theta(t)] \tag{105}$$

where S is the average signal power, $m(t)$ is a binary modulation (a $\pm 1$ digital waveform) with arbitrary statistics (for example, it could be an all +1 or all -1 sequence which are equivalent to no data at all), $\omega_0$ is the radian carrier frequency, and $\theta(t)$ is the received carrier phase.

For the true lock case, the in-phase and quadrature reference signals $r_s(t)$ and $r_c(t)$, respectively, would be given by

$$r_s(t) = \sqrt{2}\, K_1 \sin [\omega_0 t + \hat{\theta}(t)]$$

$$r_c(t) = \sqrt{2}\, K_1 \cos [\omega_0 t + \hat{\theta}(t)] \tag{106}$$

where $\hat{\theta}(t)$ is the VCO's estimate of $\theta(t)$ and $K_1^2$ is the reference signal power. In the false lock mode, one would have

$$r_s(t) = \sqrt{2}\, K_1 \sin [(\omega_0 - \omega_f)t + \hat{\theta}(t)]$$

$$r_c(t) = \sqrt{2}\, K_1 \cos [(\omega_0 - \omega_f)t + \hat{\theta}(t)] \tag{107}$$

where $\omega_f$ is the false lock radian frequency as yet to be determined.

Denoting the in-phase and quadrature phase detector (multiplier) gains by $K_m$, then using (105) and (107), the output $\varepsilon_c(t)$ of the quadrature phase detector is (ignoring second-harmonic terms)

---

*To illustrate the false lock phenomenon in a simple, clear manner, the analysis presented here assumes the absence of additive noise at the input. The additional complication introduced by including the effects of additive noise can be handled in a manner analogous to the development in [20].

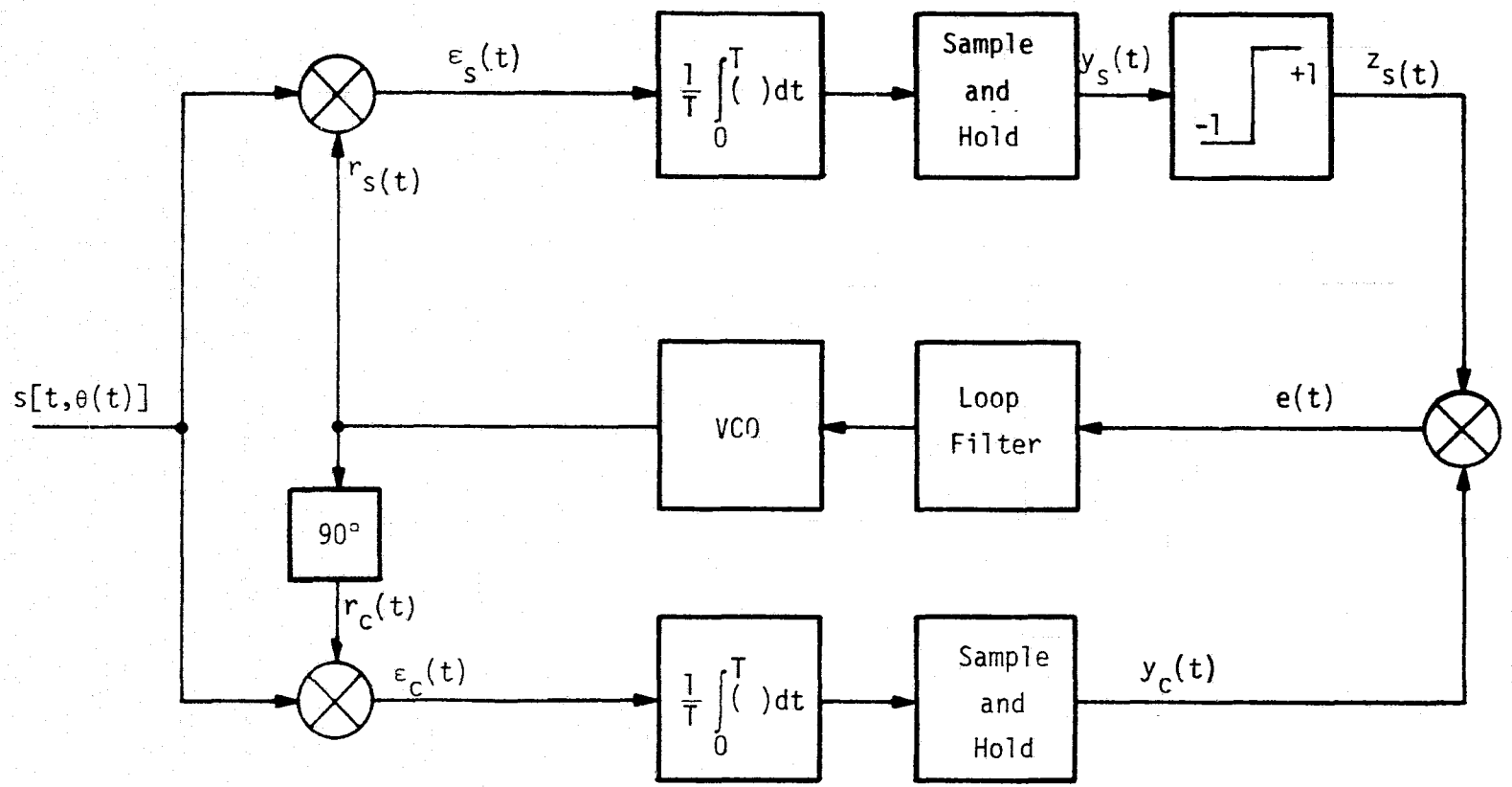


Figure 11. A Continuous-Type Decision-Directed I-Q Loop

$$\varepsilon_c(t) = K_m\, s[t,\theta(t)]\ \sqrt{2}\, K_1 \cos\,[(\omega_0 - \omega_f)t + \theta(t)]$$

$$= K_1 K_m\ \sqrt{S}\, m(t) \sin\,[\omega_f t + \phi(t)] \tag{108}$$

while the in-phase arm phase detector output is

$$\varepsilon_s(t) = K_m\, s[t,\theta(t)]\ \sqrt{2}\, K_1 \sin\,[(\omega_0 - \omega_f)t + \hat{\theta}(t)]$$

$$= K_1 K_m\ \sqrt{S}\, m(t) \cos\,[\omega_f t + \phi(t)] \tag{109}$$

where $\phi(t) \triangleq \theta(t) - \hat{\theta}(t)$ is the loop phase error.

The digital modulation m(t) may be represented as

$$m(t) = \sum_{k=-\infty}^{\infty} a_k\, p(t - kT) \tag{110}$$

where $a_k = \pm 1$ is the data symbol in the kth symbol interval $kT \le t \le (k+1)T$, and p(t) is the symbol pulse shape corresponding to NRZ coding, namely*

$$p(t) = \begin{cases} 1; & 0 \le t \le T \\ 0; & \text{elsewhere} \end{cases} \tag{111}$$

Thus, after lowpass filtering with the in-phase and quadrature phase integrate-and-dump arm filters, the corresponding sample-and-hold outputs become, respectively,

$$y_s(t) = K_1 K_m \sqrt{S} \sum_{k=-\infty}^{\infty} a_{k-1}\, p(t-kT) \left[\frac{1}{T}\int_{(k-1)T}^{kT} \cos\,(\omega_f t+\phi)\, dt\right]$$

$$= K_1 K_m \sqrt{S} \sum_{k=-\infty}^{\infty} a_{k-1}\, p(t-kT) \left[\frac{1}{\omega_f T}\left\{\sin\,(\omega_f kT+\phi) - \sin\,\left(\omega_f(k-1)T+\phi\right)\right\}\right] \tag{112}$$

and

$$y_c(t) = K_1 K_m \sqrt{S} \sum_{k=-\infty}^{\infty} a_{k-1}\, p(t-kT) \left[\frac{1}{T}\int_{(k-1)T}^{kT} \sin\,(\omega_f t+\phi)\, dt\right]$$

$$= -K_1 K_m \sqrt{S} \sum_{k=-\infty}^{\infty} a_{k-1}\, p(t-kT) \left[\frac{1}{\omega_f T}\left\{\cos\,(\omega_f kT+\phi) - \cos\,\left(\omega_f(k-1)T+\phi\right)\right\}\right] \tag{113}$$

---

*NRZ coding is assumed throughout this section, since, for this case, the integrate-and-dump filters of Figure 11 are equivalent to matched filters. The results presented for NRZ, however, are exactly the same as for Manchester coded data when the pulse shape is included in the integration circuit.

Passing $y_s(t)$ through the hard limiter results in

$$z_s(t) \triangleq \text{sgn}\left[y_s(t)\right]$$

$$= \sum_{k=-\infty}^{\infty} p(t-kT)\ \text{sgn}\left[\frac{a_{k-1}}{\omega_f T}\left\{\sin(\omega_f kT+\phi) - \sin\left(\omega_f(k-1)T+\phi\right)\right\}\right]$$

$$= \text{sgn}\left\{\frac{1}{\omega_f T}\right\} \sum_{k=-\infty}^{\infty} p(t-kT)\ \text{sgn}\left\{a_{k-1}\right\}\ \text{sgn}\left\{\sin(\omega_f kT+\phi) - \sin\left(\omega_f(k-1)T+\phi\right)\right\} \quad (114)$$

Finally, multiplying (113) and (114) gives the loop error e(t), namely,

$$e(t) = y_c(t)\ z_s(t) = -K_1 K_m \sqrt{S}\left|\frac{1}{\omega_f T}\right| \sum_{k=-\infty}^{\infty} A_k\ p(t - kT) \quad (115)$$

where

$$A_k \triangleq \left[\cos\ (\omega_f kT+\phi) - \cos\ \left(\omega_f(k-1)T+\phi\right)\right]\ \text{sgn}\ \left[\sin\ (\omega_f kT+\phi) - \sin\ \left(\omega_f(k-1)T+\phi\right)\right] \quad (116)$$

and we have also made use of the fact that

$$a_{k-1}\ \text{sgn}\left[a_{k-1}\right] = \left|a_{k-1}\right| = 1 \qquad \text{for all } k \quad (117)$$

We note that e(t) is totally independent of the data sequence $\{a_k\}$.

Recalling the trigonometric identities

$$\sin A - \sin B = 2 \sin\left(\frac{A-B}{2}\right) \cos\left(\frac{A+B}{2}\right)$$

$$\cos A - \cos B = -2 \sin\left(\frac{A-B}{2}\right) \sin\left(\frac{A+B}{2}\right) \quad (118)$$

the expression for $A_k$ in (116) simplifies to

$$A_k = -2\left|\sin\left(\frac{\omega_f T}{2}\right)\right| \sin\left[\left(k - \frac{1}{2}\right)\omega_f T + \phi\right]\ \text{sgn}\left\{\cos\left[\left(k-\frac{1}{2}\right)\omega_f T + \phi\right]\right\} \quad (119)$$

If the loop is to false lock at a given frequency offset $\omega_f$, we must demonstrate that the time average of e(t) denoted by $\langle e(t)\rangle$ produces an S-curve (an odd function of $\phi$) about some steady-state phase error value, say $\phi_0$. Thus, equivalently, we must examine the conditions under which

$$\frac{\langle e(t)\rangle}{K_1 K_m \sqrt{S}} = \left| \frac{\sin\left(\frac{\omega_f T}{2}\right)}{\frac{\omega_f T}{2}} \right| \lim_{n\to\infty} \left(\frac{1}{2n+1}\right) \sum_{k=-n}^{n} \sin\left[\left(k-\frac{1}{2}\right)\omega_f T + \phi\right] \times \operatorname{sgn}\left\{\cos\left[\left(k-\frac{1}{2}\right)\omega_f T + \phi\right]\right\} \quad (120)$$

is nonzero except where $\phi = \phi_0$.

The approach taken here is to expand the function $\sin\theta \operatorname{sgn}[\cos\theta]$ in a Fourier series and evaluate the limit required in (120) for each term in the series. Thus,

$$\sin\theta \operatorname{sgn}[\cos\theta] = (\sin\theta)\left[\frac{4}{\pi}\sum_{\ell=0}^{\infty}\frac{(-1)^\ell}{2\ell+1}\cos[(2\ell+1)\theta]\right]$$

$$= \frac{2}{\pi}\sum_{\ell=0}^{\infty}\frac{(-1)^\ell}{2\ell+1}\left\{\sin[(2\ell+2)\theta] - \sin(2\ell\theta)\right\} \quad (121)$$

Letting $m = \ell + 1$ in the first summation in (121) and then combining the two summations yields

$$\sin\theta \operatorname{sgn}[\cos\theta] = -\frac{2}{\pi}\sum_{m=1}^{\infty}(-1)^m\left[\frac{1}{2m-1}+\frac{1}{2m+1}\right]\sin(2m\theta)$$

$$= \frac{4}{\pi}\sum_{m=1}^{\infty}(-1)^{m-1}\left(\frac{2m}{4m^2-1}\right)\sin(2m\theta) \quad (122)$$

Letting $\theta = \left(k-\frac{1}{2}\right)\omega_f T + \phi$ in (122), then (120) becomes

$$\frac{\langle e(t)\rangle}{K_1 K_m \sqrt{S}} = \left| \frac{\sin\left(\frac{\omega_f T}{2}\right)}{\frac{\omega_f T}{2}} \right| \frac{4}{\pi}\sum_{m=1}^{\infty}(-1)^{m-1}\left(\frac{2m}{4m^2-1}\right)$$

$$\times \left\{\left[\lim_{n\to\infty}\left(\frac{1}{2n+1}\right)\sum_{k=-n}^{n}\sin\left[(2k-1)m\omega_f T\right]\right]\cos(2m\phi)\right.$$

$$\left. + \left[\lim_{n\to\infty}\left(\frac{1}{2n+1}\right)\sum_{k=-n}^{n}\cos\left[(2k-1)m\omega_f T\right]\right]\sin(2m\phi)\right\} \quad (123)$$

The two limiting sums in (123) are evaluated as follows:

$$\lim_{n\to\infty}\left(\frac{1}{2n+1}\right)\sum_{k=-n}^{n}\sin\left[(2k-1)m\omega_f T\right]=0$$

$$\lim_{n\to\infty}\left(\frac{1}{2n+1}\right)\sum_{k=-n}^{n}\cos\left[(2k-1)m\omega_f T\right]=\lim_{n\to\infty}\frac{1}{n}\sum_{k=1}^{n}\cos\left[(2k-1)m\omega_f T\right]$$

$$=\lim_{n\to\infty}\frac{1}{2n}\left(\frac{\sin 2n\, m\omega_f T}{\sin m\omega_f T}\right)$$

$$=\begin{cases}-1;\ m|\omega_f T|=j_m\pi,\ j_m \text{ an odd integer}\\ +1;\ m|\omega_f T|=j_m\pi,\ j_m \text{ an even integer}\\ 0;\ \text{otherwise}\end{cases}\qquad(124)$$

Thus, $\langle e(t)\rangle$ of (123) will be nonzero only when

$$|\omega_f T|=\gamma\pi\qquad(125)$$

where $\gamma$ is a rational number. Equivalently, if $\Delta_f \triangleq \omega_f/2\pi$, then the false lock frequencies (in Hz) relative to the nominal VCO carrier frequency can potentially occur at <u>any rational multiple of half the data rate</u>, i.e.,

$$|\Delta_f|=\gamma\left(\frac{1}{2T}\right)\qquad(126)$$

Substituting (125) and (124) into (123) gives and expression for the false lock voltage (normalized to the loop gain), namely,

$$\frac{\langle e(t)\rangle}{K_1K_m\sqrt{S}}=\left|\frac{\sin\left(\frac{\gamma\pi}{2}\right)}{\frac{\gamma\pi}{2}}\right|\frac{4}{\pi}\sum_{\{m\}}(-1)^{m-1}(-1)^{m\gamma}\left(\frac{2m}{4m^2-1}\right)\sin(2m\phi)\qquad(127)$$

where $\{m\}$ is defined as the set of integer values of $m$ such that $m\gamma = j_m$, $j_m$ any integer (different for each $m$).

With regard to the values of $\gamma$, two distinct situations can occur. Either $\gamma$ is itself an integer or can be expressed as a ratio of integers $p/q$, where $p$ and $q$ are relatively prime.

4.1.1 $\gamma = n$ (n an integer)

When $\gamma = n$, the set $\{m\}$ such that $mn = j_m$, $j_m$ any integer, clearly contains <u>all</u> the positive integers. Thus, for this case, (127) simplifies to

$$\frac{\langle e(t)\rangle}{K_1 K_m \sqrt{S}} = \left|\frac{\sin\left(\frac{n\pi}{2}\right)}{\frac{n\pi}{2}}\right| \frac{4}{\pi} \sum_{m=1}^{\infty} (-1)^{m-1}(-1)^{mn} \left(\frac{2m}{4m^2-1}\right) \sin(2m\phi)$$

$$= \begin{cases} -\left(\frac{2}{n\pi}\right) \frac{4}{\pi} \sum_{m=1}^{\infty} \left(\frac{2m}{4m^2-1}\right) \sin(2m\phi)\ ; & n \text{ odd} \\ 0\ ; & n \text{ even} \end{cases} \qquad (128)$$

To see how (128) can be put in closed form, consider the Fourier series of the function $\cos\phi\ \mathrm{sgn}[\sin\phi]$, namely,

$$\cos\phi\ \mathrm{sgn}[\sin\phi] = (\cos\phi)\frac{4}{\pi} \sum_{\ell=0}^{\infty} \left(\frac{1}{2\ell+1}\right) \sin[2\ell+1)\phi]$$

$$= \frac{2}{\pi} \sum_{\ell=0}^{\infty} \left(\frac{1}{2\ell+1}\right) \left\{\sin[(2\ell+2)\phi] + \sin(2\ell\phi)\right\} \qquad (129)$$

Making similar shifts of the summation index to those employed in deriving (122) from (121), we obtain the desired result

$$\cos\phi\ \mathrm{sgn}[\sin\phi] = \frac{4}{\pi} \sum_{m=1}^{\infty} \left(\frac{2m}{4m^2-1}\right) \sin(2m\phi) \qquad (130)$$

Substituting (130) into (128) gives the false lock behavior of the continuous decision-directed I-Q loop at frequency offsets (relative to the nominal VCO carrier frequency) which are integer multiples of half the data rate, namely (see Figure 12a),

$$\frac{\langle e(t)\rangle}{K_1 K_m \sqrt{S}} = \begin{cases} -\frac{2}{n\pi} \cos\phi\ \mathrm{sgn}[\sin\phi]; & n \text{ odd} \\ 0\ ; & n \text{ even} \end{cases} \qquad (131)$$

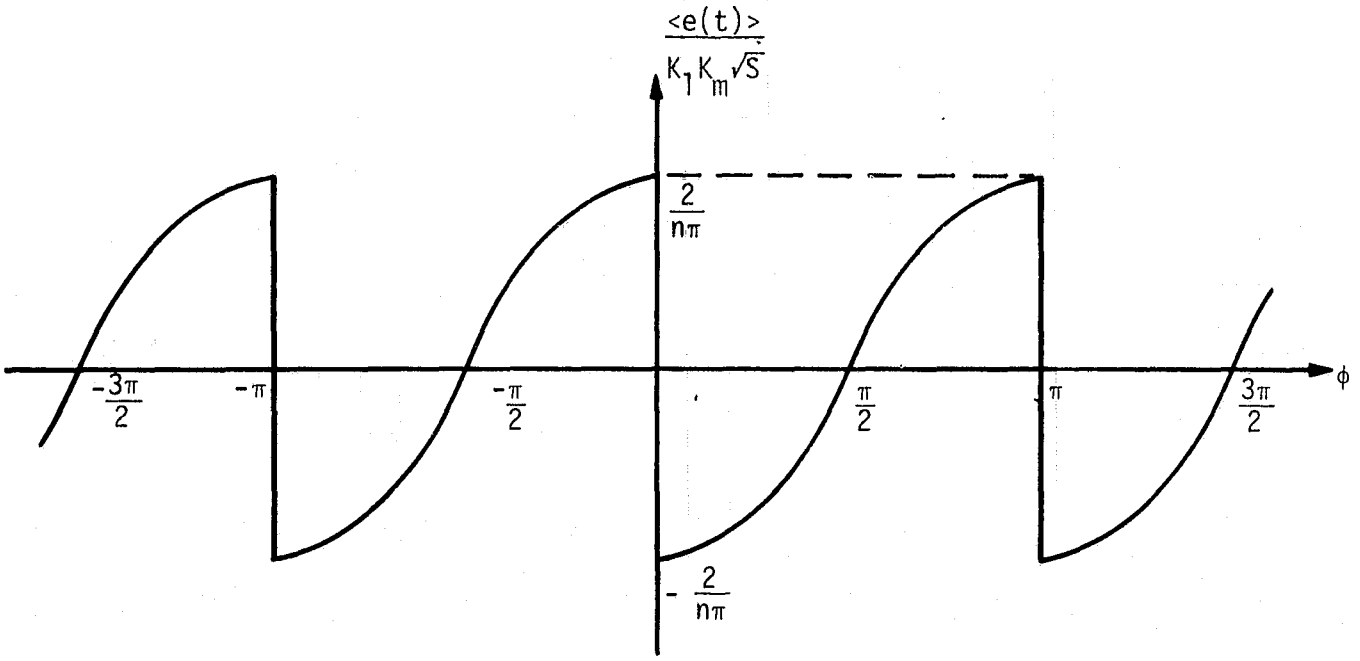


Figure 12a. S-Curve for False Lock at nth Multiple of Half the Data Rate (n/2T)

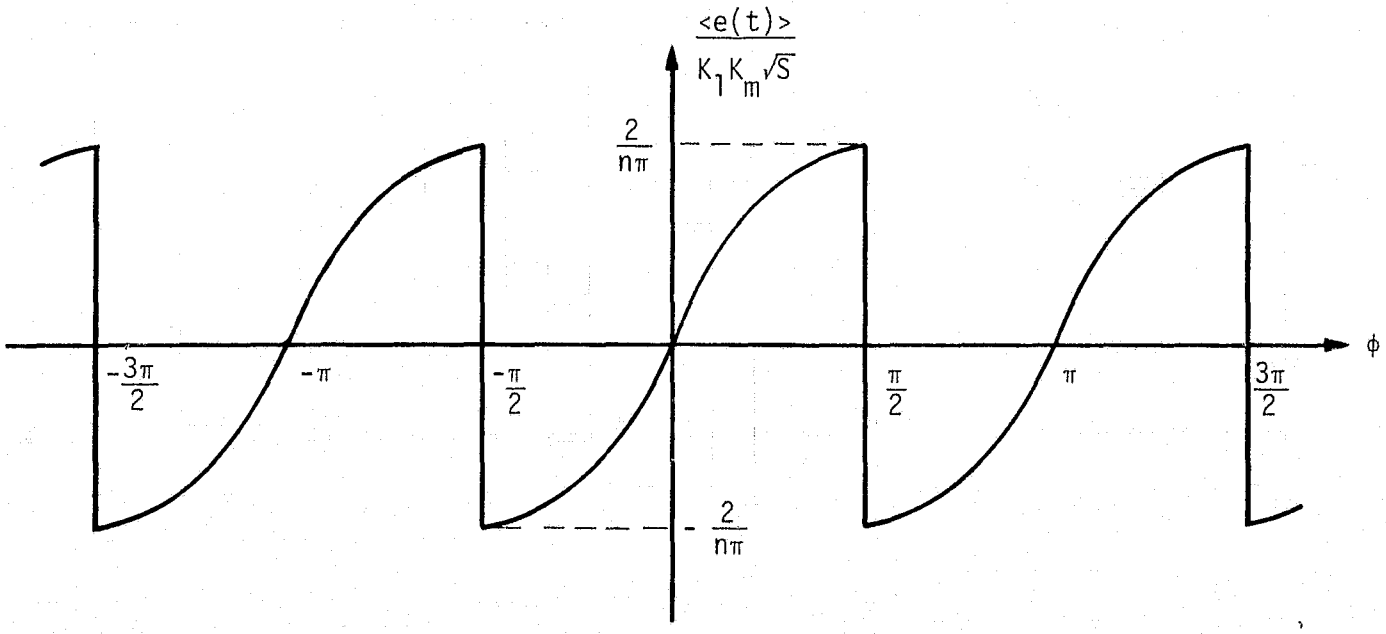


Figure 12b. True Lock S-Curve

To compare this behavior with that corresponding to true lock ($\Delta_f = 0$), we recall [17] that for true lock (see Figure 12b)

$$\frac{\langle e(t)\rangle}{K_1 K_m \sqrt{S}} = \sin\phi \ \mathrm{sgn}\,[\cos\phi] \tag{132}$$

Thus, we observe from (131) and (132) that the false lock S-curve is merely a 90° phase shift of the true lock S-curve and its slope at the lock point ($\pm n\pi/2$, n an odd integer) is $2/n\pi$ times that of the true lock S-curve at its lock point ($\pm n\pi$, n an even integer including zero).

4.1.2 $\gamma = \frac{p}{q}$ (p and q relatively prime)

When $\gamma = p/q$ with p and q relatively prime integers, the set {m} [see (127)] such that $mp/q = j_m$, $j_m$ any integer, clearly consists of the integers $m = \ell q$; $\ell = 1, 2, \ldots$ Thus, for this case, (127) simplifies to

$$\frac{\langle e(t)\rangle}{K_1 K_m \sqrt{S}} = \left| \frac{\sin\left(\frac{p\pi}{2q}\right)}{\frac{p\pi}{2q}} \right| \frac{4}{\pi} \sum_{\ell=1}^{\infty} (-1)^{\ell q - 1} (-1)^{\ell p} \left( \frac{2\ell q}{4\ell^2 q^2 - 1} \right) \sin(2\ell q \phi) \tag{133}$$

Some specific cases of (133) are now worthy of examination.

Case 1. q even, p arbitrary

If q is even and p and q are to be relatively prime, p must be odd. Thus,

$$(-1)^{\ell q - 1} = -1$$
$$(-1)^{\ell p} = (-1)^{\ell} \tag{134}$$

and (133) further simplifies to

$$\frac{\langle e(t)\rangle}{K_1 K_m \sqrt{S}} = \left| \frac{\sin\left(\frac{p\pi}{2q}\right)}{\frac{p\pi}{2q}} \right| \frac{4}{\pi} \sum_{\ell=1}^{\infty} (-1)^{\ell - 1} \left( \frac{2\ell q}{4\ell^2 q^2 - 1} \right) \sin(2\ell q \phi) \tag{135}$$

To put (135) in closed form, we examine the periodic function (Figure 12)

$$f(\phi) = \sin\left(\phi - \frac{m\pi}{q}\right); \qquad \left(m - \frac{1}{2}\right)\frac{\pi}{q} \le \phi \le \left(m + \frac{1}{2}\right)\frac{\pi}{q}$$
$$m = 0, \pm 1, \pm 2, \ldots. \tag{136}$$

Since the period of $f(\phi)$ in (136) is $\pi/q$, it has the Fourier series

$$f(\phi) = \sum_{\ell=-\infty}^{\infty} c_\ell \exp\left[j(2\ell q\phi)\right] \tag{137}$$

where the Fourier coefficients $c_\ell$ are given by

$$c_\ell = \frac{q}{\pi} \int_{-\frac{\pi}{2q}}^{\frac{\pi}{2q}} f(\phi) \exp[-j(2\ell q\phi)]\, d\phi \tag{138}$$

Substituting $\sin\phi$ for $f(\phi)$ in (138) and carrying out the integral evaluation yields

$$\begin{aligned} c_\ell &= \frac{q}{j\pi}(-1)^{\ell-1} \sin\left(\frac{\pi}{2q}\right)\left[\frac{4\ell q}{4\ell^2 q^2 - 1}\right] \\ c_{-\ell} &= c_\ell^* \\ c_0 &= 0 \end{aligned} \tag{139}$$

where the asterisk denotes complex conjugate. Substituting (139) into (137) and combining complex conjugate terms gives

$$f(\phi) = 2\left(\frac{\sin\left(\frac{\pi}{2q}\right)}{\frac{\pi}{2q}}\right) \sum_{\ell=1}^{\infty} (-1)^{\ell-1} \left(\frac{2\ell q}{4\ell^2 q^2 - 1}\right) \sin(2\ell q\phi) \tag{140}$$

Comparing (135) with (140) gives the desired result:

$$\frac{\langle e(t)\rangle}{K_1 K_m \sqrt{S}} = \left(\frac{2}{p\pi}\right) \frac{\left|\sin\left(\frac{p\pi}{2q}\right)\right|}{\sin\left(\frac{\pi}{2q}\right)} f(\phi) \tag{141}$$

where $f(\phi)$ is the normalized S-curve defined in (136) with <u>unit</u> slope at the lock points $\phi = 0, \pm\pi/q, \pm 2\pi/q, \ldots$ Note that, while the slope of the unnormalized S-curve of (141) depends on <u>both</u> p and q, the shape and period of it depend <u>only on q</u> as per (136). Further note that, if $p = 1$, in which case the false lock frequencies occur at $\Delta_f = 1/2qT$, the slope of the S-curve from (141) is $2/\pi$ times that of the true lock S-curve at its lock point, <u>independent of the value of q</u>. Thus, insofar as false lock <u>signal strength</u> is concerned, all of these lock points are equally strong.

However, since the period of the S-curve decreases as 1/q with increasing q, the tracking region ($-\pi/2q \leq \phi \leq \pi/2q$) becomes smaller and smaller as the false lock frequency comes closer and closer to the nominal carrier frequency $\omega_0$. Therefore, while indeed a stable false lock point theoretically exists (in the absence of noise) at any value of q regardless of how large, any small amount of phase noise associated with either the transmitter oscillator or receiver VCO will cause the loop to cycle slip, thereby preventing, in practice, false lock from occurring too close to the true lock frequency. A quantitative evaluation of the false lock points to external perturbations (e.g., additive noise, phase noise, oscillator instabilities, etc.), and the manner in which the loop acquires lock in the neighborhood of these points, can only be had by a careful study of the phase plane trajectories associated with the loop. Such a study is not the subject of the present report but is indeed important in order to obtain a complete picture of the false lock behavior of decision-directed I-Q loops. Without such additional analysis, our discussion must be somewhat qualitative and restricted to only tracking behavior once the loop has indeed false locked. Nevertheless, as we have already observed, a great deal of insight can still be gained from the limited results presented here.

Case 2. q odd, p arbitrary

If q is odd and p and q are to be relatively prime, p can be either even or odd. When p is even, the following simplifications of (133) occur:

$$(-1)^{\ell q-1} = (-1)^{\ell-1}$$
$$(-1)^{\ell p} = 1 \tag{142}$$

Using (142) in (133) results in an expression identical to (135). Thus, for p even, the false lock behavior is characterized by (141).

When p is odd, we have

$$(-1)^{\ell q-1} = (-1)^{\ell-1}$$
$$(-1)^{\ell p} = (-1)^{\ell} \tag{143}$$

and (133) becomes

$$\frac{<e(t)>}{K_1 K_m \sqrt{S}} = -\frac{\left|\sin\left(\frac{p\pi}{2q}\right)\right|}{\frac{p\pi}{2q}} \frac{4}{\pi} \sum_{\ell=1}^{\infty} \left(\frac{2\ell q}{4\ell^2 q^2 - 1}\right) \sin(2\ell q\phi) \tag{144}$$

Letting $\phi = \Phi + \frac{\pi}{2q}$ and recognizing that

$$\sin(2\ell q\phi) = \sin(2\ell q\Phi)\cos\pi\ell + \cos(2\ell q\Phi)\sin\pi\ell$$

$$= (-1)^{\ell} \sin(2\ell q\Phi) \tag{145}$$

we can rewrite (144) as

$$\frac{<e(t)>}{K_1 K_m \sqrt{S}} = \frac{\left|\sin\left(\frac{p\pi}{2q}\right)\right|}{\frac{p\pi}{2q}} \frac{4}{\pi} \sum_{\ell=1}^{\infty} (-1)^{\ell-1} \left(\frac{2\ell q}{4\ell^2 q^2 - 1}\right) \sin(2\ell q\Phi) \tag{146}$$

Comparing (146) with (135), we can immediately conclude that, for p odd,

$$\frac{<e(t)>}{K_1 K_m \sqrt{S}} = \left(\frac{2}{p\pi}\right) \frac{\left|\sin\left(\frac{p\pi}{2q}\right)\right|}{\sin\left(\frac{\pi}{2q}\right)} f\left(\phi - \frac{\pi}{2q}\right) \tag{147}$$

which has stable lock points at $\phi = \pm\frac{\pi}{2q}, \pm\frac{3\pi}{2q}, \pm\frac{5\pi}{2q}, \ldots$ Furthermore, note that the slopes of the false lock S-curves at their lock points are the same for q odd as for q even.

## 4.2 An Alternate Form for the Normalized S-Curve $f(\phi)$

An alternate form of the normalized S-curve $f(\phi)$ defined in (136) will now be derived. The purpose of this exercise is to show the relation of false lock tracking in decision-directed I-Q loops for biphase modulation [see (105)] with true lock tracking in decision-directed I-Q loops for polyphase modulation or, equivalently, M-ary PSK [27].

Once again, we must first separate our considerations into q even and q odd.

### 4.2.1 q even

Consider the function

$$g(\phi) = \frac{1}{q} \sum_{i=0}^{q-1} \sin\left[\phi + (2i+1)\frac{\pi}{2q}\right] \operatorname{sgn}\left\{\cos\left[\phi + (2i+1)\frac{\pi}{2q}\right]\right\} \tag{148}$$

which is periodic with period $\pi/q$. For $|\phi| \leq \pi/2q$, we would have sgn $\{\} = 1$ for the first $q/2$ terms and sgn $\{\} = -1$ for the remaining $q/2$ terms; thus,

$$g(\phi) = \frac{1}{q}\left\{\sum_{i=0}^{\frac{q}{2}-1} \sin\left[\phi + (2i+1)\frac{\pi}{2q}\right] - \sum_{i=\frac{q}{2}}^{q-1} \sin\left[\phi + (2i+1)\frac{\pi}{2q}\right]\right\} \tag{149}$$

Letting $\ell = q-1-i$ in the second summation and recognizing that

$$\begin{aligned}\sin\left[\phi + (2i+1)\frac{\pi}{2q}\right] &= \sin\left[\phi + (2q-2\ell-1)\frac{\pi}{2q}\right] \\ &= \sin\left[\phi + \pi - (2\ell+1)\frac{\pi}{2q}\right]\end{aligned} \tag{150}$$

we obtain after combining the two summations

$$g(\phi) = \frac{1}{q}\left\{\sum_{i=0}^{\frac{q}{2}-1}\left[\sin\left[\phi + (2i+1)\frac{\pi}{2q}\right] - \sin\left[\phi + \pi - (2i+1)\frac{\pi}{2q}\right]\right]\right\} \tag{151}$$

Trigonometrically expanding the sine functions in (151) gives

$$\begin{aligned} g(\phi) &= \frac{1}{q}\left\{\sum_{i=0}^{\frac{q}{2}-1}\left[\cos\left((2i+1)\frac{\pi}{2q}\right) - \cos\left(\pi - (2i+1)\frac{\pi}{2q}\right)\right]\sin\phi\right. \\ &\qquad \left. + \sum_{i=0}^{\frac{q}{2}-1}\left[\sin\left((2i+1)\frac{\pi}{2q}\right) - \sin\left(\pi - (2i+1)\frac{\pi}{2q}\right)\right]\cos\phi\right\} \\ &= \frac{2}{q}\left[\sum_{i=0}^{\frac{q}{2}-1}\cos\left((2i+1)\frac{\pi}{2q}\right)\right]\sin\phi \\ &= \frac{1}{q\sin\left(\frac{\pi}{2q}\right)}\sin\phi \end{aligned} \tag{152}$$

Comparing $g(\phi)$ of (152) with $f(\phi)$ of (136) (for $m = 0$), and the fact that both $g(\phi)$ and $f(\phi)$ are periodic with period $\pi/q$, we immediately see that for all $\phi$,

$$f(\phi) = q \sin\left(\frac{\pi}{2q}\right) g(\phi)$$

$$= \left[\sin\left(\frac{\pi}{2q}\right)\right] \sum_{i=0}^{q-1} \sin\left[\phi + (2i+1)\frac{\pi}{2q}\right] \operatorname{sgn}\left\{\cos\left[\phi + (2i+1)\frac{\pi}{2q}\right]\right\} \tag{153}$$

4.2.2 q odd

For q odd, we consider the function

$$g(\phi) = \frac{1}{q} \sum_{i=0}^{q-1} \sin\left(\phi + \frac{i\pi}{q}\right) \operatorname{sgn}\left\{\cos\left(\phi + \frac{i\pi}{q}\right)\right\} \tag{154}$$

which is also periodic with period $\pi/q$. Following steps similar to those in deriving (152) and (148), we obtain a result identical to (152); thus, once again, for all $\phi$ and q odd,

$$f(\phi) = q \sin\left(\frac{\pi}{2q}\right) g(\phi)$$

$$= \left[\sin\left(\frac{\pi}{2q}\right)\right] \sum_{i=0}^{q-1} \sin\left(\phi + \frac{i\pi}{q}\right) \operatorname{sgn}\left\{\cos\left(\phi + \frac{i\pi}{q}\right)\right\} \tag{155}$$

Careful examination of Figure 5 of [27] (the large signal-to-noise ratio approximation of the MAP estimation receiver for M-ary PSK) reveals an S-curve of the form (153) or (155) where the number of phases M is equal to $2^q$.

## 4.3 Sampled Data Loop Model

Consider the sampled data type of decision-directed I-Q loop proposed by Motorola as illustrated in Figure 13. Here, as contrasted with the continuous loop of Figure 11, the phase detector outputs are sampled at a rate $R_s = 1/T_s$, and input to accumulators (the sampled data equivalent of integrate-and-dump filters). Each accumulator sums a number of input samples corresponding to the number which occur in a symbol time. For simplicity, we shall assume that the ratio of sampling rate to symbol rate is integer, i.e.,

$$\frac{T}{T_s} = M \text{ ; } M \text{ integer} \tag{156}$$

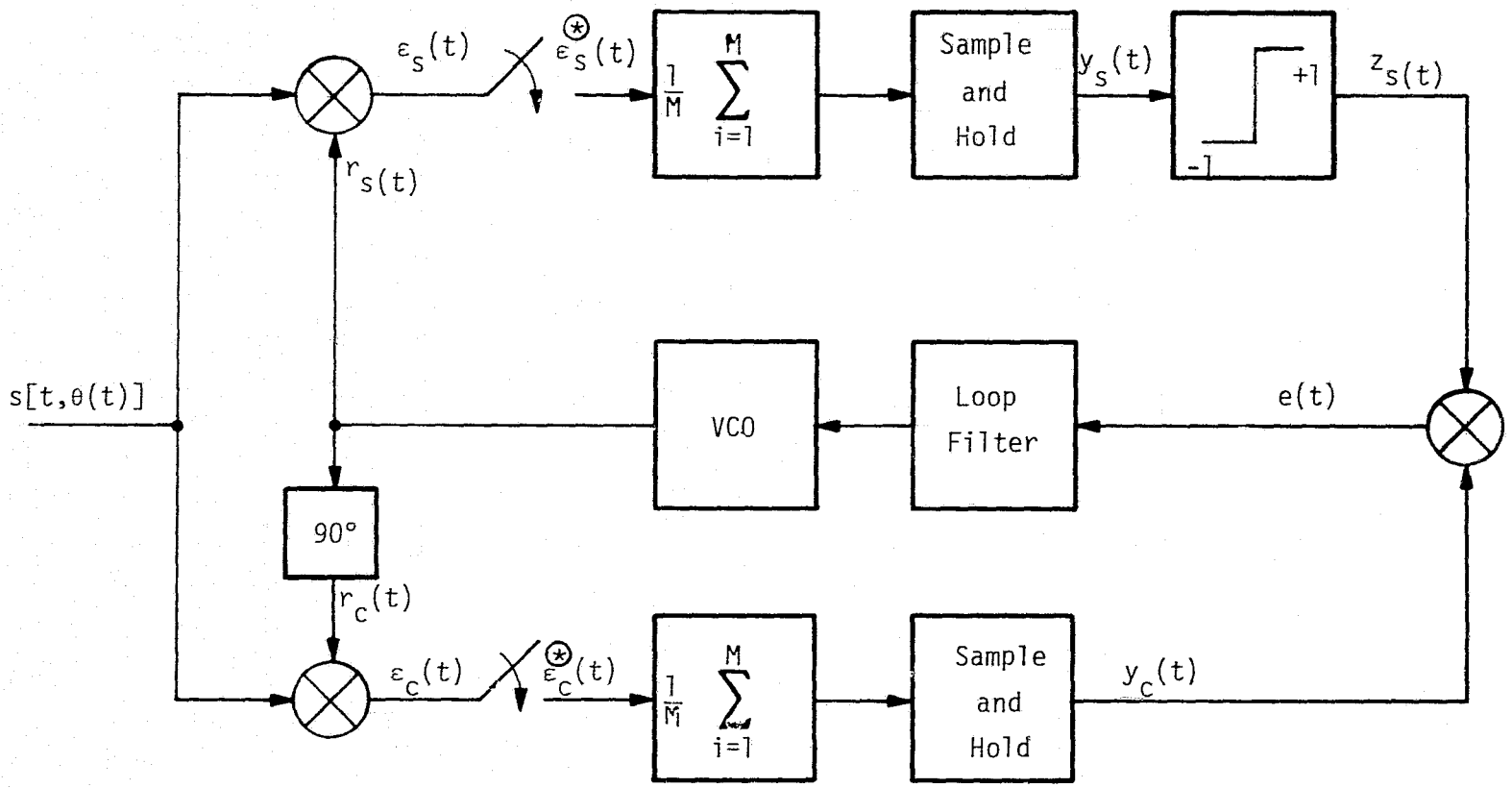


Figure 13. A Sampled Data Type Decision-Directed I-Q Loop

so that M also characterizes the size of the accumulators. The outputs of the in-phase and quadrature accumulators (which occur at the symbol rate) are sampled and held with the remainder of the loop operating as previously discussed for Figure 11.

Starting with the phase detector outputs of (108) and (109) and the characterization of the digital modulations given in (110), we can express the sampled versions of these signals by

$$\varepsilon_c^{\circledast}(t) \triangleq \varepsilon_c(t) \sum_{n=-\infty}^{\infty} \delta(t-nT_s)$$

$$= K_1 K_m \sqrt{S} \sum_{k=-\infty}^{\infty} a_{k-1} \sum_{i=(k-1)M+1}^{kM} \sin(\omega_f i T_s + \phi)\, \delta(t-iT_s)$$

$$\varepsilon_s^{\circledast}(t) \triangleq \varepsilon_s(t) \sum_{k=-\infty}^{\infty} \delta(t-nT_s)$$

$$= K_1 K_m \sqrt{S} \sum_{k=-\infty}^{\infty} a_{k-1} \sum_{i=(k-1)M+1}^{kM} \cos(\omega_f i T_s + \phi)\, \delta(t-iT_s) \qquad (157)$$

Thus, after in-phase and quadrature accumulation, the corresponding sample-and-hold outputs become, respectively,

$$y_s(t) = K_1 K_m \sqrt{S} \sum_{k=-\infty}^{\infty} a_{k-1}\, p(t-kT) \left[ \frac{1}{M} \sum_{i=(k-1)M+1}^{kM} \cos(\omega_f i T_s + \phi) \right]$$

$$y_c(t) = K_1 K_m \sqrt{S} \sum_{k=-\infty}^{\infty} a_{k-1}\, p(t-kT) \left[ \frac{1}{M} \sum_{i=(k-1)M+1}^{kM} \sin(\omega_f i T_s + \phi) \right] \qquad (158)$$

Passing $y_s(t)$ through the hard limiter and multiplying by $y_c(t)$ gives the loop error signal e(t), namely,

$$e(t) = y_c(t)\, z_s(t) = K_1 K_m \sqrt{S} \sum_{k=-\infty}^{\infty} B_k\, p(t-kT) \qquad (159)$$

where

$$B_k \triangleq \frac{1}{M} \left[ \sum_{i=(k-1)M+1}^{kM} \sin(\omega_f i T_s + \phi) \right] \operatorname{sgn} \left[ \sum_{i=(k-1)M+1}^{kM} \cos(\omega_f i T_s + \phi) \right] \qquad (160)$$

Letting $\ell = 1 - (k-1)M$, the sums in (160) are evaluated as follows:

$$\sum_{i=(k-1)M+1}^{kM} \sin(\omega_f iT_s+\phi) = \sum_{\ell=1}^{M} \sin\left[\omega_f \frac{T}{M}\left(\ell+(k-1)M\right) + \phi\right]$$

$$= \left[\sum_{\ell=1}^{M} \sin\left(\ell\omega_f \frac{T}{M}\right)\right] \cos\left(\phi+(k-1)\omega_f T\right)$$

$$+\left[\sum_{\ell=1}^{M} \cos\left(\ell\omega_f \frac{T}{M}\right)\right] \sin\left(\phi+(k-1)\omega_f T\right) \qquad (161)$$

Since

$$\sum_{\ell=1}^{M} \sin\left(\ell\omega_f \frac{T}{M}\right) = \frac{\sin\left[\left(\frac{M+1}{M}\right)\frac{\omega_f T}{2}\right]\sin\left(\frac{\omega_f T}{2}\right)}{\sin\left(\frac{\omega_f T}{2M}\right)}$$

$$\sum_{\ell=1}^{M} \cos\left(\ell\omega_f \frac{T}{M}\right) = \frac{\cos\left[\left(\frac{M+1}{M}\right)\frac{\omega_f T}{2}\right]\sin\left(\frac{\omega_f T}{2}\right)}{\sin\left(\frac{\omega_f T}{2M}\right)} \qquad (162)$$

then, substituting (162) into (161) and combining gives

$$\sum_{i=(k-1)M+1}^{kM} \sin(\omega_f iT_s+\phi) = \frac{\sin\left(\frac{\omega_f T}{2}\right)}{\sin\left(\frac{\omega_f T}{2M}\right)} \sin\left[\left(\frac{M+1}{M}\right)\frac{\omega_f T}{2} + \phi + (k-1)\omega_f T\right] \qquad (163)$$

Similarly, it can be shown that

$$\sum_{i=(k-1)M+1}^{kM} \cos(\omega_f iT_s+\phi) = \frac{\sin\left(\frac{\omega_f T}{2}\right)}{\sin\left(\frac{\omega_f T}{2M}\right)} \cos\left[\left(\frac{M+1}{M}\right)\frac{\omega_f T}{2} + \phi + (k-1)\omega_f T\right] \qquad (164)$$

Thus, substituting (163) and (164) into (160) gives the desired result

$$B_k = \frac{1}{M}\left|\frac{\sin\left(\frac{\omega_f T}{2}\right)}{\sin\left(\frac{\omega_f T}{2M}\right)}\right| \sin\left[\left(\frac{M+1}{M}\right)\frac{\omega_f T}{2} + \phi + (k-1)\omega_f T\right]$$

$$\times \operatorname{sgn}\left\{\cos\left[\left(\frac{M+1}{M}\right)\frac{\omega_f T}{2} + \phi + (k-1)\omega_f T\right]\right\} \tag{165}$$

Once again, to demonstrate the false lock behavior of the loop, we must demonstrate that there exists a frequency $\omega_f$ at which the time average of the loop error signal produces an S-curve about some steady-state phase error value. Thus, equivalently, we must examine the conditions under which

$$\frac{\langle e(t)\rangle}{K_1 K_m \sqrt{S}} = \frac{1}{M}\left|\frac{\sin\left(\frac{\omega_f T}{2}\right)}{\sin\left(\frac{\omega_f T}{2M}\right)}\right| \lim_{n\to\infty}\left(\frac{1}{2n+1}\right)\sum_{k=-n}^{n} \sin\left[\left(k-1+\frac{M+1}{2M}\right)\omega_f T + \phi\right]$$

$$\times \operatorname{sgn}\left\{\cos\left[\left(k-1+\frac{M+1}{2M}\right)\omega_f T + \phi\right]\right\} \tag{166}$$

is nonzero except at the lock point $\phi = \phi_0$. Letting $\theta = (k-1+(M+1)/2M]\omega_f T + \phi$ in the Fourier series for $\sin\theta \operatorname{sgn}[\cos\theta]$ (see (122)), then (166) becomes

$$\frac{\langle e(t)\rangle}{K_1 K_m \sqrt{S}} = \frac{1}{M}\left|\frac{\sin\left(\frac{\omega_f T}{2}\right)}{\sin\left(\frac{\omega_f T}{2M}\right)}\right| \frac{4}{\pi}\sum_{m=1}^{\infty}(-1)^{m-1}\left(\frac{2m}{4m^2-1}\right)$$

$$\times\left\{\left[\lim_{n\to\infty}\left(\frac{1}{2n+1}\right)\sum_{k=-n}^{n}\sin\left[(2k-1)m\omega_f T\right]\right]\cos\left[2m\phi + \frac{m\omega_f T}{M}\right]\right.$$

$$\left. + \left[\lim_{n\to\infty}\left(\frac{1}{2n+1}\right)\sum_{k=-n}^{n}\cos\left[(2k-1)m\omega_f T\right]\right]\sin\left[2m\phi + \frac{m\omega_f T}{M}\right]\right\} \tag{167}$$

Since the two limiting sums in (167) are identical with those in (123), then using their evaluation in (124), the conditions for false lock for the sampled-data loop are identical with those for the continuous loop

[see (125) or (126)]. Thus, analogous to (127), the false lock voltage (normalized to the loop gain) is given by

$$\frac{\langle e(t)\rangle}{K_1 K_m \sqrt{S}} = \frac{1}{M}\left|\frac{\sin\left(\frac{\gamma\pi}{2}\right)}{\sin\left(\frac{\gamma\pi}{2M}\right)}\right| \frac{4}{\pi} \sum_{\{m\}} (-1)^{m-1}(-1)^{m\gamma}\left(\frac{2m}{4m^2-1}\right) \sin\left[2m\left(\phi + \frac{\gamma\pi}{2M}\right)\right] \tag{168}$$

where again $\{m\}$ is the set of integer values of $m$ such that $m\gamma = j_m$, $j_m$ any integer (different for each $m$).

Comparing (168) with (127), we observe that the two results are quite similar except for two basic differences. First, the lock points of the S-curves for the sampled data loop are shifted by $\gamma\pi/2M$ relative to those of the continuous type loop. More important, however, is that the slope of the sampled data loop S-curves is degraded by

$$\eta \triangleq \left|\frac{M\sin\left(\frac{\gamma\pi}{2M}\right)}{\frac{\gamma\pi}{2}}\right| < 1 \tag{169}$$

relative to that of the continuous loop. Note that, as the ratio of sampling rate to data rate becomes large, then $\eta = 1$ and the two loops perform equivalently. Thus, $\eta$ represents the degradation in false and true lock tracking performance due to the finite sampling rate.

Without going into great detail, suffice it to say that the specific results previously obtained for the continuous loop by considering $\gamma$ integer and $\gamma = p/q$ with $p$ and $q$ relatively prime can be applied to the sampled data loop as follows. The slope of every S-curve previously obtained must now be multiplied by $\eta$, and $\phi$ must be replaced by $\phi + \gamma\pi/2M$.

## 4.4 Periodicity of False Lock Behavior

One final difference between the false lock behavior of the continuous and sampled-data decision-directed I-Q loops is the periodicity of the false lock behavior caused by the sampling operation in the latter. To see this, consider (168) with $\gamma$ replaced by $\gamma + 2M$, namely,

$$\frac{\langle e(t)\rangle}{K_1 K_m \sqrt{S}} = \frac{1}{M}\left|\frac{(-1)^M \sin\left(\frac{\gamma\pi}{2}\right)}{-\sin\left(\frac{\gamma\pi}{2M}\right)}\right| \frac{4}{\pi} \sum_{\{m\}} (-1)^{m-1}(-1)^{m\gamma}(-1)^{2Mm}$$

$$\times \left(\frac{2m}{4m^2-1}\right) \sin\left[2m\left(\phi + \frac{\gamma\pi}{2M}\right) + 2m\pi\right]$$

$$= \frac{1}{M}\left|\frac{\sin\left(\frac{\gamma\pi}{2}\right)}{\sin\left(\frac{\gamma\pi}{2M}\right)}\right| \frac{4}{\pi} \sum_{\{m\}} (-1)^{m-1}(-1)^{m\gamma}\left(\frac{2m}{4m^2-1}\right) \sin\left[2m\left(\phi + \frac{\gamma\pi}{2M}\right)\right] \qquad (170)$$

which is identical to (168). Thus, the false lock behavior of the sampled-data loop is periodic with period 2M. Similarly, the true lock behavior of this loop is also periodic with period 2M.

## 4.5 Comparison with Previous Experimental Results

Experiments on a second-order sampled data hardware version of a suppressed carrier data-aided loop have been previously conducted [26]. Since, as previously mentioned in the introduction, the loop was actually implemented as a sampled-data decision-directed I-Q loop similar to the proposed Motorola loop, it is logical to compare the theoretical false lock results obtained here with the comparable experimental results reported in [26]. In particular, false lock acquisition tests were conducted by offsetting the loop VCO from the nominal transmitted frequency by a certain amount when the loop was open*, then closing the loop and observing the transition to the steady-state condition. These tests were conducted in the absence of noise.

The results of these experiments are illustrated in Figure 14 (same as Figure 3-14 of [26]). False lock points are indicated by the solid vertical lines topped by numbers. The vertical dashed lines represent instability region boundaries. Some instability boundaries are coincident with the false lock points. The arrows indicate the direction taken by the loop VCO once the loop is closed, assuming that the initial open-loop frequency offset falls somewhere between the relevant instability boundaries. To illustrate this, for all initial $|\Omega_0/2\pi W_L| < 0.19$ ($W_L$ is the two-sided closed-loop noise bandwidth), the proper lock point

*The condition of open loop involves removing any residual memory from the loop filter.

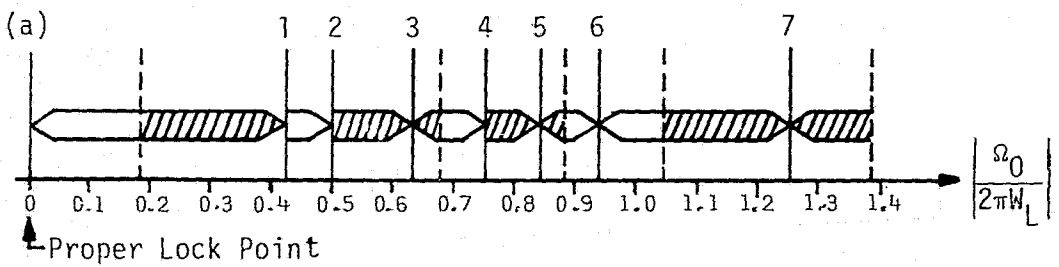


Figure 14. Data-Aided Loop False Lock Ranges for $\delta = 10$

is reached. For $0.19 < |\Omega_0/2\pi W_L| < 0.42$, the first false lock point becomes the steady-state condition. For $0.5 < |\Omega_0/2\pi W_L| < 0.68$, the loop will tend to false lock at point 3. The alternate regions of false lock are indicated by shaded arrows. The reason why some instability region boundaries are coincident with lock points is unknown. Notice the definite subregions where frequency pushing away from the proper lock point occurs. This would be indicated by any arrows that point to the right.

Since our theoretical results here apply only to false lock tracking and not false lock acquisition behavior, we can, at best, hope to verify the vertical solid lines observed in Figure 14. Since Figure 14 is plotted for $\delta = 10$ and $\delta$ is defined as the ratio of data rate to one-sided loop noise bandwidth, i.e.,

$$\delta = \frac{2}{W_L T} \tag{171}$$

then the horizontal axis can equivalently be relabeled $5\Delta_f T$ where we have also defined $\Delta_f = \Omega_0/2\pi$ in order to be consistent with our usage in this report. Thus, the observed false frequencies corresponding to vertical lines 1 through 7 occur, respectively, at $\Delta_f = 1/12T$, $1/10T$, $1/8T$, $3/20T$, $1/6T$, $3/16T$, and $1/4T$. Note that the vertical lines 1, 2, 3, 5, and 7 have false lock frequencies of the form $1/q(2T)$ where $q = 6$, 5, 4, 3, and 2. As previously discussed, false lock frequencies with the smallest values of q are likely to be the most stable from the standpoint of external noise disturbances. The two remaining false lock frequencies (vertical lines 4 and 6) correspond to $\Delta_f = p/q(2T)$ where $p = 3$ and $q = 10$ and 8, respectively. These are, again, the values of $\Delta_f$ where p and q are relatively prime with the smallest values of q for $p = 3$ (within the region of measured observation).

Because of the false lock susceptibility of the hard-limited loop proposed by Motorola, Axiomatix believes the implementation should be reviewed. At the moment it seems that, in the sampled data hardware version proposed by Motorola, there is little implementation impact for not hard-limiting the in-phase channel. Therefore, a better implementation would be to eliminate the hard limiter, which would leave the first false lock point at one-half the data rate (integrate-and-dump sample time), i.e., outside the acquisition sweep range.

# 5.0 S-BAND ANTENNA MEASUREMENT

## 5.1 Introduction and Statement of Problem

The actual gain pattern for the Orbiter S-band antennas is difficult, at best, to predict from the customary ground antenna range pattern measurements. This is because, for these flush-mounted antennas, the Orbiter structure itself has a profound influence on the pattern. Consequently, the adjacent sections of the Orbiter structure in which the antennas are mounted have been mocked-up and, along with the antenna(s) mounted in them, used for pattern tests on the JSC antenna range. This technique typically yields fairly accurate gain measurements near the boresight of the antenna, i.e., normal to the surface of the structure. However, as the angle of boresight increases, the accuracy in the gain pattern decreases due to edge effects of the limited structural mockup and the missing influence of the more remote parts of the structure, such as the wings.

Because of the predicted narrow margins for some of the S-band Shuttle/TDRSS links, it is desirable to determine the antenna gains with greater accuracy. This will enable a higher degree of confidence in the Shuttle/TDRSS links to be established. A prime opportunity to accomplish this finer calibration exists during the OFT phase because, during OFT, communication with the Shuttle will be via STDN stations. While in orbit, the actual performance of the Shuttle antennas will be free of all the ground effects present on conventional antenna ranges. Thus, with appropriate link calibration and data processing, the OFT Orbiter/STDN link can function in the same manner as an antenna range.

The remainder of this section describes a technical approach to be used during OFT to obtain the finer gain calibration. The results described are preliminary, and further refinement of the approach is continuing.

## 5.2 General Technical Approach

The RF link information which will be available during OFT for purposes of Shuttle antenna calibration will fall into two general categories. First, there is the link information which will be obtained during communication while the Orbiter is in a "random attitude." By

"random attitude," it is meant that the Orbiter attitude has not been picked specifically for antenna calibration purposes but, rather, is determined by other mission requirements such as thermal testing or payload operations. The other category of link information is that which is obtained while the Orbiter's attitude is determined and controlled specifically to support antenna calibration. The desired primary objective in this case is to utilize specific antenna coordinate profiles, or "cuts," to obtain gain information for that portion of the antenna(s) pattern. This would be implemented by having the Orbiter perform suitable roll and pitch maneuvers.

The type of link information gathered from the programmed attitude profile is superior to the "random attitude" category. This is because it is a more systematic approach and comes closest to conventional antenna pattern measurement techniques. It is felt, however, that the latter category of link information will be the predominantly available information due to the pressure of numerous mission requirements for OFT. Consequently, the preliminary approach taken here for developing an antenna calibration technique has been to develop a method for utilizing the "random attitude" category of data.

The general approach to calibrating the Orbiter S-band antennas during OFT with "random attitude" data is as follows:

(1) Calibrate the STDN station.

(2) Record received signal strength versus Orbiter attitude.

(3) Filter the data from (2) to fill in any holes (i.e., interpolate for missing data for segments of the pattern).

(4) Filter the data from (2) to take advantage of multiple measurements of the same segments of the pattern.

Figure 15 illustrates the basic mathematical link relationship for determination of antenna gain from received signal power. From this figure, it is seen that, in addition to Orbiter attitude, the key parameters which must be known or measured are: received signal power, calibrated STDN gain, Orbiter transmitted power, line-of-sight range, and carrier frequency. This calculation is not normally encountered in conventional antenna measurement procedures because, in conventional procedures, a standard gain horn is substituted for the antenna being measured and the received signal power is measured. Thereafter, the dB

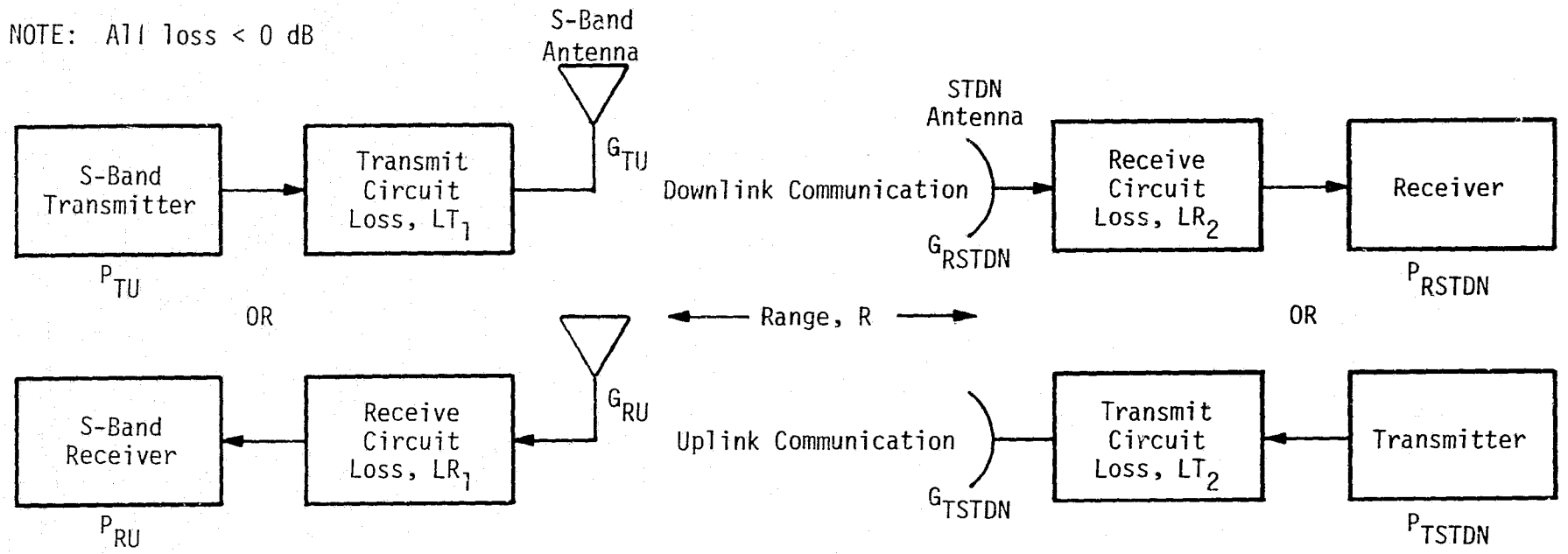


Downlink Communications Antenna Gain Determination

$$P_{RSTDN} = P_{TU} + LT_1 + G_{TU} + L_R + G_{RSTDN} + LR_2$$

$$G_{TU} = P_{RSTDN} - P_{TU} - LT_1 - L_R - G_{RSTDN} - LR_2$$

Uplink Communications Antenna Gain Determination

$$P_{RU} = P_{TSTDN} + LT_2 + G_{TSTDN} + L_R + G_{RU} + LR_1$$

$$G_{RU} = P_{RU} - P_{TSTDN} - LT_2 - G_{TSTDN} - L_R - LR_1$$

where

$G_{TU}$ = Shuttle transmit antenna gain
$G_{RU}$ = Shuttle receive antenna gain
$P_{TU}$ = Shuttle transmitter output power
$P_{RU}$ = Shuttle received power at receiver
$LT_1$ = Shuttle transmit circuit loss
$LR_1$ = Shuttle receive circuit loss

$G_{RSTDN}$ = STDN receive antenna gain
$G_{TSTDN}$ = STDN transmit antenna gain
$P_{RSTDN}$ = STDN receive power
$P_{TSTDN}$ = STDN transmitter power
$LR_2$ = STDN receive circuit loss
$LT_2$ = STDN transmit circuit loss

Figure 15. Link Relationships for Determination of Shuttle Antenna Gain During OFT

difference in received signal power with the measured antenna indicates the gain relative to the standard gain horn.

The calibrated STDN gain includes the entire receive (or transmit) chain including antenna gain, antenna feed circuit losses, preamp gain, and receiver gain. Since it may be desirable to measure received signal power on the Orbiter, the STDN gain and power in the transmit mode must also be known. Similarly, the Orbiter antenna circuit losses must be known in both the transmit and receive modes.

Since the STDN stations are not operated for metrology purposes, it is unlikely that sufficiently accurate gain calibration for the stations will exist. However, it should be possible to use the Orbiter itself to calibrate the STDN station. This could be accomplished by using the measured STDN received signal strength when an Orbiter S-band antenna is being used in an orientation that has a high degree of gain confidence, i.e., close to antenna boresight. Calibration techniques will be presented in detail in a subsequent report.

The basic information gathering and processing procedure to obtain the gain pattern is shown in Figure 16. Provisions for gain calculations from both uplink and downlink communications are shown. The majority of Figure 16 depicts the information flow necessary to evaluate the equations shown in Figure 15. The box labeled "Unprocessed Gain Matrix" represents the three-dimensional matrix of measured antenna gain samples. This matrix is depicted in Figure 17. The X and Y coordinates correspond to the quantized azimuth and elevation coordinates of the antenna. The Z coordinate corresponds to the measured gain samples. There may be several gain samples for a given coordinate, corresponding to several passes of the same station or samples of the gain at that coordinate for several stations. In general, the elements of the three-dimensional gain matrix are identified by $G_{N,\theta,\phi}$ where

$G_{N,\theta,\phi}$ = gain sample which is a function of station, station elevation angle, Orbiter attitude, and Orbiter transmit circuit

$N$ = number of gain samples for the particular $\theta,\phi$ cell

$\theta$ = Shuttle elevation angle

= $i\Delta\theta$, where $\Delta\theta$ is the desired elevation angular resolution

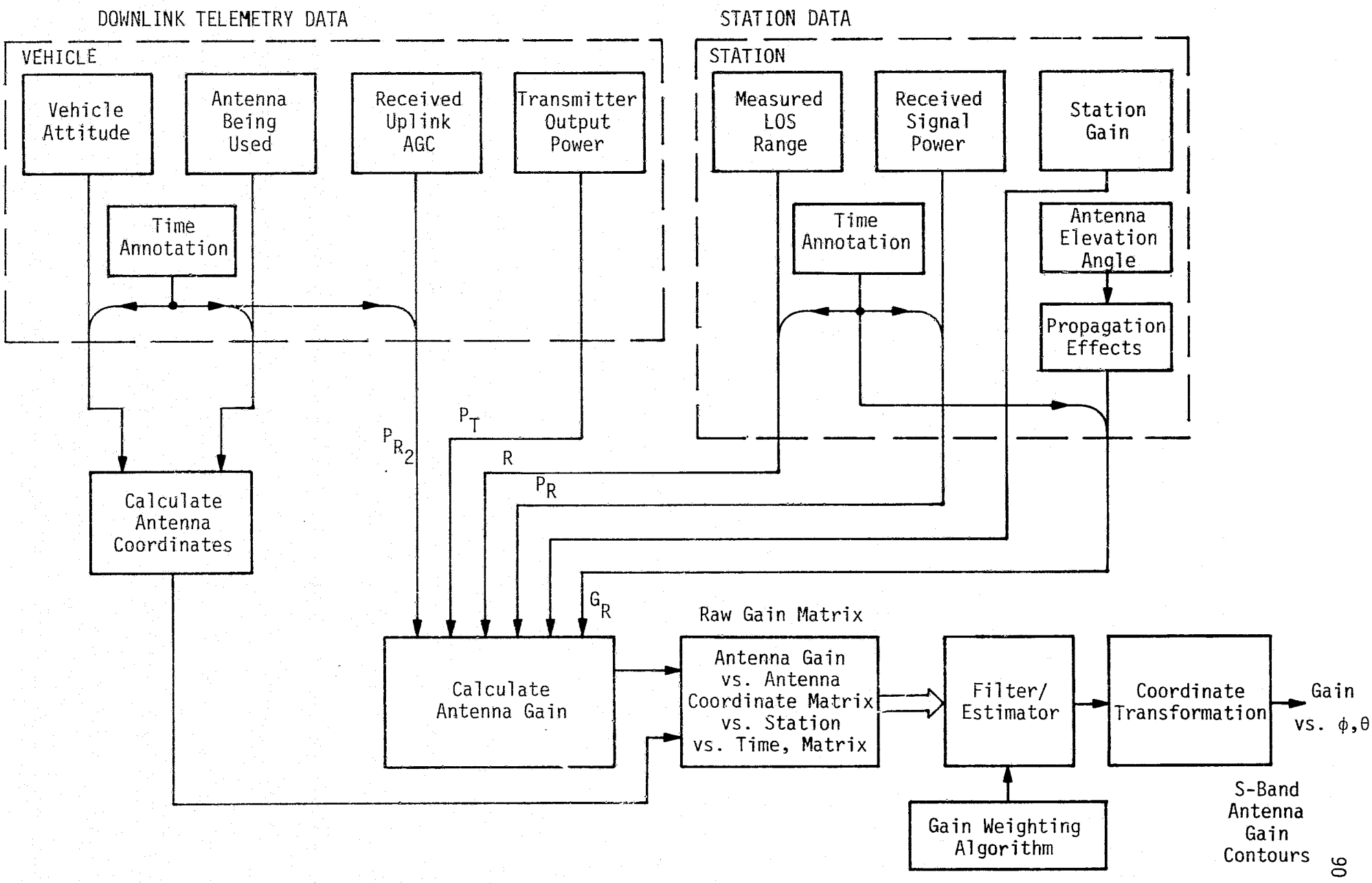


Figure 16. Information Flow for Gain Pattern Determination of Shuttle Antenna During OFT

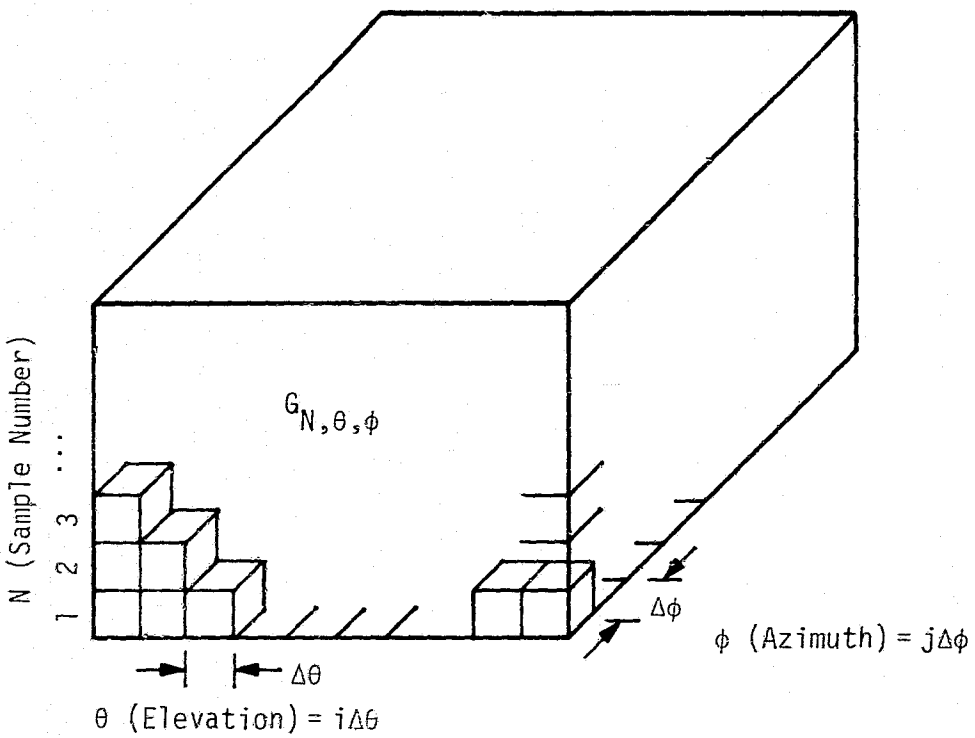


$G_{N,\theta,\phi}$ = f(station, station elevation angle, time, Orbiter attitude, Orbiter transmitter)

N = 0 to number of gain samples for the particular $\theta,\phi$ cell

$\theta = i\Delta\theta$, $\Delta\theta$ = required elevation angular resolution

$i = 0,\pm1,\pm2,\ldots,\pm I$ where $I\Delta\theta$ = antenna pattern interest limits

$\phi = j\Delta\phi$, $\Delta\phi$ = required azimuth angular resolution

$j = 0,\pm1,\pm2,\ldots,\pm J$ where $J\Delta\phi$ = antenna pattern interest limits

Figure 17. Unprocessed Gain Matrix

$i = 0, \pm1, \pm2, \ldots, \pm I$, where $I\Delta\theta$ is the region of interest for the antenna pattern for elevation

$\phi = j\Delta\phi$, where $\Delta\phi$ is the desired azimuth angular resolution

$j = 0, \pm1, \pm2, \ldots, \pm J$, where $J\Delta\phi$ is the region of interest for the antenna pattern for azimuth.

The matrix of $G_{N,\theta,\phi}$ will, in general, have many $\theta,\phi$ cells for which where will be no values and others for which there will be several values. Thus, to arrive at the final antenna pattern, it is necessary to pass this matrix through an appropriate filter/estimator. This process is discussed in the following section.

## 5.3 Antenna Data Processing Algorithm

The flow chart for the preliminary antenna data processing algorithm is shown in Figure 18. The first step in the process is to read the data tapes for both Shuttle data and STDN station data. At this point, it is assumed that all data is appropriately annotated and time tagged. Thus, it should be fairly straightforward to correlate Shuttle received signal power with Shuttle attitude. Whether this software exists, or must be modified, or must be developed will be evaluated as the follow-on study continues. Calculation of the raw gain is a straightforward process, as depicted in Figure 15. Once the raw gain samples are correlated with the corresponding coordinates, the raw gain matrix $G_{N,\phi,\theta}$ exists. The remainder of the algorithm, with the exception of the generation of the weighting factor, $W_n$, is devoted to the filtering and estimation processing of $G_{N,\phi,\theta}$. The filtering and estimation process is a complex problem involving linear interpolation and extrapolation of a random space-time field with a limited domain of measurement. An initial heuristic approach to the problem is depicted in Figure 18. However, the mathematical analysis of a more effective algorithm has been started and, when completed, will be used to update the process of Figure 18. The preliminary findings of this analysis are summarized in the following section.

The calculation of weighting factors is another process that is currently under development. Some of the factors considered in the weighting factor calculation include the distance the antenna coordinate is from the antenna boresight, the accuracy of STDN station calibration, the elevation angle of the STDN station, and several other link and hardware considerations.

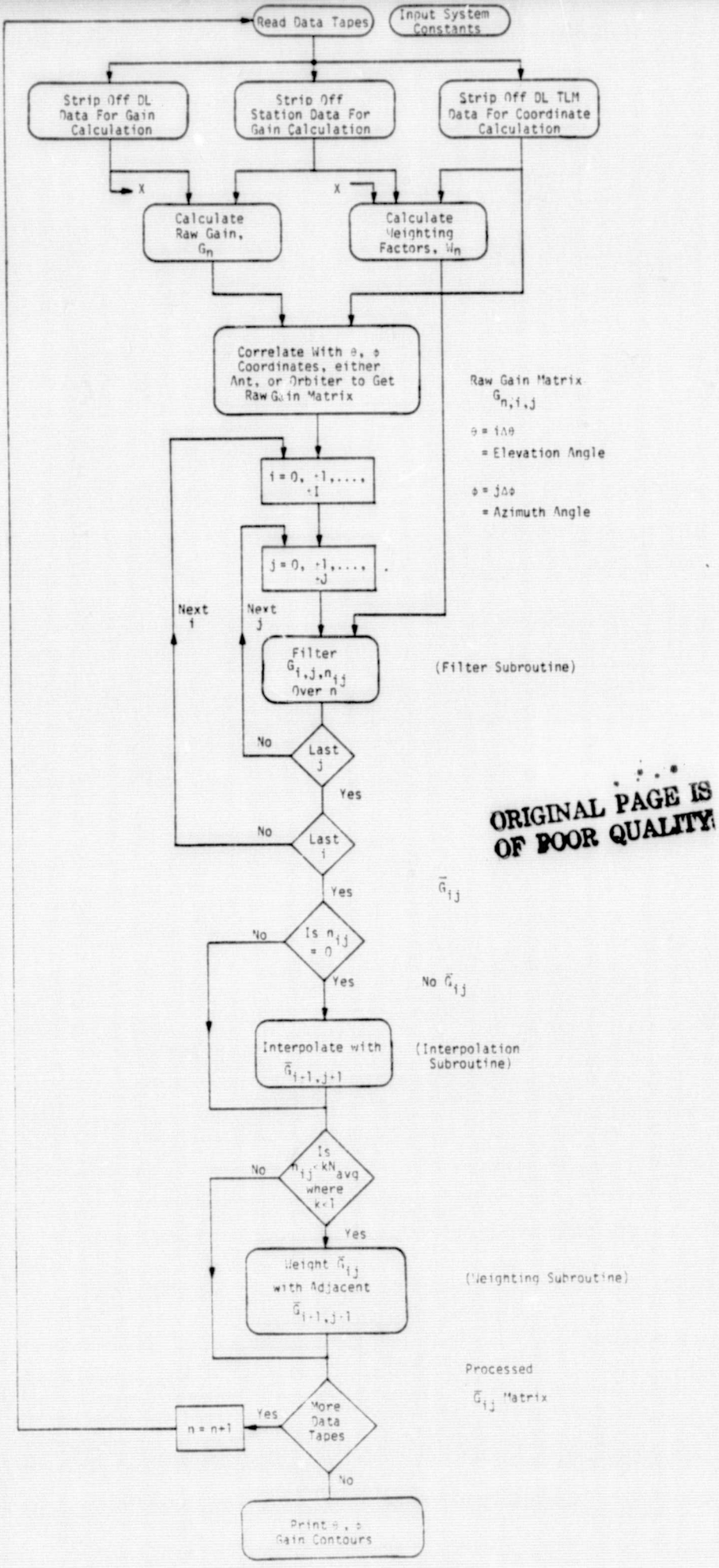




Figure 18. Flow Chart for Preliminary Antenna Data Processing Algorithm

After the weighting factors have been assigned to each sample of $G_{N,\theta,\phi}$, a weighted average is performed along the N dimension (Z axis of the matrix) for each $\theta,\phi$ coordinate. This results in

$$\bar{G}_{\theta,\phi} = \sum_{\substack{n=1 \\ \text{for all} \\ \theta,\phi}}^{N} G_{N,\theta,\phi} \; W(N,\theta,\phi) \qquad (172)$$

Since N will be 0 for some $\theta,\phi$ coordinates, it is necessary to use the nearest adjacent samples to these missing samples to interpolate the missing samples. This is shown in Figure 18. Where N is small for $\theta,\phi$ cells, it is desirable to weight the weighted average of (172) with the adjacent neighbors' weighted averages. This process, combined with the interpolation process, is actually filtering in the $\theta,\phi$ plane. Again, the final algorithm for this two-dimensional filtering process is subject to the results of the analysis currently being conducted.

As shown in Figure 18, as more data tapes become available, the process is reiterated. This provides a more accurate estimate of the gain pattern. This basic analytical approach for the filtering algorithms is described next.

## 5.4 Derivation of Antenna Gain Filtering Algorithm

An initial analytical exposé is presented which will provide a good estimate of the variations in the Shuttle antenna pattern due to the Orbiter's appendages and obtained from measurements taken from orbital passes. The analysis will need to be massaged to account for specific intricacies of the antenna problem, such as:

(1) Large known variations in signal strength from measurement to measurement due to

(a) position in pattern that is being measured,

(b) variations among the various ground receivers such as fixed biases, and

(c) ground station uncertainties.

(2) There exists a benchmark or baseline antenna pattern obtained from ground measurements. As a result, what we are actually determining are the changes in the pattern versus the vehicle attitude due to the presence of the Orbiter's appendages.

(3) There exists some calibration capability because the antenna pattern will not change in certain regions (for example, at boresight).

As a result, the output of this exercise is a set of variations from the present baseline patterns obtained from ground measurements.

The variations in antenna pattern and the resulting measurements can be satisfactorily modeled in terms of added biases and additive Gaussian noise. As a result, the problem at hand can be described as linear interpolation and extrapolation of a random space-time field with a limited domain of measurement.

### 5.4.1 Basic Approach

Let us consider the basic problem of linear estimation and interpolation in the absence of additive noise. A random variable $G(\underline{X})$ defined on a multidimensional argument $X = \{x_1, x_2, \ldots, x_N\}$ is to be measured at a set of points $\{X_k\}$, $k = 1, \ldots, n$, which is to be used to form a linear estimate $\hat{G}(\underline{X})$ by means of a linear combination of the sampled values with appropriate weighting factors:

$$\hat{G}(X) = \sum_{k=1}^{n} G(X_k)\, w(X, X_k) \tag{173}$$

For the antenna pattern, $N = 2$, and $X = (\theta_1, \theta_2)$ for the two angles necessary to specify positions on the pattern. In (173), $w(X, X_k)$ are the weighting factors to be determined; $G(X_k)$, $k = 1, \ldots, n$, are the antenna measurements; and $\hat{G}(X)$ is the estimated antenna pattern, and $\underline{X}$ can be any value for which the pattern is to be determined.

Our criterion for estimation is to minimize the mean-square error

$$\sigma_\varepsilon^2 = E\left\{\left[G(X) - \hat{G}(X)\right]^2\right\} \tag{174}$$

which can be expressed as

$$\sigma_\varepsilon^2 = E\left\{\left[G(X)\right]^2\right\} - 2\sum_{k=1}^{n} w(X, X_k)\, E\left[G(X)G(X_k)\right] + \sum_{\ell=1}^{n}\sum_{k=1}^{n} w(X, X_k)\, w(X, X_\ell)\, E\left[G(X_k)G(X_\ell)\right] \tag{175}$$

Introducing the notation

$$K(X,Y) \triangleq E\left[G(X)\ G(Y)\right] \tag{176}$$

for the cross-correlation function of the antenna pattern, which contains the known second-order statistics, the mean-square error can be written as

$$\sigma_\varepsilon^2 = K(X,X) - 2 \sum_{k=1}^{n} K(X,X_k)\ w(X,X_k) + \sum_{\ell=1}^{n} \sum_{k=1}^{n} (X_k,X_\ell)\ w(X,X_k)\ w(X,X_\ell) \tag{177}$$

By using standard techniques to determine the set of the weighting values $\{w(X,X_k)\}$ to yield the minimum value of mean-square error, necessary and sufficient conditions which must be satisfied are

$$K(X,X_r) = \sum_{k=1}^{n} K(X_r,X_k)\ w_o(X,X_k) \qquad r = 1, \ldots, n \tag{178}$$

where $\{w_o(x,y)\}$ are the optimum weights.

By substituting (178) into (177), an expression for the minimum mean-square error is

$$\sigma_{min}^2 = K(X,X) - \sum_{k=1}^{n} K(X,X_k)\ w_o(X,X_k) \tag{179}$$

When these optimum weights are determined from (178) and the theory is extended to take into account the specific issues enumerated at the outset, the most effective weight will result for updating the Shuttle antenna pattern.

## 6.0 S-BAND RFI MEASUREMENT

During the course of this contract, Axiomatix was asked to examine the possibility of evaluating the effects of RFI on TDRSS S-band communication during OFT. The scenario for the RFI and operational S-band Shuttle/TDRSS communication links is shown in Figure 19. Because TDRSS will not be available for OFT, the concept was to use the Shuttle S-band receiver as a test instrument to possibly detect the RFI. This test scenario is shown in Figure 20.

The first question asked was whether the Shuttle would be visible to both the RFI and the STDN during OFT. To answer this question, JSC ran the orbital trajectory software. Typical results are shown in Figures 21 and 22 for a 38°, 120-mile orbit. Figure 21 is the elevation angle at the East German RFI. It can be seen that the maximum elevation is less than 0.5 degree and that this limited visibility lasts for only 2 minutes. The only STDN station to potentially have simultaneous visibility is Madrid. Figure 22 shows the elevation angle at Madrid for this time period. Unfortunately, there are virtually only a few seconds before the Madrid station antenna is obstructed by the local terrain. For the BRM 2, or "Base Reference Mission" (55°, 300-mile orbit), however, the situation is somewhat different, as shown in Figures 23 and 24. Figure 23 is the Shuttle visibility (elevation angle) at Madrid and Figure 24 is the same for the East Germany RFI. It can be seen that there is good overlap, although for only several minutes. One possible method for increasing the overlap time is to utilize a portable "STDN" station. This station would be positioned at a location, preferably a U.S. base or facility within an allied country, which would be chosen to yield as much overlap time as possible. The location and design of the portable station will be studied as part of the follow-on contract.

The next step in the evaluation is to analyze the signal level of the RFI at the Shuttle during OFT and attempt to predict the effects of the Shuttle receiver. This work will be undertaken during the follow-on contract.

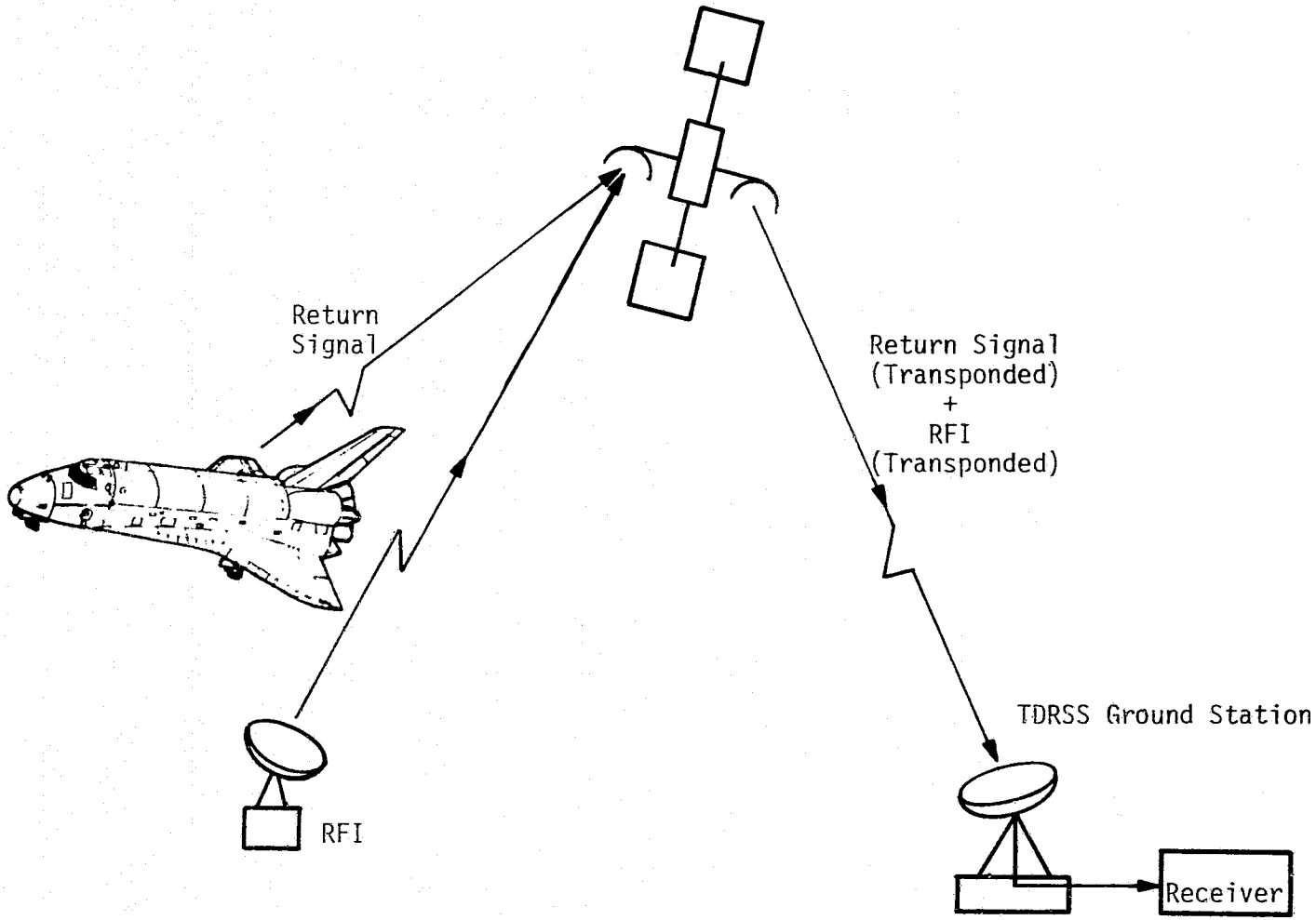


Figure 19. TDRSS/Shuttle/RFI Operational Scenario

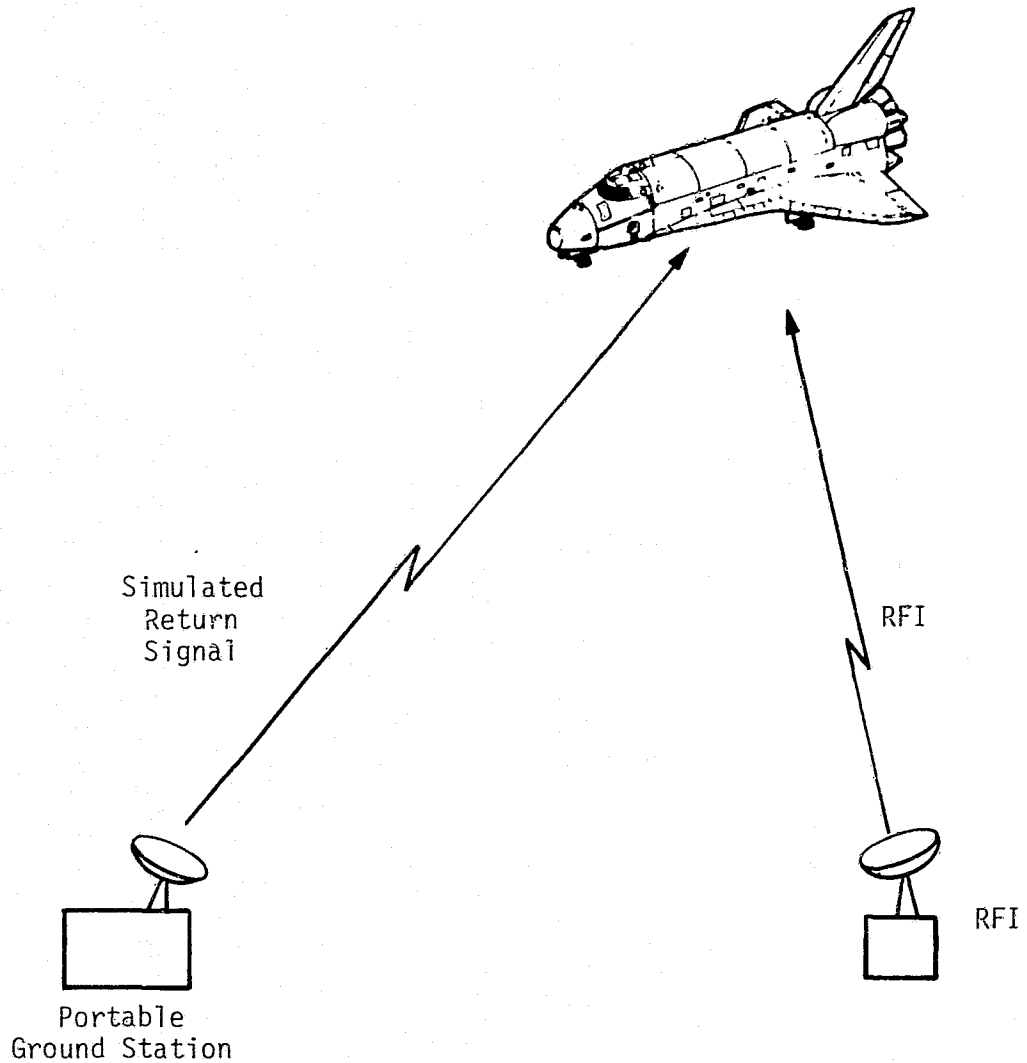


Figure 20. RFI Test Scenario

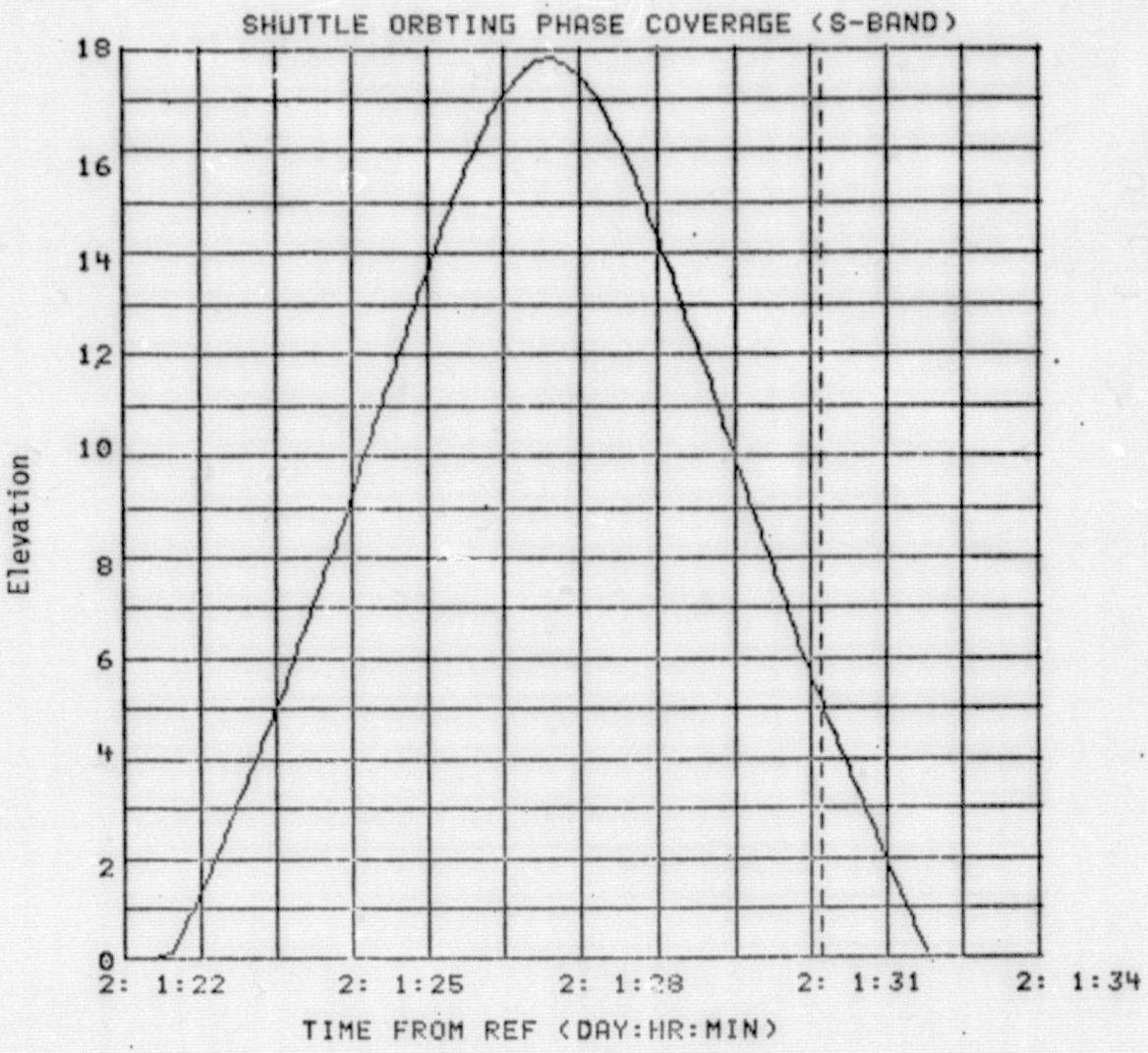


TRAJECTORY: BRM2 (NORTHERLY LAUNCH)
LAUNCH SITE: KSC; LANDING SITE: KSC
GROUND STATION: RFI1

Figure 21. Shuttle Visibility at East Germany RFI Location

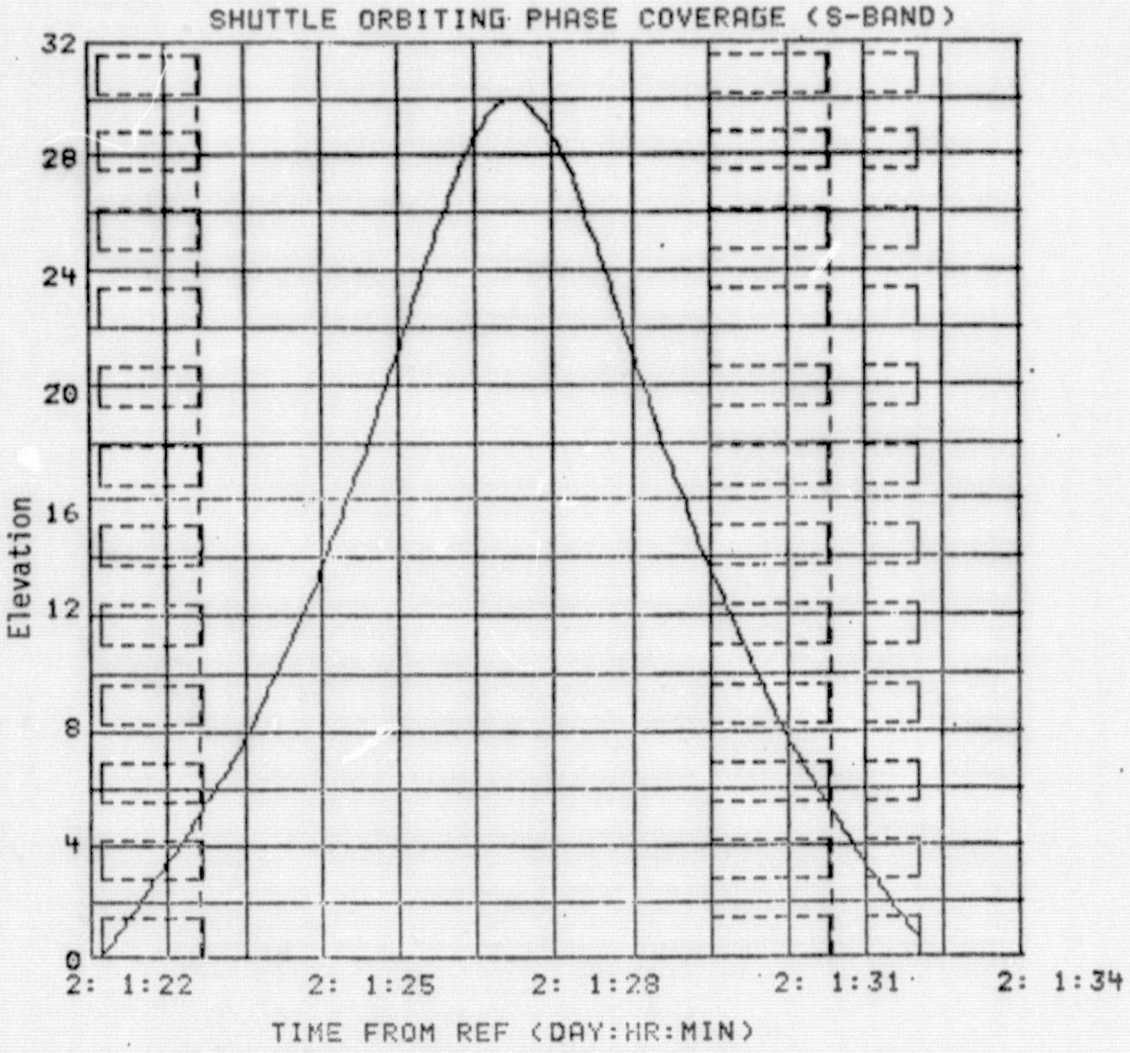


TRAJECTORY: BRM2 (NORTHERLY LAUNCH)
LAUNCH SITE: KSC; LANDING SITE: KSC
GROUND STATION: MAD

Figure 22. Shuttle Visibility at Madrid for Simultaneous RFI Visibility for BRM2

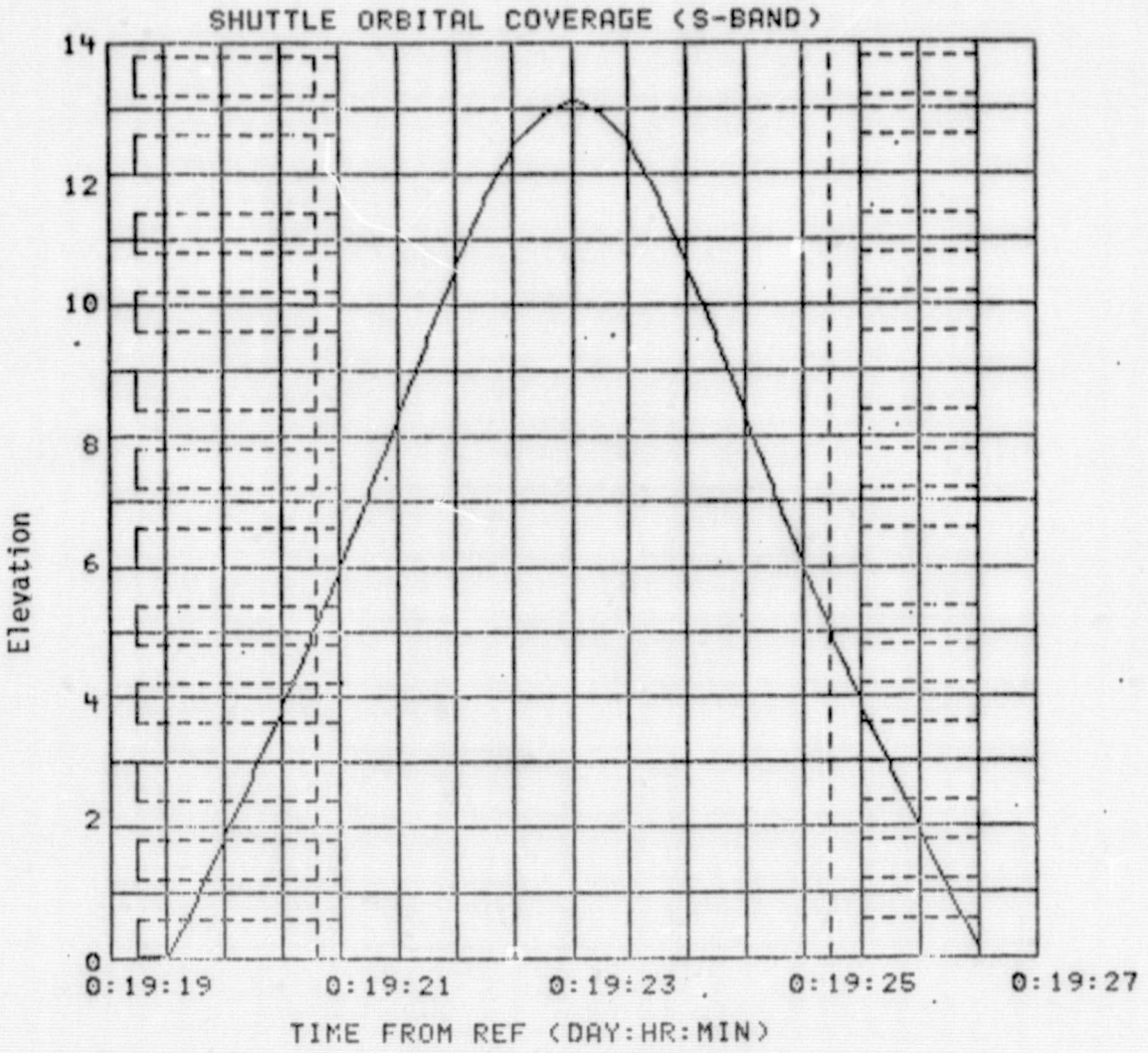


Figure 23. Madrid STDN Elevation Angle During Simultaneous Shuttle Visibility with RFI

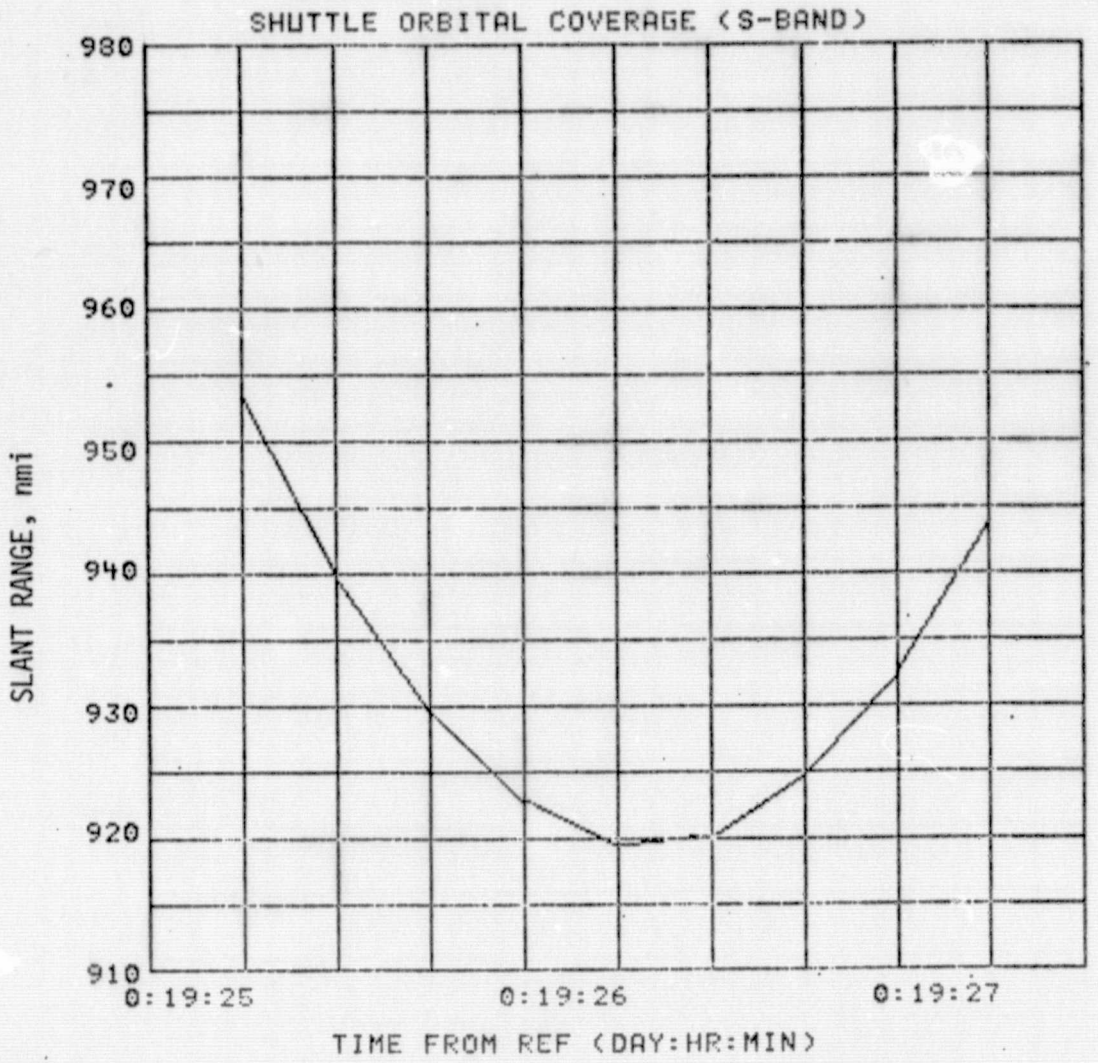


TRAJECTORY: OFT-1 ORBITAL PHASE
LAUNCH SITE: KSC; LANDING SITE: EAFB
GROUND STATION: RFI1

Figure 24. East Germany RFI Visibility of Shuttle

## 7.0 PAYLOAD INTERFACE INTEGRATION

The Orbiter avionics equipment serving attached and detached payloads perform two major functions. First, there are avionic equipment that perform payload RF signal processing and baseband signal processing functions. Second, there are avionic equipment that perform the payload data handling functions. The equipment in the first category are Payload Interrogator (PI), Payload Signal Processor (PSP), Communication Interface Unit (CIU), and Ku-Band Signal Processor (KuSP). The equipment in the second category are Payload Data Interleaver (PDI), PCM Master Unit (PCMMU), Network Signal Processor (NSP), and various DOD encryptor/decryptor units.

### 7.1 Attached Payload Communication

In the attached mode, a hard line (umbilical) provides two-way communication between the payload and the Orbiter. Scientific data, engineering data, guidance, navigation and attitude control data (GN&C), as well as caution and warning data (CW), are received by the Orbiter from the Payload.

Alternately, command data, GN&C, and uplink data are transmitted to the payload from the Orbiter.

Figure 25 illustrates the functional scientific data interfaces for attached payloads. Only limited processing, that required to throughput data to a ground terminal, is provided for payload medium-band and wideband scientific data inputs (inputs in the range of 16 kbps to 50 Mbps). For data rates below 64 kbps, the data can be routed through the PDI to the PCMMU, where it is made available to the general-purpose computers (GPC) for processing and on-board display. A payload specialist crew member may then interface directly with a specific experiment, as required. Medium-band scientific data is routed to the receiving ground terminal either via the S-band FM link or via the Ku-band system as follows:

(a) S-band FM:

Analog: 300 Hz - 4 MHz

or

Digital: 200 bps - 5 Mbps NRZ-L, or
200 bps - 2 Mbps biphase-L

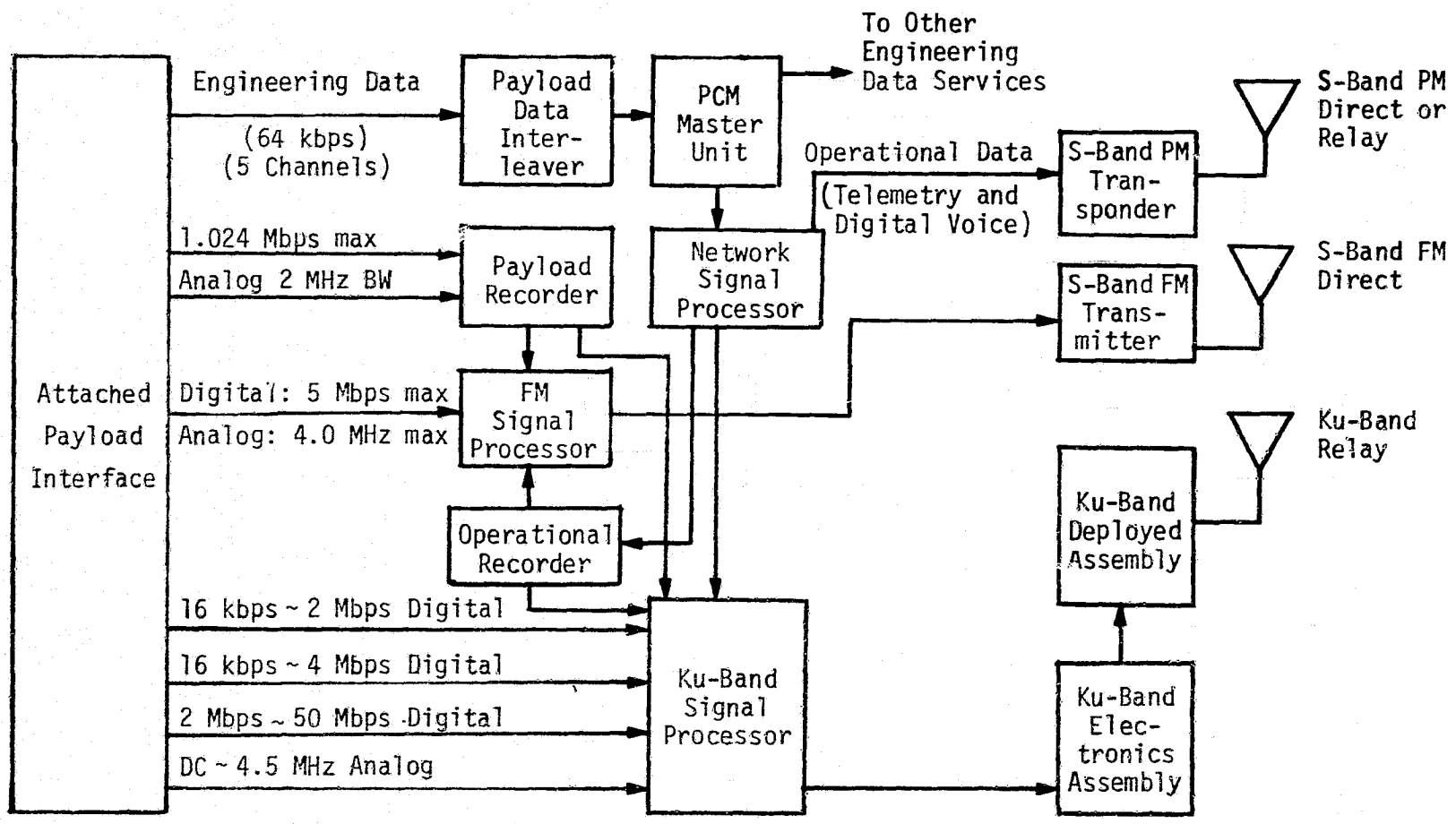


Figure 25. Attached Payload Scientific Data Interface

(b) Ku-band:

Analog: DC - 4.5 MHz BW

plus

Digital: 16 kbps - 1024 Mbps biphase-L

or

16 kbps - 2 Mbps NRZ-L, M, or S.

Wideband science data in the form of a PCM bit stream (NRZ-L, M, or S) at rates between 2 and 50 Mbps is accommodated via the Ku-band link. When operating in this mode (Ku-band Mode 1, channel 3), the input data stream is convolutionally encoded at rate 1/2 to achieve the necessary error protection on the link. The input payload data stream must be accompanied by a 1x bit rate clock, which is used to drive the encoder circuitry.

The Ku-band wideband analog channel input (DC - 4.5 MHz) can be used by payloads with unique modulation schemes or data formats as a transparent throughput channel, which provides greater data transfer flexibility and minimum Orbiter processing. Capability is constrained only by the KuSP bandwidth. Also, as discussed in Section 2.0, digital data on a subcarrier or certain other modulated digital data can be relayed using the narrowband bent-pipe mode of the KuSP.

Figure 26 depicts the Orbiter provisions for processing, displaying, and downlinking systems status data from attached payloads in support of payload monitoring and checkout functions. Data can be accessed by the Orbiter via either of two interfaces: (1) a multiplexer/demultiplexer (MDM) serial I/O channel (SIO) which makes data available directly to the GPCs for processing, display, and downlinking; and (2) one of five inputs to the PDI which makes specific parameters contained in the input PCM bit stream (0 to 64 kbps) available to the PCMMU for insertion into the operational instrumentation (OI) downlink and available to the GPCs for processing and display. The MDM SIO channel operates at a 1 Mbps burst rate and therefore is not necessarily best suited for payloads having conventional PCM data systems; however, the PDI is specifically designed to accommodate continuous PCM inputs.

Data transfers from a payload to a serial MDM channel must have a length of exactly 32 data words (16-bit word) and the sequence must conform to the following order:

(1) response header word (RHW)

(2) record ID

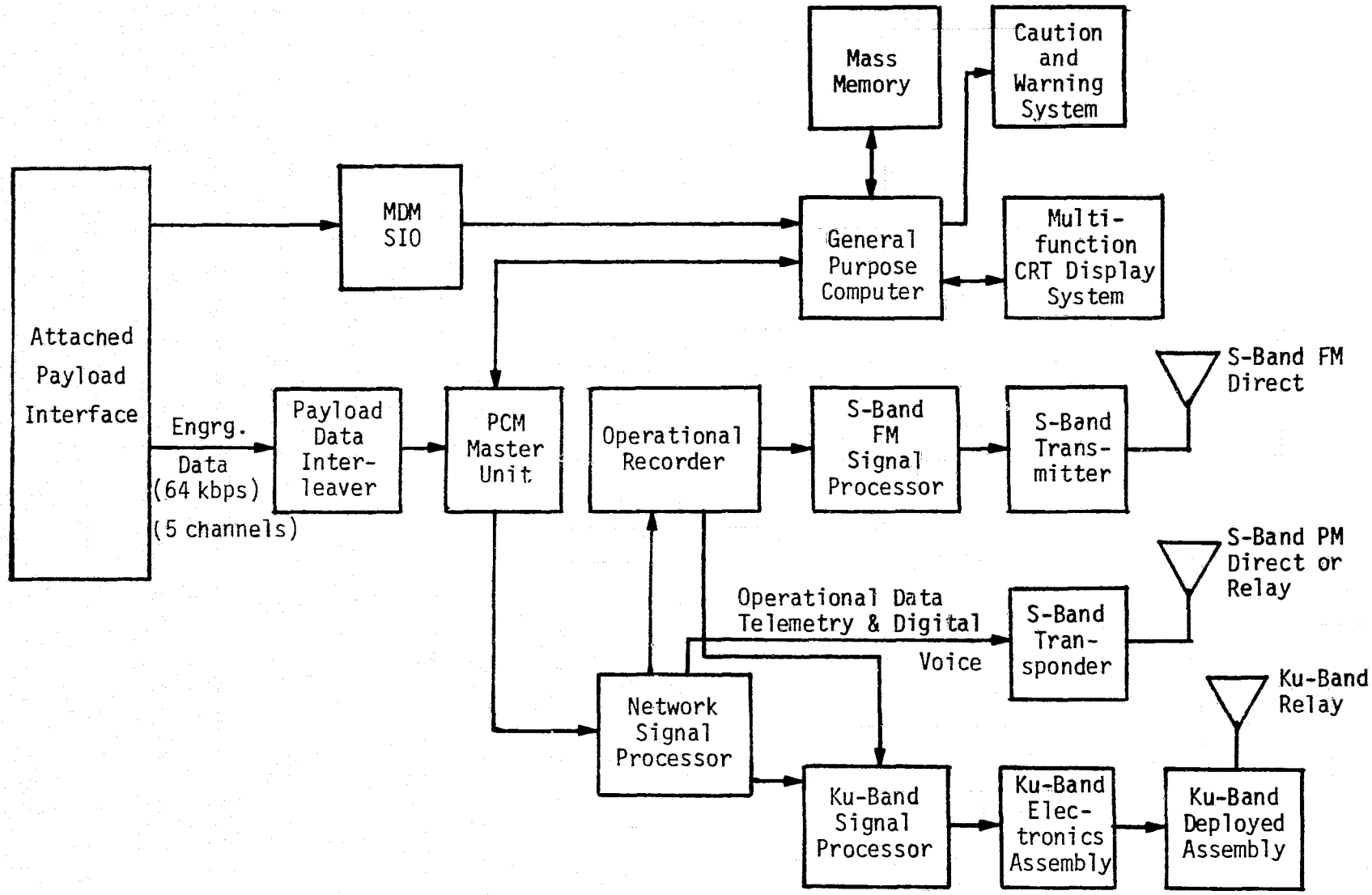


Figure 26. Attached Payload Engineering Data Interface

(3) data

(4) contents of the data words required to complete a 32 16-bit word transaction may be arbitrary.

The PDI provides the capability to receive engineering data from up to five attached payloads simultaneously. The PDI then decommutates up to four of these inputs and provides time-tagged, time-homogeneous data from these four payloads simultaneously to the Orbiter data processing subsystem (DPS) for on-board display and/or transmission to the ground via OI downlink.

In order to provide the data processing service, the input data to the PDI must be in a standard format, as follows:

- Bits per word: 8
- Words per frame: 1024 max
- Subframe rate groups per frame: 4 max
- Words per subframe: 128 max
- Frame rate: 200 per second max
- Bits per frame synchronization: 8, or 16, or 24, or 32
- Process data rate: Up to 64 kbps.

The throughput data rate (composite PDI output to the PCMMU) is limited to 64 kbps max on-orbit and 5 kbps for ascent.

A capability to throughput data which is in nonstandard format, or other unique data such as encrypted data, is also provided by the PDI. In this mode, the frame synchronization circuitry is bypassed and artificial data blocks are established to transfer the data to the PCMMU. No on-board processing or display of the data is available when operating in the nonstandard mode.

The capability for the Orbiter to provide hazards monitoring, annunciation, and control is depicted in Figure 27. Five hardwired inputs to the caution and warning electronics unit (CWE) are provided for out-of-limit sensing and annunciation at the forward flight deck panel. In addition, audible tones (siren for fire smoke and klaxon for rapid depressurization) are generated and sent to the audio central control unit (ACCU) for distribution. An additional 50 inputs (25 analog/25 discrete) are accommodated via an MDM for annunciation by the CWE, as well as fault annunciation display on the Orbiter CRT. System safing is provided via five dedicated switches located on the forward flight panel

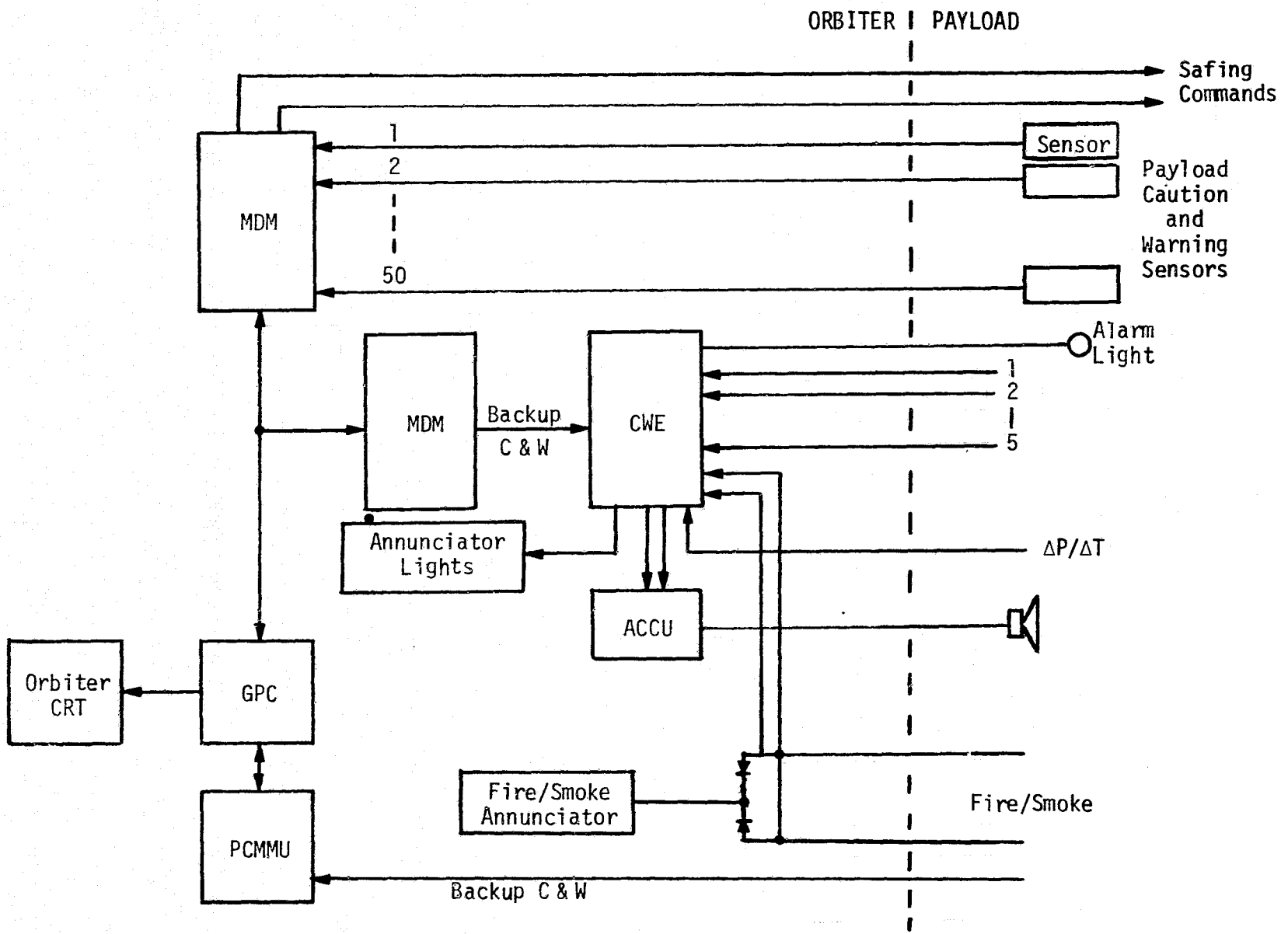


Figure 27. Attached Payload Caution and Warning Interface

or via 36 software-controlled discrete output signals available from the MDM. Backup hazards monitoring is available through the use of redundant channels or through the PDI/PCMMU interface provided for systems management data.

A capability for direct recording of certain types of payload data is provided, as shown in Figure 28. The payload recorder is a 14-track recorder capable of serial or parallel recording of digital and analog data. Data rates from 25.5 kbps to 1.024 Mbps and analog data of 1.9 kHz to 2 MHz may be recorded. A minimum record time of 56 minutes is provided at the maximum data rate. Simultaneous analog/digital parallel recording is limited to the first record pass. Subsequent passes are restricted to sequential single-channel digital record.

A total of 14 tape speeds (4 per mission) are available and selectable by on-board or ground control.

Guidance, navigation and attitude control services are provided for payloads using the interface shown in Figure 29. The Orbiter provides state vector update data words to payloads, provides target state vector update data words to payloads, receives body vector and target vector for payload pointing via Orbiter attitude maneuvers, and receives attitude errors and commanded angular rates from payload-mounted sensors for cooperative attitude control.

Orbiter state vector data can be transmitted to an attached payload at 1 Mbps clock rate via an MDM half-duplex serial channel or the PSP on a 16 kHz sine wave subcarrier at one of nine binary command data rates (125/16 bps to 2 kbps). Closed-loop pointing sensor/attitude control is provided by utilizing two half-duplex serial MDM channels.

## 7.2 Detached Payload Communication

The basic low rate data-processing/display services that are provided for attached payloads are also provided for detached or deployed payloads via S-band RF communications link between the Orbiter and payload. Figure 30 shows the interfacing hardware that supports this link. The dashed lines indicate the signal paths for detached payloads and the solid lines are attached payload paths. Note that, when the spacecraft is launched by the Inertial Upper Stage (IUS) as shown in Figure 30, the spacecraft only communicates in the attached mode through the IUS. Also,

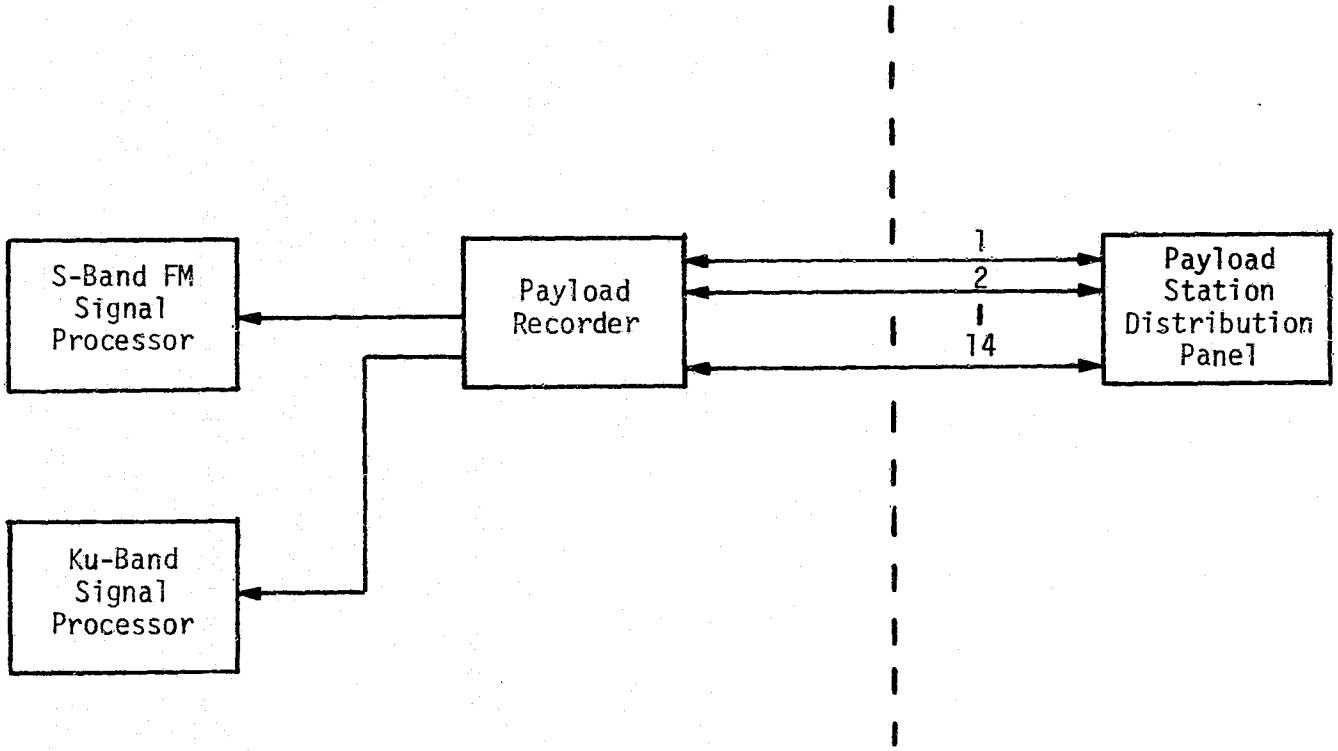


Figure 28. Attached Payload Data Recording Interface

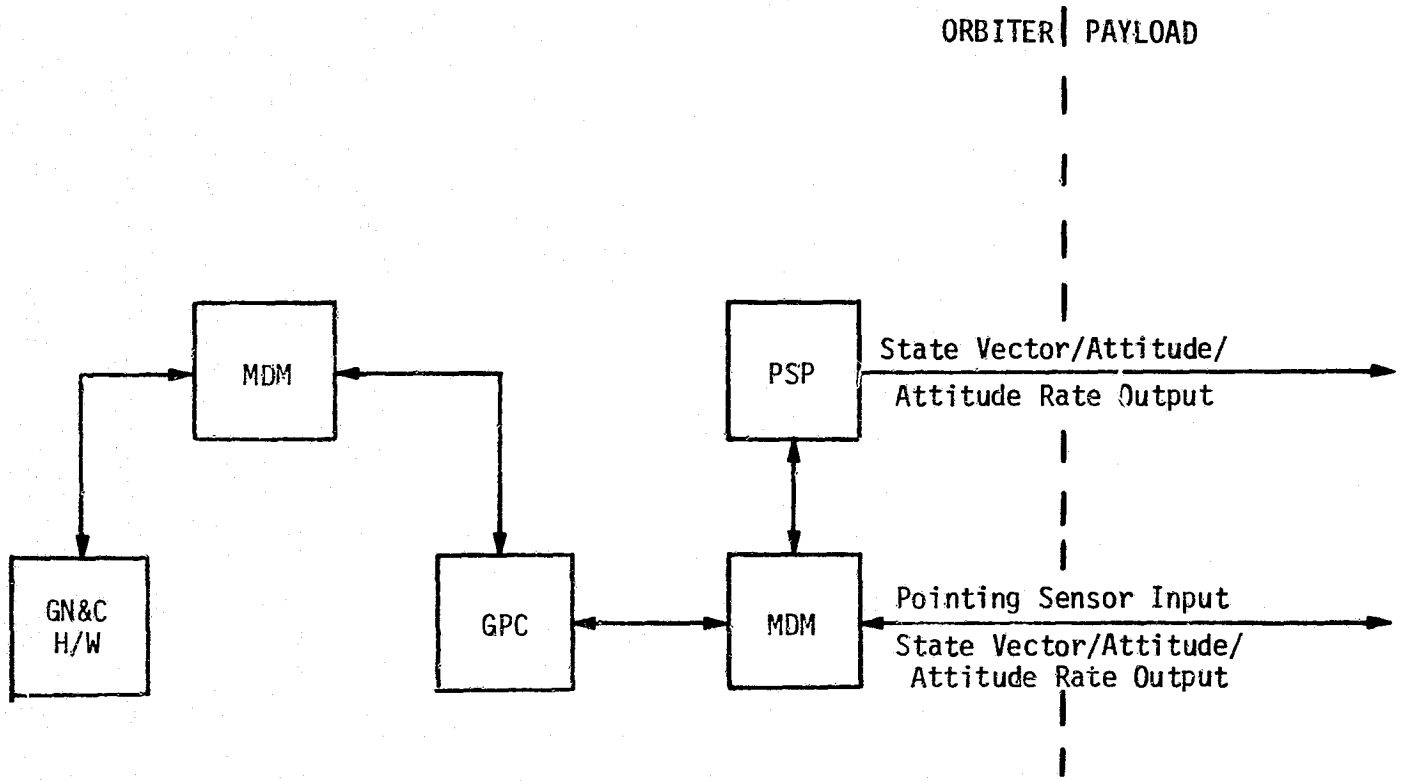


Figure 29. Attached Payload Guidance, Navigation, and Attitude Control Interface

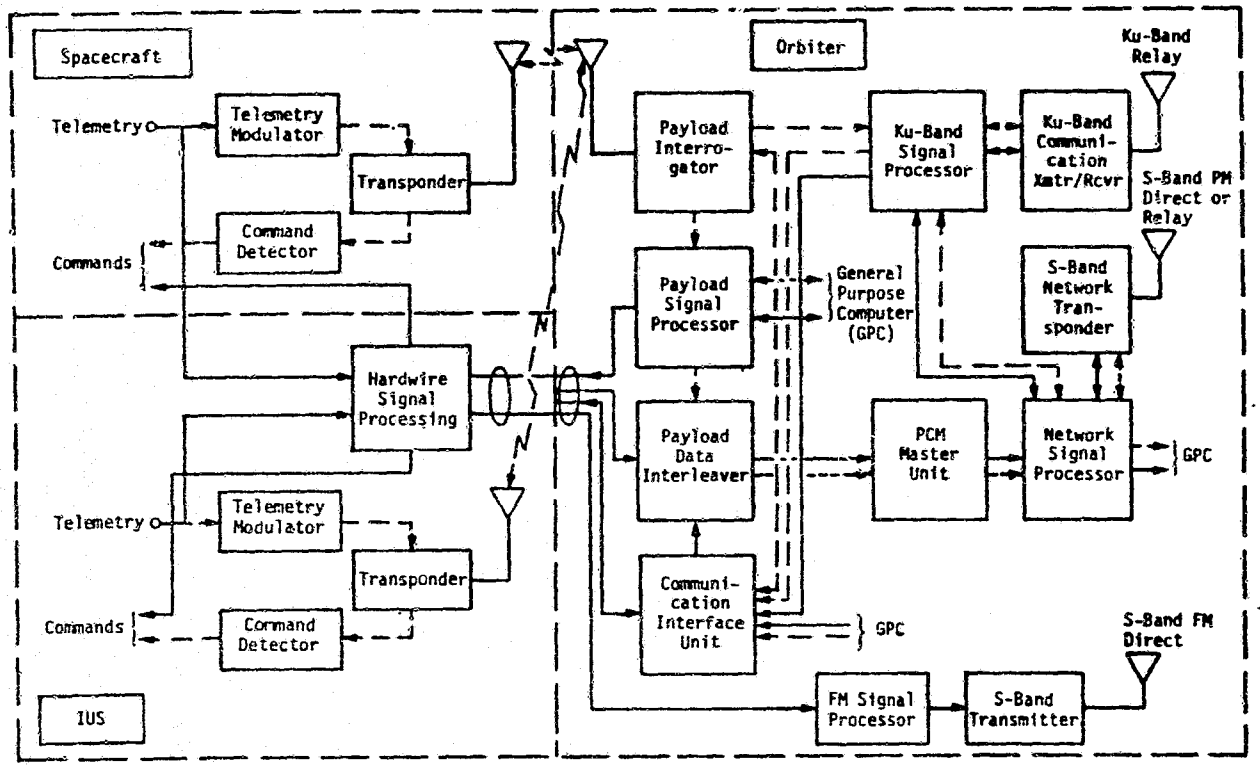


Figure 30. Payload/Orbiter Subsystems and Interfaces

note that the PI cannot communicate with the IUS and the spacecraft simultaneously.

The Orbiter S-band transceiver (PI) that supports RF communications with detached payloads is compatible frequency-wise with STDN, SGLS, and DSN-compatible payloads--capable of operating at approximately 850 selectable frequencies in the 2200-2300 MHz range.

Telemetry signals in the Orbiter standard mode of operation are routed from the PI, after carrier demodulation, to the PSP, where the data is demodulated off of a 1.024 MHz subcarrier (or a 1.7 MHz subcarrier for DOD). The data is then routed to the PDI/PCMMU/GPC for decommutation processing, display and downlinking in the same manner as for attached payloads.

Data rates that can be accommodated by the PSP in the standard mode are 16, 8, 4, 2, and 1 kbps. Processing for 256, 64, 32, 10, 0.5, and 0.25 kbps may be provided by a special DOD processor located at the payload station in the aft flight deck for DOD missions. In this mode, the PSP is bypassed. The PSP is being designed to accommodate any one of six PCM code formats in the standard mode (biphase-L, M, S and NRZ-L, M, S).

The Orbiter standard mode of operation was selected to provide a degree of flexibility of operation while minimizing basic Orbiter hardware costs. Payloads that ultimately fly on the Orbiter which are not compatible with the standard in terms of data rate or subcarrier frequency will be accommodated in a transparent throughput fashion, using a "bent-pipe" mode of operation. In this mode, the interrogator output, following carrier demodulation, is routed to the KuSP 4.5 MHz analog input channel or the 2 Mbps digital channel. These inputs are essentially limited only by the respective bandwidths and are capable of a wide range of data rate/subcarrier options (the 2 Mbps channel is limited to one subcarrier). Unique demodulation hardware at either the Ku-band ground station or the payload operation center currently must be provided by the payload requiring bent-pipe service. The bent-pipe channels are available for use by one detached payload at a time with the following capabilities:

- Digital data from 2 kbps to 2 Mbps, or
- Analog data from 2 kHz to 2 MHz, or
- Digital data from 16 kbps to 4 Mbps, or

- Analog data from DC to 4.5 MHz.

No on-board processing or display of data is available when operating in the bent-pipe mode.

## 7.3 Orbiter Avionic Equipment Serving Payloads

In order to determine that the interfaces between Orbiter avionic equipment serving payloads are compatible and that the NASA performance requirements are being met, the details of the avionic equipment were studied. This section summarizes the avionic equipment operation and capability.

### 7.3.1 Payload Interrogator

The function of the PI is to provide the RF communication link between the Orbiter and detached payloads. For communication with the NASA payloads, the PI operates in conjunction with the PSP. During DOD missions, the PI is interfaced with the CIU. Nonstandard (bent-pipe) data received by the PI from either NASA or DOD payloads is delivered to the KuSP, where it is processed for transmission to the ground via the Shuttle/TDRSS link.

Simultaneous RF transmission and reception is the primary mode of PI operation with both NASA and DOD payloads. The Orbiter-to-payload link carries the commands, while the payload-to-Orbiter link communicates the telemetry data. In addition to this duplex operation, the PI provides the "transmit only" and "receive only" modes of communication with some payloads.

Figure 31 shows the functional block diagram for the PI. The antenna connects to an input/output RF port which is common to the receiver and the transmitter of the PI unit. Because of a requirement to operate the PI simultaneously with the Shuttle/ground S-band network transponder which radiates and receives on the same frequency bands, a dual triplexer is employed. The S-band network transponder emits a signal at either 2217.5 MHz or 2287.5 MHz; both frequencies thus fall directly into the PI receive band of 2200-2300 MHz. Conversely, the payload transmitter, operating in either the 2025-2120 MHz (NASA) or the 1764-1840 MHz DOD bands, can interfere with uplink signal reception by the S-band network transponder receiver. Therefore, by use of the

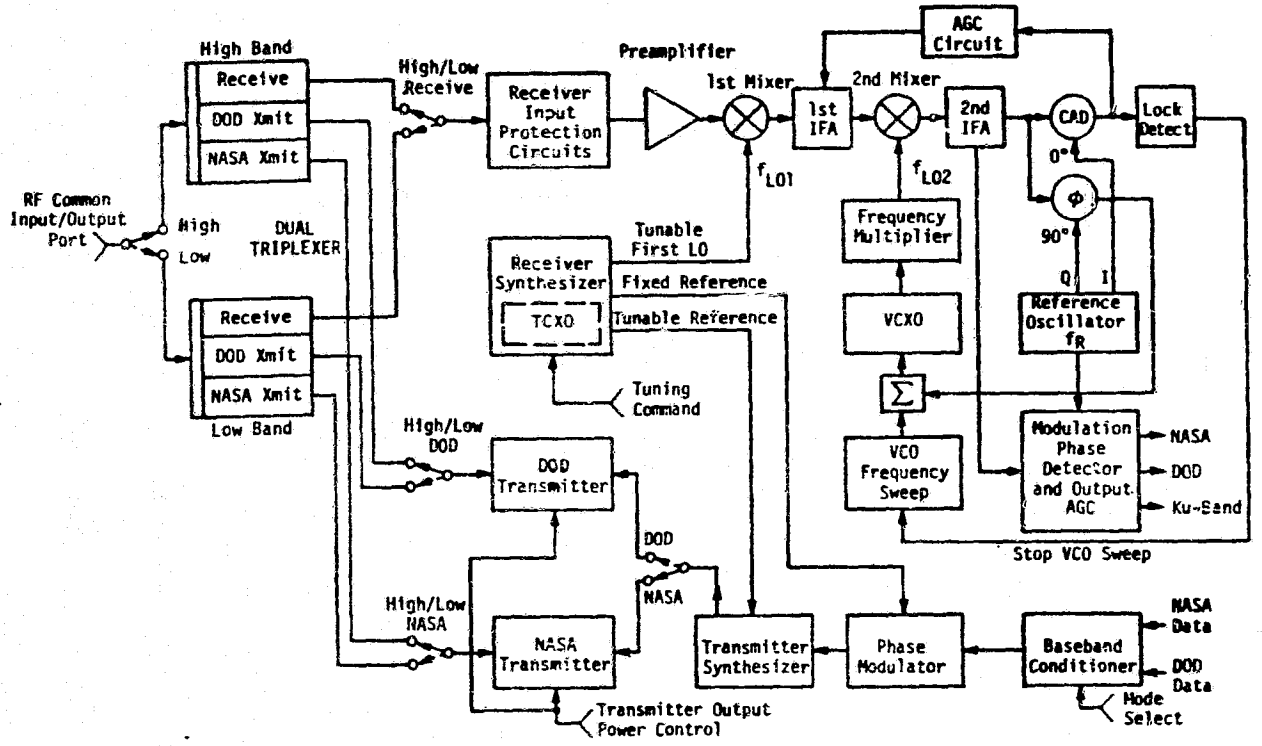


Figure 31. Payload Interrogator Functional Block Diagram

triplexer and by simultaneously operating the PI and network transponder in the mutually exclusive subbands, the interference problem is effectively eliminated.

The receiver frequency and phase tracking loop begins at the second mixer. As shown in Figure 31, the output of the first IF amplifier is down-converted to the second IF as a result of mixing with a variable second LO frequency, $f_{LO2}$. The portion of the second IF which involves only the carrier tracking function is narrowband, passing the received signal residual carrier component and excluding the bulk of the sideband frequencies. Demodulation to baseband of the second IF signal is accomplished by mixing with a reference frequency, $f_R$. The output of the tracking phase detector, after proper filtering, is applied to the control terminals of a VCO which provides the second local oscillator signal, thereby closing the tracking loop. Thus, when phase track is established, $f_{LO2}$ follows frequency changes of the received payload signal.

For the purpose of frequency acquisition, the $f_{LO2}$ may be swept over a ±50 kHz uncertainty region. Sweep is terminated when the output of the coherent amplitude detector (CAD) exceeds a preset threshold, indicating that the carrier tracking loop has attained lock. The output of the CAD also provides the AGC to the first IF amplifier.

A wideband phase detector is used to demodulate the telemetry signals from the carrier. The output of this detector is filtered, envelope level controlled, and buffered for delivery to the PSP, CIU, and KuSP.

The PI receiver frequency synthesizer provides the tunable first LO frequency and the corresponding exciter frequency to the transmitter synthesizer. It also delivers a reference signal to the transmitter phase modulator. Baseband NASA or DOD command signals modulate the phase of this reference signal which is, in turn, supplied to the transmitter synthesizer where it is upconverted to either the NASA or DOD transmit frequency and applied to the power amplifier.

For transmitter efficiency optimization, separate NASA and DOD RF power amplifier units are used. Depending on the operating band selected, transmitter output is applied to either the high-band or low-band triplexer.

### 7.3.2 Payload Signal Processor

The PSP performs the following functions: (1) it modulates NASA payload commands onto a 16 kHz sinusoidal subcarrier and delivers the resultant signal to the PI and the attached payload umbilical, (2) it demodulates the payload telemetry data from the 1.024 MHz subcarrier signal provided by the PI, and (3) it performs bit and frame synchronization of demodulated telemetry data and delivers this data and its clock to the PDI.

The PSP also transmits status messages to the Orbiter's GPC; the status messages allow the GPC to control and configure the PSP and validate command messages prior to transmission.

The functional block diagram for the PSP is shown in Figure 32. The PSP configuration and payload command data are input to the PSP via a bidirectional serial interface. Transfer of data in either direction is initiated by discrete control signals. Data words 20 bits in length (16 information, 1 parity, 3 synchronization) are transferred across the bidirectional interface at a burst rate of 1 Mbps, and the serial words received by the PSP are applied to word validation logic which examines their structure. Failure of the incoming message to pass a validation test results in a request for a repeat of the message from the GPC.

Command data is further processed and validated as to content and the number of command words. The function of the command buffers is to perform data rate conversion from the 1 Mbps bursts to one of the selected standard command rates (see Table 2). Command rate and format are specified through the configuration message control subunit.

Table 2. NASA Command System Parameters

| | |
|---|---|
| Subcarrier Frequency | 16 kHz, sinewave |
| Bit Rates | $2000 \div 2^N$ bps, N = 0,1,2,...,8 |
| $E_b/N_0$ for $P_e^b = 1 \times 10^{-5}$ | 10.5 dB |

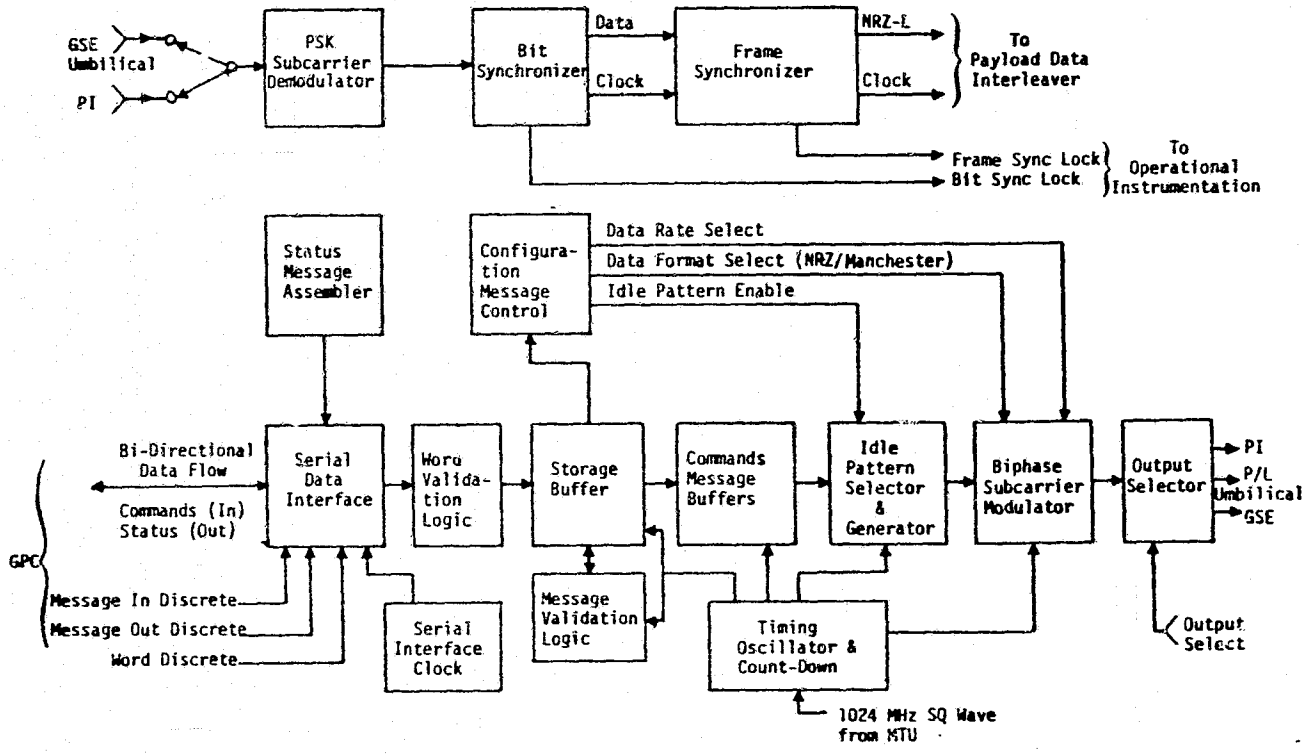


Figure 32. NASA Payload Signal Processor Functional Block Diagram

From the message buffers, the command bits are fed via the idle pattern selector and generator to the subcarrier biphase modulator. The idle pattern (which in many cases consists of alternating "ones" and "zeros") precedes the actual command word and is usually also transmitted in lieu of command messages. Subcarrier modulation is biphase NRZ only.

The 1.024 MHz telemetry subcarrier from the PI is applied to the PSK subcarrier demodulator. Since the subcarrier is biphase modulated, a Costas-type loop is used to lock onto and track the subcarrier. The resulting demodulated bit stream is input to the bit synchronizer subunit, where a DTTL bit synchronization loop provides timing to an integrate-and-dump matched filter which optimally detects and reclocks the telemetry data.

From the frame synchronizer, the telemetry data with corrected frame synchronization words and clock are fed to the PDI. The telemetry detection units also supply appropriate lock signals to the Orbiter's operational instrumentation equipment, thus acting to indicate the presence of valid telemetry.

### 7.3.3 Communication Interface Unit

The CIU, shown in Figure 33, is the DOD equivalent of the NASA PSP. The major differences are that the CIU (1) handles ternary commands in both baseband and FSK tone formats, (2) accepts Orbiter crew-generated commands, (3) permits a much larger range of standard telemetry data rates (see Table 3), and (4) is capable of simultaneously handling two subcarrier frequencies.

Table 3. Standard Payload Telemetry Modulation Characteristics

| Parameter | Parameter/Range | |
|---|---|---|
| | PSK Modulation | Frequency Modulation |
| Subcarrier Frequencies | 1.024 MHz or 1.7* MHz | 1.7* MHz |
| Bit Rates or Modulation | 256,*† 128,*† 64,* 32,* 16, 10, 8, 4, 2, 1, 0.5,* 0.25* kbps | 100 Hz to 200 kHz |
| Peak Deviation | $\pm\pi/2$ radians | ±160 kHz |
| Output Bandwidth | 400 kHz | 500 kHz |

*DOD only †1.7 MHz subcarrier only

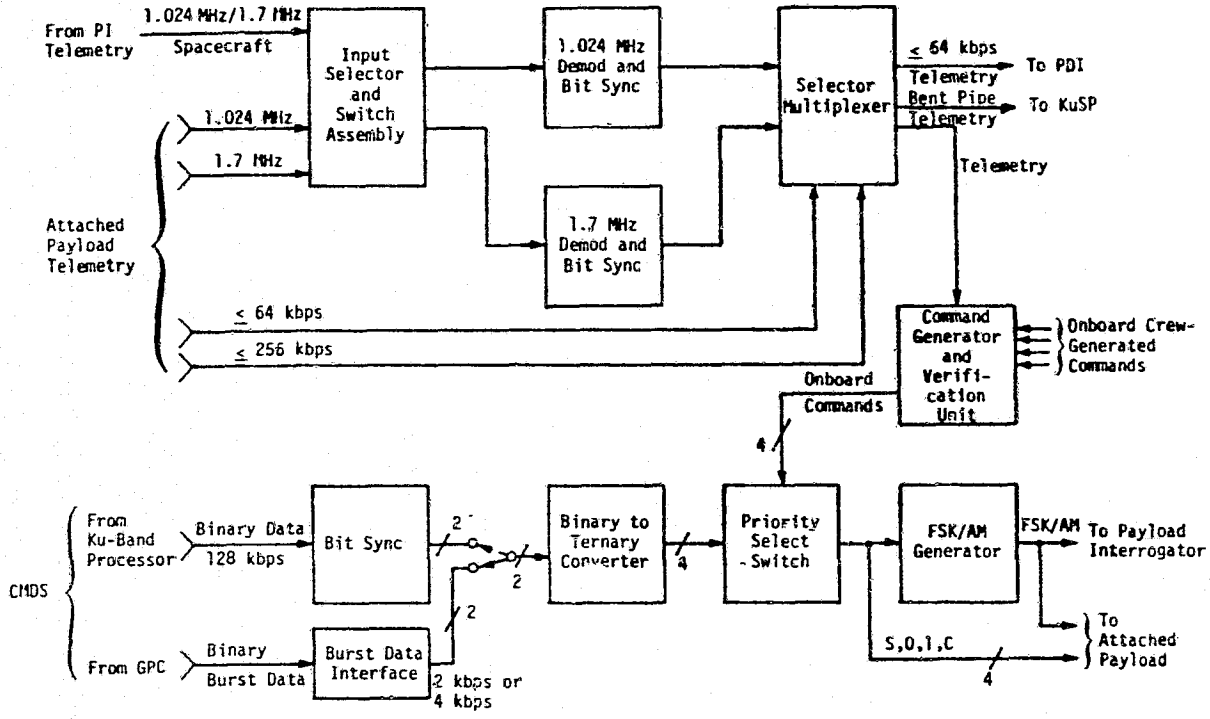


Figure 33. Communication Interface Unit for DOD Payloads

Ground-generated commands may be received from either the KuSP or the NSP (through the computer/MDM interface). Received as a continuous binary data stream at 128 kbps from the KuSP and 1 Mbps bursts from the NSP, they must be detected and buffered. The binary outputs of the buffers are either 4 kbps or 2 kbps which, when converted to the ternary format, become symbol rates of 2 ksps and 1 ksps, respectively. Input to the binary-to-ternary converter consists of serial data plus clock (two lines), and output consists of the "S," "0," and "1" symbols plus clock (four lines).

Crew-generated commands are input through the command generator and verification unit which outputs them in the proper ternary format. A priority selection switch determines whether ground or Orbiter originated commands will be transmitted to the payload. The FSK/AM generator encodes the ternary commands into the proper signal for transmission to the payload. Three subcarrier tones of 65 kHz, 76 kHz, and 95 kHz (corresponding respectively to the "S," "0," and "1" symbols) are employed in a time-serial manner. The command rate clock, at one-half the symbol rate and in the form of a triangular wave, is amplitude modulated onto the composite tone stream. Attached payloads may receive either the ternary baseband or tone command signals from the CIU.

Figure 33 shows that there are one PI and four hardline telemetry inputs to the CIU. The modulated subcarrier characteristics are indicated in Table 3. All subcarrier inputs are routed through an input selector to the two PSK demodulators. These PSK demodulators are similar to the one used in the PSP. The FM discriminator, however, demodulates the analog baseband signal from its 1.7 MHz subcarrier (see Table 3) which is, in turn, sent to the KuSP to be handled as "bent-pipe" telemetry. All demodulated/detected and hardline telemetry is routed to the selector/multiplexer where it is partially demultiplexed and sorted for reformatting to the PDI and where the command verification data from the payload is extracted for the command generator and verification unit.

### 7.3.4 Ku-Band Signal Processor

The KuSP receives payload data from the PI, PSP, PR, operational recorder (OR), and attached payload interface (API). Similarly, the KuSP transmits data to the payload via the CIU or via the NSP/GPC/PSP

(or CIU). Table 4 presents the characteristics of the data that are handled by the KuSP. The 216 kbps data shown for the forward link originates at the TDRSS ground station and can be 72 kbps command data to the NSP, 128 kbps DOD command data to the CIU, 128 kbps text and graphics data, and 216 kbps data containing 72 kbps command data plus digital voice data that is sent directly to the NSP. Figure 34 illustrates the functional processing of the KuSP for data to be transmitted to the payload (i.e., the forward link). When the forward link contains the normal S-band 216 kbps operational data of the 72 kbps command data plus digital voice data, the data mode select is set to transfer the data directly to NSP1 and NSP2 without any processing in the KuSP. Note that, in this data select position, the possible data rates are 32, 72, 96, 216 kbps. When the 216 kbps forward link data contains either text and graphics data or DOD command data, then data mode select is set to transfer the 72 kbps command data to NSP1 and NSP2. The 128 kbps DOD command data is actually either 2 kbps or 4 kbps which has been coded to use the available 128 kbps data rate without having to modify the KuSP bit synchronizer or frame synchronizer design.

The characteristics of the data that must be processed by the KuSP on the return link are quite varied, as shown in Table 4. The return link is transmitted in one of two modes which are identified by the type of carrier modulation utilized. Mode 1 implements unbalanced quadriphase-shift-keying (UQPSK) while Mode 2 implements FM. In both modes of operation, two of the channels (1 and 2) UQPSK modulate a subcarrier. Mode 1 utilizes this modulated subcarrier along with the third channel to UQPSK the carrier, as shown in Figure 35. Mode 2 linearly sums the modulated subcarrier with the third channel and frequency modulates the carrier with the resultant summed signal, as shown in Figure 36.

Channel 1 always (Modes 1 and 2) carries the operations data of 192 kbps consisting of 128 kbps telemetry data and two 32 kbps delta-modulated voice channels. Similarly, the data on Channel 2 does not change from Mode 1 to Mode 2. Channel 2 carries the output from the PR, the OR, and the PSP as well as low rate data for the API and narrowband bent-pipe data from the PI, as described in Section 2.0. The range of data rates handled by the KuSP Channel 2 is shown in Table 4 to be

Table 4. Ku-Band Signal Processor Data Characteristics

| Processor Interface | Type | Rate or Bandwidth |
|---|---|---|
| FORWARD LINK | | |
| Operations Data - NSP(1,2) | Digital | 32,72,96,216 kbps (Manchester) |
| Command/Text & Graphics - NSP (1,2) and Text & Graphics | Digital | 72 kbps Command<br>128 kbps Text & Graphics<br>16 kbps Frame Sync<br>(Manchester) |
| Command/DOD Payload Command Data - NSP(1,2)/CIU | Digital | 72 kbps Command<br>128 kbps DOD Payload<br>16 kbps Frame Sync<br>(Manchester) |
| RETURN LINK | | |
| CHANNEL 1 (MODE 1/MODE 2) | | |
| Operations Data - NSP(1,2) | Digital | 192 kbps (Manchester) |
| CHANNEL 2 (MODE 1/MODE 2) | | |
| Payload Recorder (PR) | Digital | 25.5-1024 kbps (Manchester) |
| Operations Recorder (OR) | Digital | 25.5-1024 kbps (Manchester) |
| Payload low data rate - PSP (1,2) or Attached Payload Interface (API) | Digital | 16-2000 kbps (NRZ)<br>16-1024 kbps (Manchester) |
| PI(1,2) low data rate | Digital/Analog | 16-2000 kbps (NRZ)<br>16-1024 kbps (Manchester)<br>0-2 MHz |
| CHANNEL 3 (MODE 1) | | |
| Attached Payload Interface (API) | Digital | 2-50 Mbps (NRZ) |
| CHANNEL 3 (MODE 2) | | |
| PI(1,2) high data rate | Digital/Analog | 16-4000 kbps (NRZ)<br>0-4.5 MHz |
| Attached Payload Interface | Digital/Analog | 16-4000 kbps (NRZ)<br>0-4.5 MHz |
| Video Interface Unit | Analog | 0-4.5 MHz |

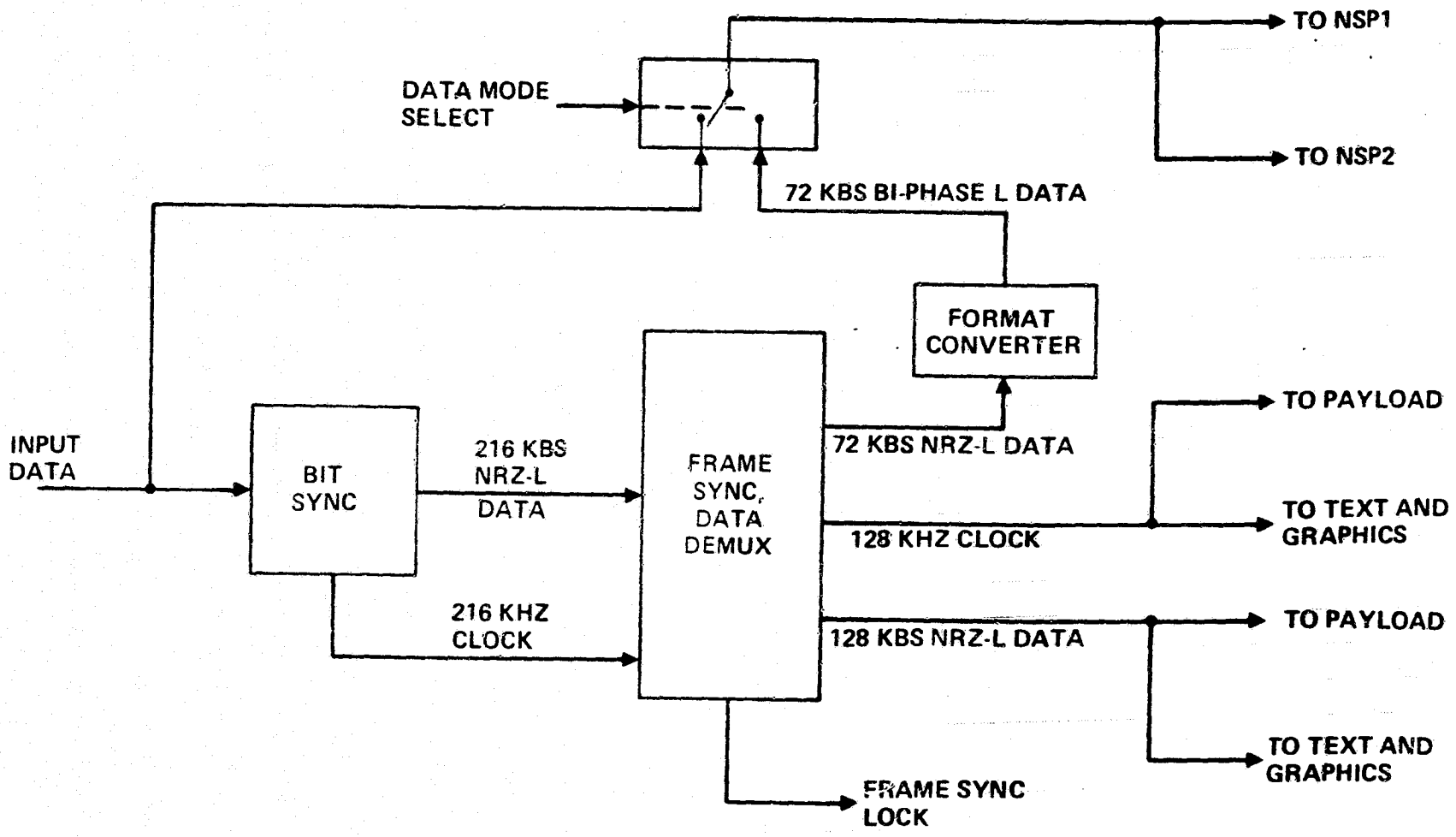


Figure 34. Ku-Band Signal Processor Forward Link Functional Block Diagram

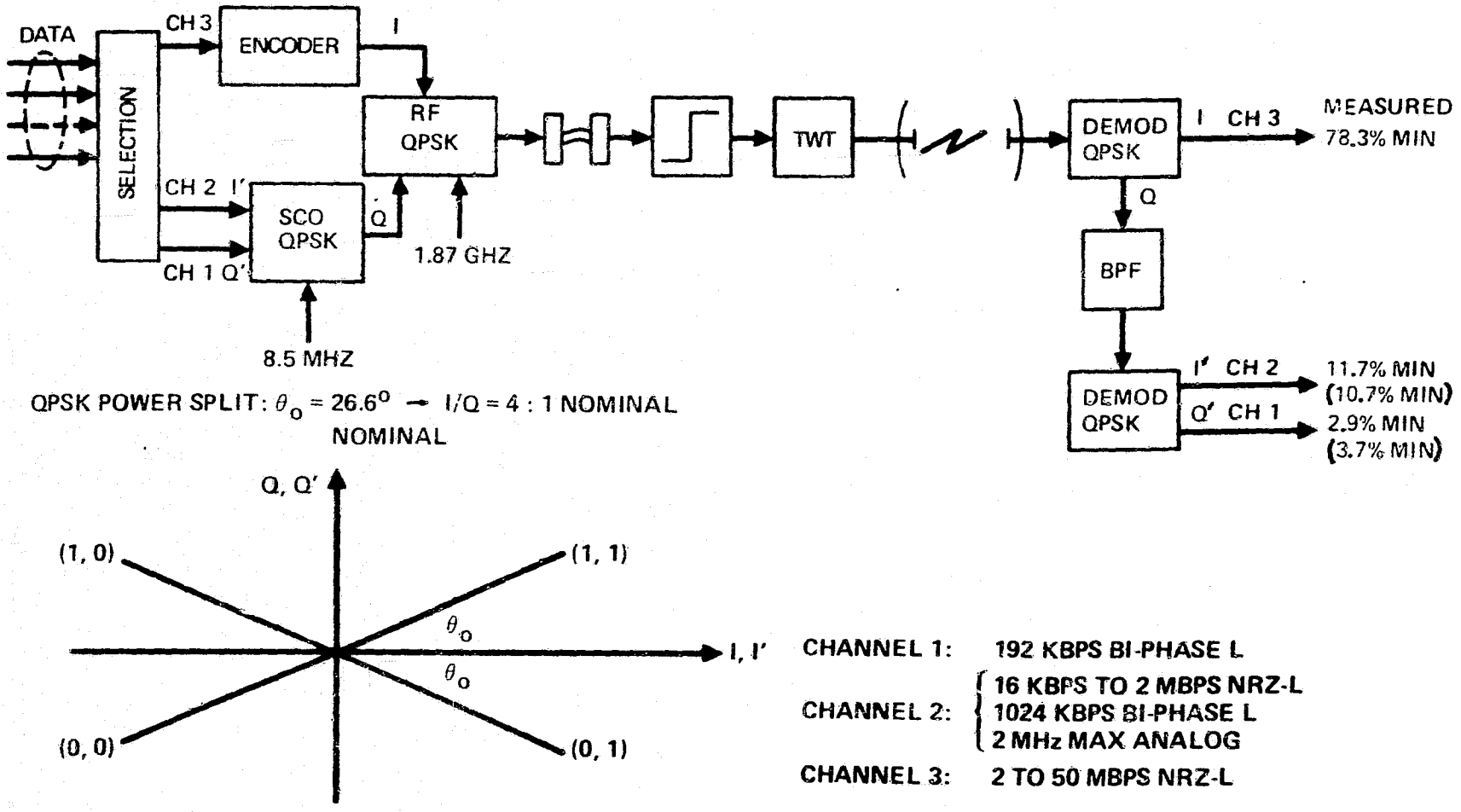


Figure 35. Ku-Band Mode 1 Three Channel Modulation

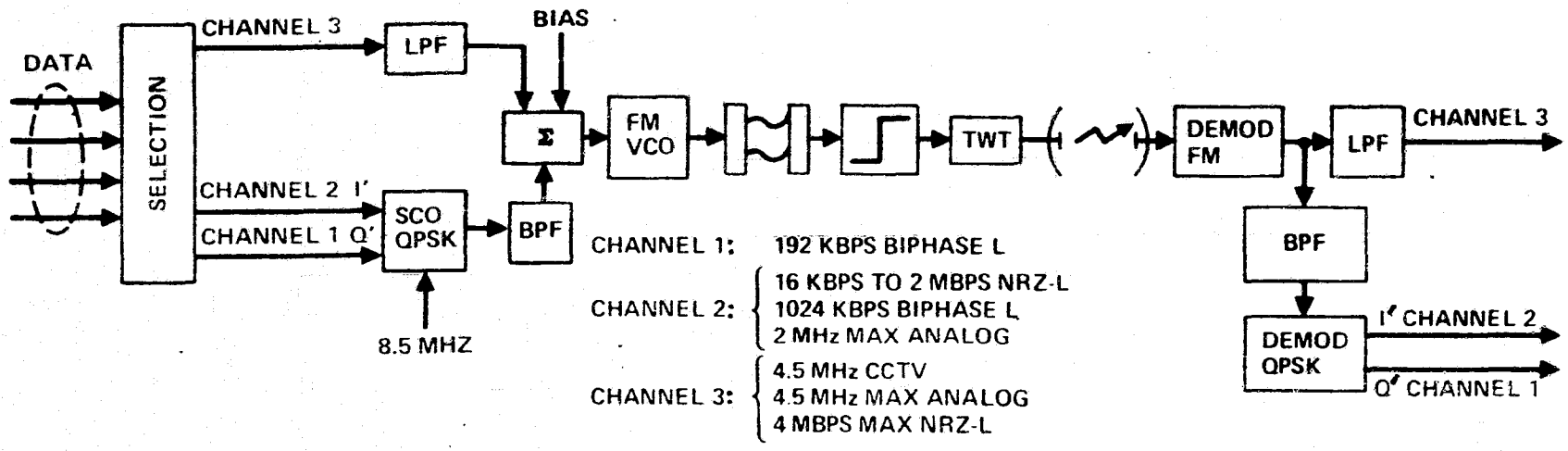


Figure 36. Ku-Band Mode 2 Three Channel Modulation

16-1024 kbps Manchester coded data, 16-2000 kbps NRZ coded data, or DC-2 MHz analog bent-pipe data.

The data carried on Channel 3 in Mode 1 is digital data of 2-50 Mbps (NRZ) which is rate 1/2-constraint length 7, convolutionally encoded by the KuSP to maintain adequate performance margin at bit error probability of $10^{-6}$. Because the output data rate of the convolutional encoder is twice the input, the input data clock must be doubled by the KuSP. The input clock is regenerated and synchronized with the input data to compensate for phase offsets and to avoid sampling the data stream near transitions. A voltage-controlled oscillator (VCO) at twice the clock frequency is divided by 2 and compared in a phase/frequency detector. The detector output locks the VCO to twice the clock frequency over the entire frequency range of 2 to 5 MHz. Use of the phase/frequency detector makes it possible to cover the 25:1 frequency range without selecting bands. To correct for asymmetry in both the clock (specified at 20 percent maximum) and data (specified at 25 percent maximum) at the KuSP input, a very symmetric clock is regenerated and used to clock the convolutional encoder. The data bits are sampled using a pulse generated every other clock pulse. The KuSP clock regeneration circuit senses the proximity of a data transition to the sample pulse and inverts the clock when the transition is within 5 nsec of the sample pulse, thus shifting the sample pulse toward the middle of the data bit. The KuSP reduces the encoder output data asymmetry to less than 10 percent for all input rates and for the input clock and data asymmetry up to their maximum specified values.

In Mode 2, the UQPSK modulated 8.5 MHz subcarrier is filtered, as shown in Figure 36, by a bandpass filter with -3 dB points at 4.75 and 12.8 MHz. This BPF has extremely sharp low frequency skirts (-40 dB point $\geq$ 4.0 MHz) to minimize spectral spillover of the modulated subcarrier into the Channel 3 frequency band (DC-4.5 MHz). The Channel 3 input is passed through a lowpass filter with specified amplitude response of -3 dB at 5.5 MHz and -20 dB at 8.1 MHz. Differential delay is no more than 20 nsec due to equalization. Although the combination of these two filters will provide excellent performance of the linear Channel 3, their selection is suboptimum for Channel 2 performance since the bandpass necessarily has a high bandwidth to center frequency ratio

and the lowpass filter provides only nominal skirt rejection. Note that the degradation to Channel 2 due to spectral spillover from Channel 3 depends on the type of data on Channels 2 and 3. The worst degradation occurs when Channel 2 is 2 Mbps NRZ digital data and Channel 3 has a flat spectrum greater than 8 MHz. Table 4 presents the type of data present in Channel 3 for Mode 2. The data with the greatest spectral bandwidth and hence the most potential degradation to Channel 2 is the 4.0 Mbps NRZ digital data, but it is unlikely that Mode 2 would be used to transmit this data. More likely, Mode 1 would be used to transmit digital data at this high rate. The analog data from the PI can range from DC to 4.5 MHz but, since the PI contains a lowpass filter with effective noise bandwidth equal to 5 MHz, it can be expected that this signal will cause little degradation to Channel 2. The video interface unit (VIU) outputs a television signal with spectral bandwidth of approximately 4.5 MHz. Here again, there will be little spectral spillover into Channel 2 and there should be little degradation. The data from the API can be either digital data from 16 to 4000 kbps or analog data with spectral bandwidth from DC to 4.5 MHz. Again, high rate digital data will probably be transmitted in Mode 1 rather than Mode 2. However, there is no filtering specified for the API; therefore, the greatest potential degradation to Channel 2 from Channel 3 is when Channel 2 contains 2 Mbps NRZ digital data and the output of the API has a larger spectral bandwidth than 4.5 MHz, resulting in significant spectral spillover. This worst-case degradation to Channel 2 is 3.3 dB. While the circuit margin on Channel 2 is large enough to allow this much degradation, the use of the three channels for a given mission should be examined to guarantee that the correct mode is selected and that the data to be transmitted will achieve the required performance on each of the channels.

### 7.3.5 FM Signal Processor

The FM-SP and FM transmitter provide a capability for transmission of data not amenable for incorporation into the limited-rate PCM telemetry data stream. The data to be transmitted via FM include television digital data from the main engines during launch, wideband payload data, or digital data from the PR or the API. The characteristics of the data and the performance specifications for the FM-SP and the FM transmitter are presented in Table 5.

Table 5. S-Band FM Performance Specifications

| FM Signal Processor | |
|---|---|
| TV Channel Input | EIA TV Standard RS 170 |
| TV Channel Gain | 19 dB ±0.8 dB to -0.25 dB |
| TV Channel Dynamic Range | 51 dB ±0.25 dB |
| Frequency Response ±0.25 dB and Phase Ripple ±1.0° | DC to 4.5 MHz |
| CCIR K Factor | <2% |
| Main Engine | |
| Data in 3 Channels | 60 kbps BPL |
| Subcarrier Frequencies | 576 kHz, 768 kHz, 1024 kHz |
| Subcarrier Modulation | ±180° at ±15° |
| Analog Data Bandwidth | 300 Hz to 4 MHz |
| Wideband Digital Data Rate | 200 bps to 5 Mbps NRZ, or 200 bps to 2 Mbps Manchester Coded |
| Recorded Data - 2 Channels Data Rate | 25.5 kbps to 1024 kbps |
| Narrowband DOD Digital Data Rate | 250 bps to 256 kbps |
| Input Common Mode Voltage (DC to 2 MHz) | 1V max |
| **FM Transmitter** | |
| Frequency | 2250.0 MHz ±0.003% |
| Output Power (into 1.5:1 load) | 10W min, 15W max |
| Deviation Sensitivity (for deviation up to ±4.5 MHz peak) | 1 MHz/V peak ±10% |
| Frequency Response ±1 dB | DC to 5.0 MHz |
| Incidental AM | 5% max over input range |
| Incidental PM | <5 kHz RMS over modulation BW |
| Intermodulation Distortion (2-tone equal amplitude) | ≥40 dB with frequency deviation ±1 MHz |

Conditioning and multiplexing for FM transmission occur in the FM-SP as shown in Figure 37. Video and wideband digital and analog signals are routed to the FM transmitter with only matching and filtering, but narrowband digital engine data are placed on subcarriers at 576, 768, and 1024 kHz.

The FM transmitter operates at 2250 MHz with an output power of 10W. Both baseband and RF filtering are provided to reduce out-of-channel interference to the PM and payload receivers. The nominal RF bandwidth is 10 MHz.

To further identify the interface between the payload system (i.e., the API and PR) and the FM-SP, Table 6 presents the requirements on the input signals to the FM-SP. As additional information concerning the processing of the data, Table 6 also presents the characteristics of the data signals output to the FM transmitter. Corresponding to each type of input signal, the signal source (i.e., API or PR) is identified. The signal type is either digital or analog with the digital data further specified by the type of data coding. Note that, for the NASA wideband payload data, the data coding can be either Manchester II (biphase-L) or NRZ-L, but the Manchester coded data is limited to data rates less than 2 Mbps rather than 5 Mbps for NRZ-L coded data. The signal level voltages are all peak-to-peak (p/p) and line-to-line for differential coupling and line-to-common for single-ended coupling. The impedance for all the signals is 75 ohms ±10%, except the recorded data from the PR which is 71 ohms ±10%. The rise and fall times for the digital data are also presented in Table 6. It is desirable to keep the rise and fall times less than 10% but, in some cases, absolute times are specified which determine the type of output drivers required at the PR, API and payload. Note that there is an additional specification of ±2% data asymmetry and ±0.1% bit jitter on the PR output signal to reduce the degradation associated with these types of signal distortions. The output of the FM-SP for the PR signal has a specification of ±0.25% bit jitter which is expected due to the multiplication of the jitter through the FM-SP buffering. Actually, each of the input signals to the FM-SP should have these specifications, but typically these are not difficult specifications to meet except from tape recorders.

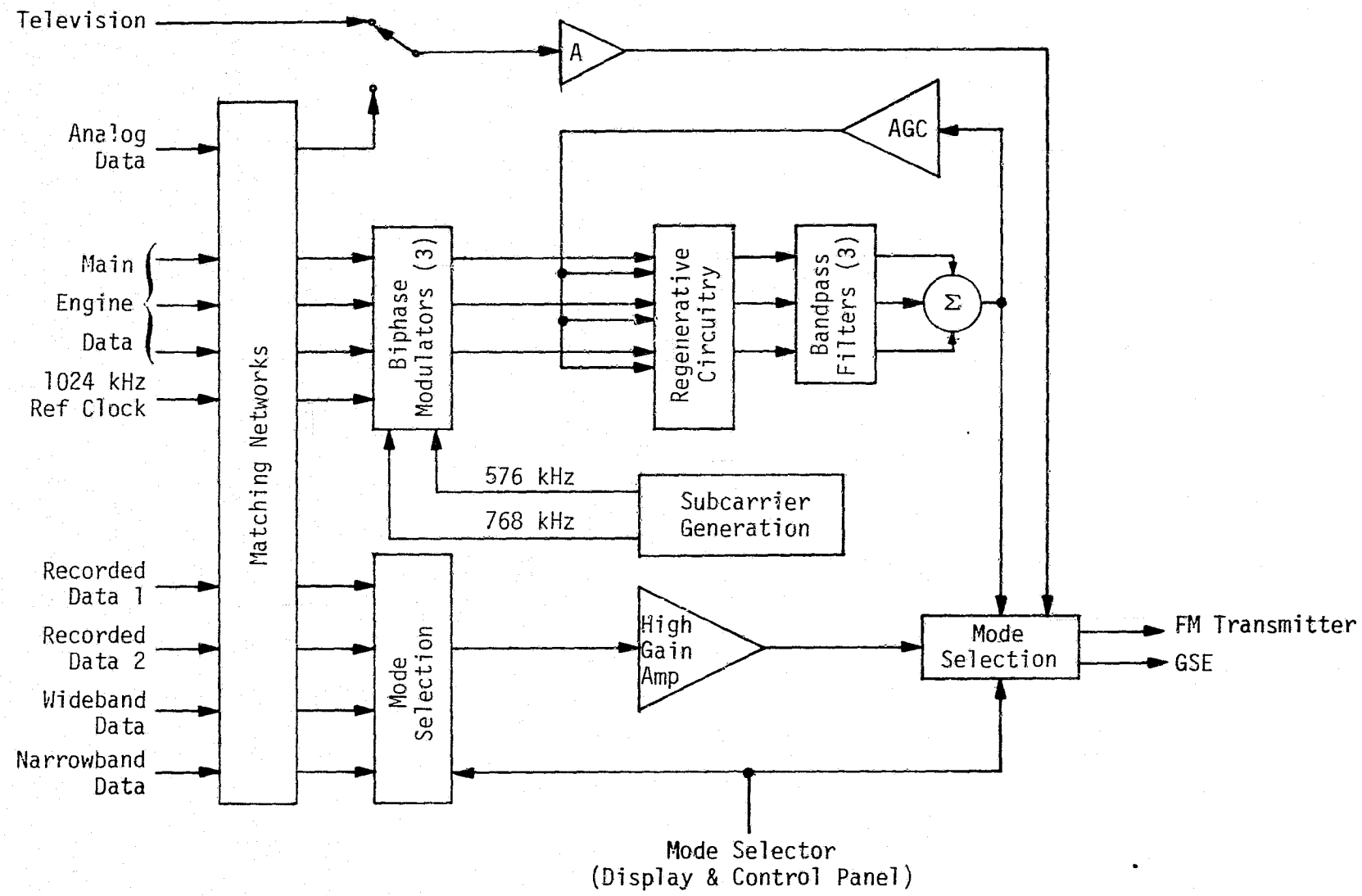


Figure 37. FM Signal Processor Functional Block Diagram

Table 6. Input and Output Signal Characteristics of FM-SP for Payload Data

| Signal | Signal Type | Data Coding | Data Rate | Signal Level | Rise/Fall Time | Coupling | Impedance |
|---|---|---|---|---|---|---|---|
| INPUT SIGNALS | | | | | | | |
| Recorded Data (PR) | Digital | Manchester II | 22.5 kbps (min)<br>1024 kbps (max) | 3-9V p/p line/line | <100 nsec<br><±2% asymmetry<br><0.1% bit jitter | Balanced Differential | 71 ohms ±10% |
| Wideband Payload (API) | Digital | Manchester II<br>NRZ-L | 200 bps-2 Mbps<br>200 bps-5 Mbps | 5V ±0.5 V p/p line/line | <50 nsec | Balanced Differential | 75 ohms ±10% |
| Wideband Payload (API) | Analog | --- | 300 Hz-4 MHz | 1V ±10% p/p line/line | --- | Balanced Differential | 75 ohms ±10% |
| DOD Payload (API) | Digital | Manchester II or NRZ-L | 250 bps-250 kbps | 1V ±0.6 V p/p line/line | <100 nsec | Balanced Differential | 75 ohms ±10% |
| OUTPUT SIGNALS | | | | | | | |
| Recorded Data | Digital | Manchester II | 22.5 kbps (min)<br>1024 kbps (max) | 1.27V ±5% p/p | 10% of bit duration;<±0.25% bit jitter | Single Ended | 71 ohms ±10% |
| Wideband Payload | Digital | Manchester II<br>NRZ-L | 200 bps-2 Mbps<br>200 bps-5 Mbps | 4V ±5% p/p | <10% | Single Ended | 75 ohms ±10% |
| Wideband Payload | Analog | --- | 300 Hz-4 MHz | 4V ±15% p/p | --- | Single Ended | 75 ohms ±10% |
| DOD Payload | Digital | Manchester II or NRZ-L | 250 bps-250 kbps | 1.27 V ±5% | <100 nsec | Single Ended | 75 ohms ±10% |

### 7.3.6 Multiplexer/Demultiplexer

The primary interface unit between the GPC and other subsystems is an MDM, shown in Figure 38. The MDMs act as a GPC-to-Orbiter format conversion unit. They accept serial digital information from the GPCs and convert or format this information into analog, discrete, or serial digital form for transfer to Space Shuttle subsystems. The MDMs can also receive analog, discrete, or serial digital information from the Space Shuttle subsystems and convert and format these data into serial digital words for transfer to the GPC. In addition, MDMs are used by the instrumentation subsystems, but only in a receive mode. Each MDM is controlled through either the primary port connected to the primary serial data bus or through the secondary port connected to the backup serial bus if failure is encountered with the primary system. The input and output of the MDM are via a multiplexer interface adapter (MIA).

The characteristics of the serial digital data input/output channels between the Orbiter subsystem (e.g., NSP, PSP, CIU) I/O buffer and the MDM are shown in Figure 39. The Word and Message Discretes are in the "0" states when the voltage level is between -0.5 V to +0.5 V and in the "1" states when the voltage level is between +4.0 V to +6.0 V. These discretes have differential signal termination with an impedance of 71 ±7 ohms and a rise and fall time between 10 and 90 percent of 100 to 250 nsec.

When the Word Discrete is switched to a logical "1" state, the Orbiter subsystem is enabled to transmit individual words to the MDM. Figures 40 through 42 present the format for individual words to the MDM. Figure 40 illustrates the overall data format and shows the various parts of the MDM word. Figure 41 presents the specifications for the data coding. Note that the burst data rate to the MDM is 1 Mbps. The first three bits of each MDM word are used for word synchronization and are different from the normal Manchester coded bits. Figure 42 presents the specifications for the nonvalid Manchester code used for word synchronization.

When the Message Discrete is switched to a logical "1" state, the Orbiter subsystem is initiated to transfer multiple words under the control of the Word Discrete beginning with the first word. Figure 43 presents the specifications for the Message Discrete and the relationship

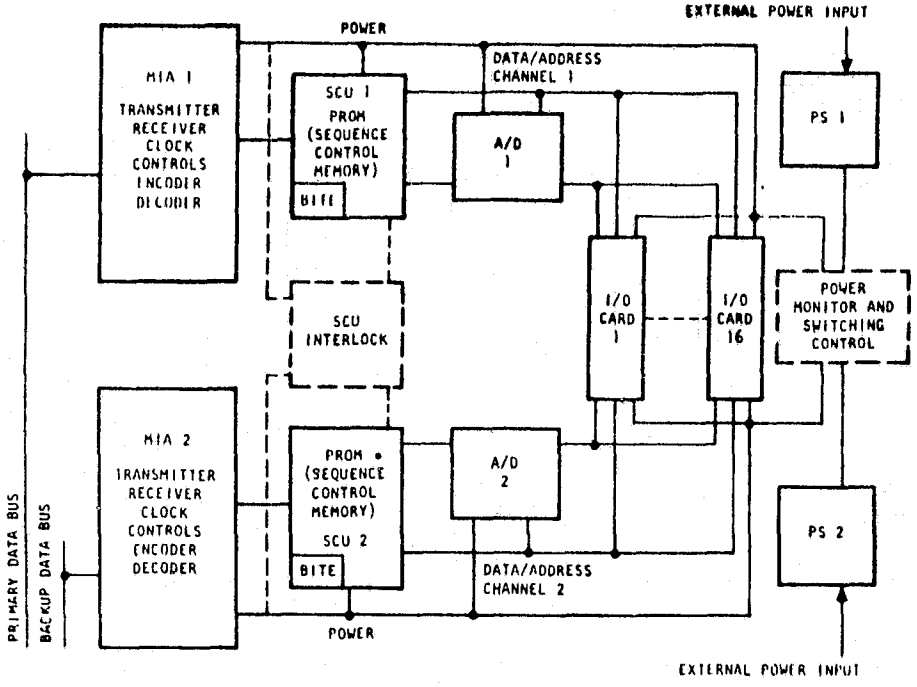


Figure 38. MDM System Block Diagram

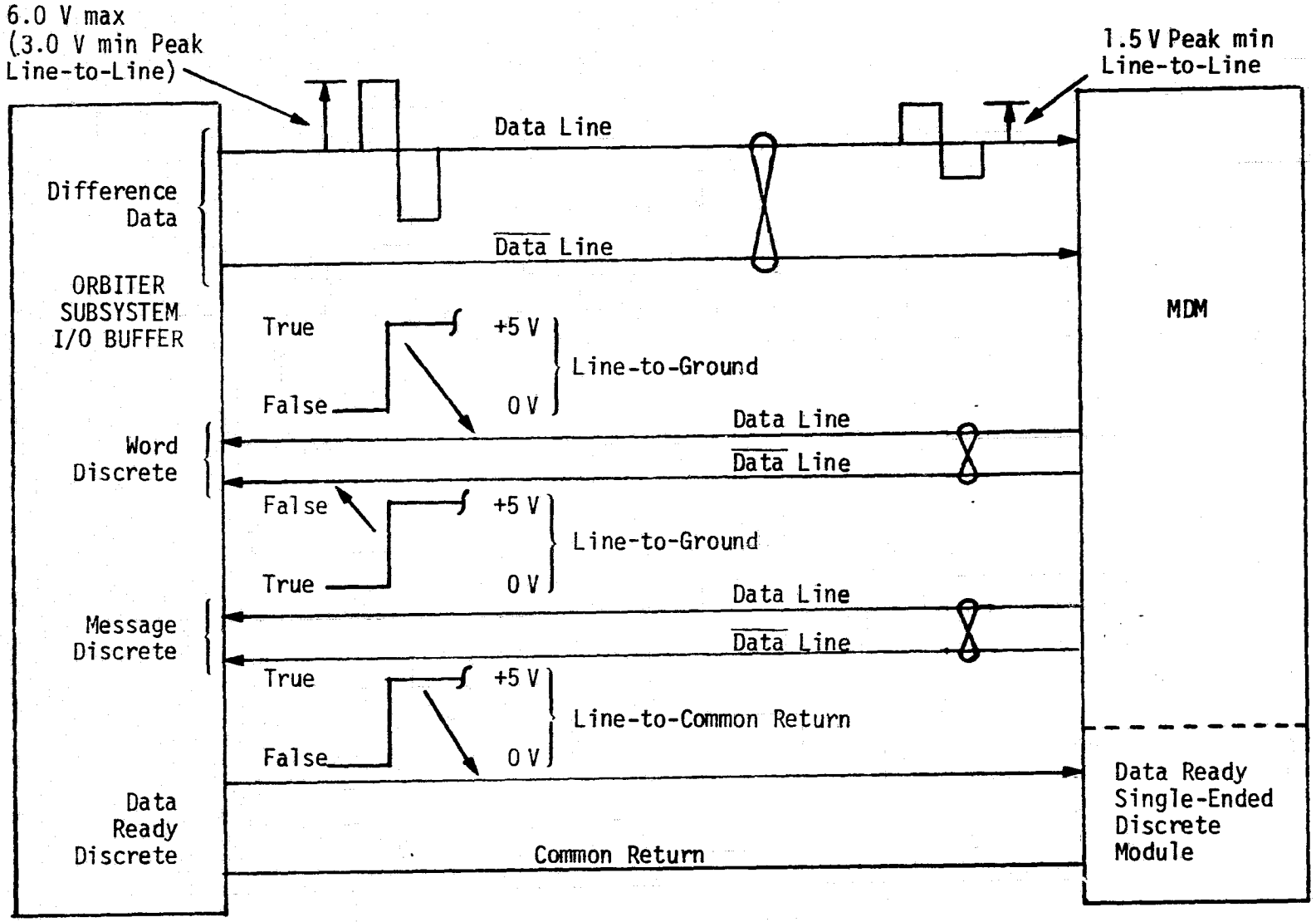


Figure 39. Serial Digital Input/Output Channel Interface

| 3 | 16 | | 1 |
|---|---|---|---|
| SYNC | SIGN OR MSB | DATA | PARITY |

Figure 40. Serial Word Format

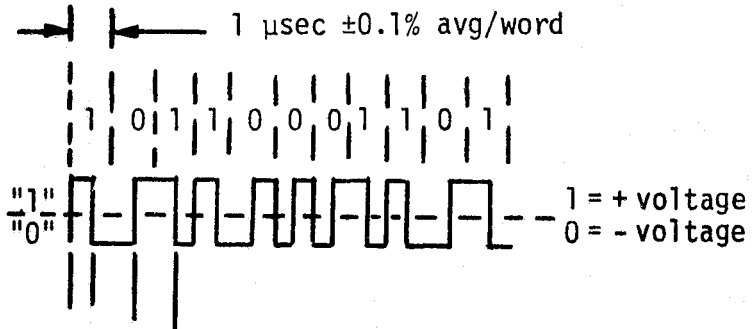


NOTE: Biphase Level (Manchester II)

"1" represented by 10
"0" represented by 01 for Data

"1" represented by 01
"0" represented by 10 for $\overline{\text{Data}}$

Figure 41. Data Code

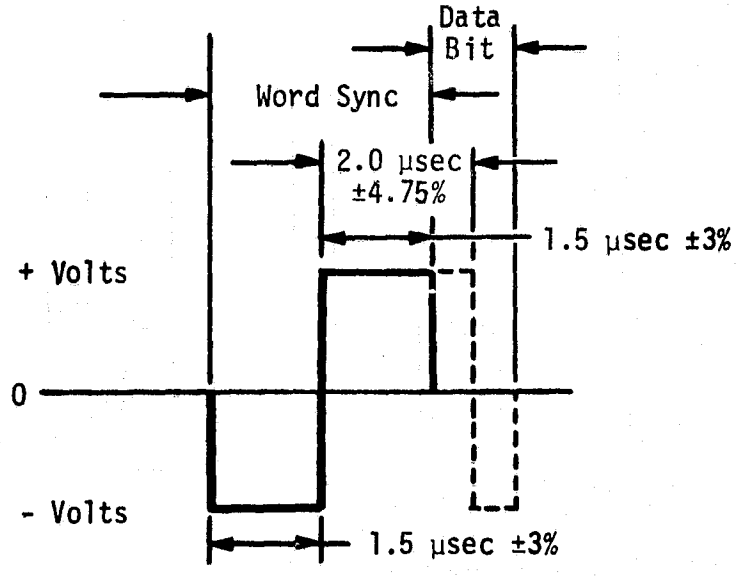


Figure 42. Data Word Synchronization, Nonvalid Manchester Code

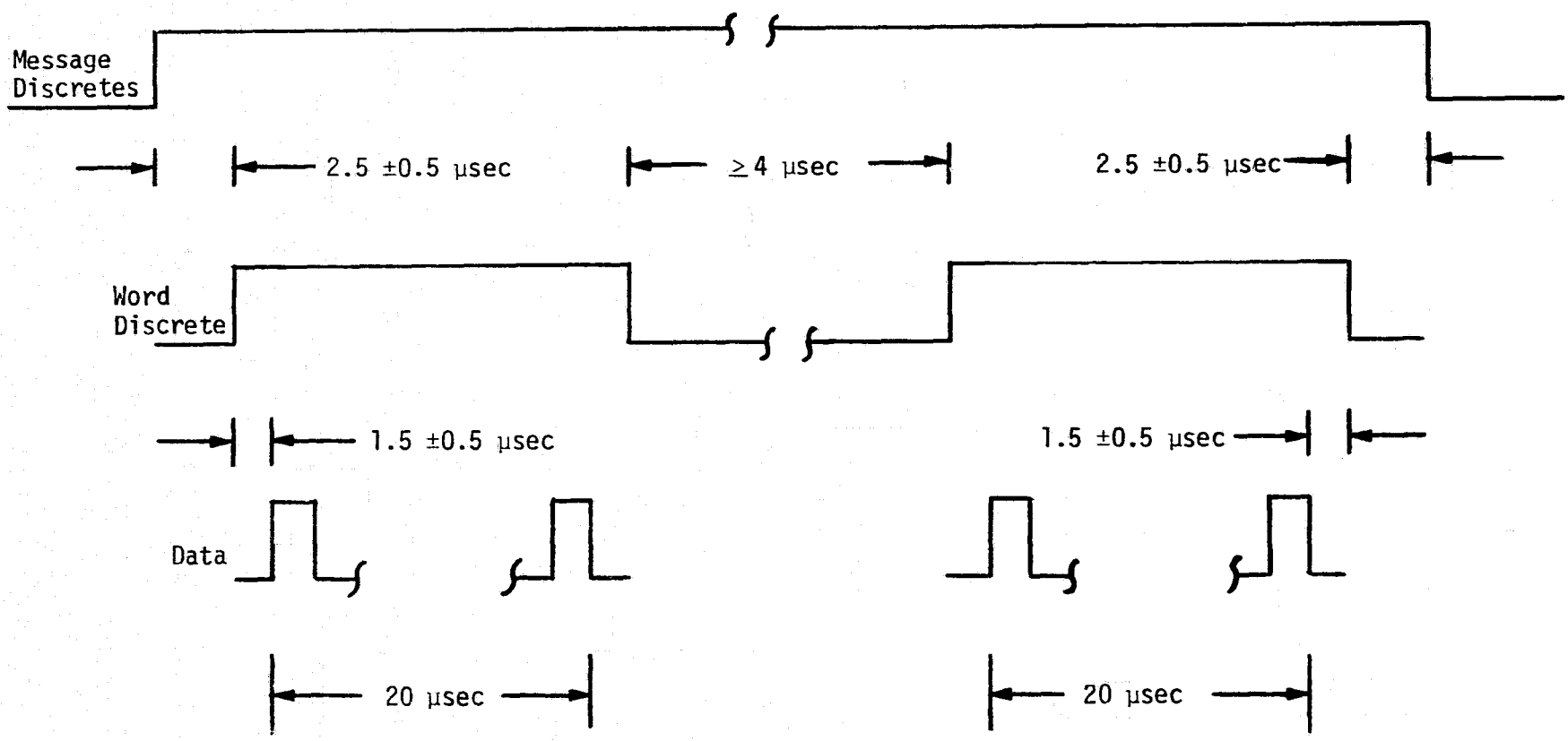


Figure 43. Serial Channel Data Transfer

between the Message Discrete and Word Discretes in the transfer of multiple MDM words.

Single-Ended Discretes are also shown in Figure 39. These discretes have the same logical state specifications as Word and Message Discretes. However, Single-Ended Discretes have rise and fall times of 20 μsec (max). The power off impedance and load impedance must be 10 kohms (max) with a line drive capacitance of 35 pf/ft (min). The corresponding input current is 2.5 mA in the "0" state and 1.25 mA in the "1" state.

The characteristics of the analog interfaces with the MDM are a voltage range of 0-5 V (peak), a source impedance of 100 ohms (max), a load impedance of 500 kohm (min), a load "OFF" impedance of 100 kohms (min) and a line drive of 35 pf/ft (min). There can be only one analog interface per return.

### 7.3.7 PCM Master Unit

The block diagram of the PCMMU is presented in Figure 44. Operational instrumentation (OI) sensor data (designated as downlink data) are acquired by the PCMMU in conjunction with MDMs. The MDMs, under control of the PCMMUs, accept, encode, and store the data in a random access memory (RAM) located within the PCMMU. The stored data are "refreshed" (updated) periodically under the control of a preprogrammed read-only memory. This module is known as a "fetch PROM."

GPC sensor and derived data (designated as downlist data) are acquired by GPCs and sent by a data bus to the PCMMUs. The PCMMU provides a unique double-buffer memory for each computer input, which allows data reception asynchronously while synchronously outputting previously received data. This guarantees the homogeneity of the data (i.e., output data are not overlaid by incoming data). Payload data are processed through the PCMMU in the same manner as the OI sensor data except that the PCMMU interfaces with a payload data interleaver (PDI).

The OI PCMMU, after accepting data from the MDM, computers, and PDI, formats the data into a serial digital output stream for telemetry, recording, and GSE. Format control is provided by the output formatter, which is programmable and can be modified by a set of instructions from the computers.

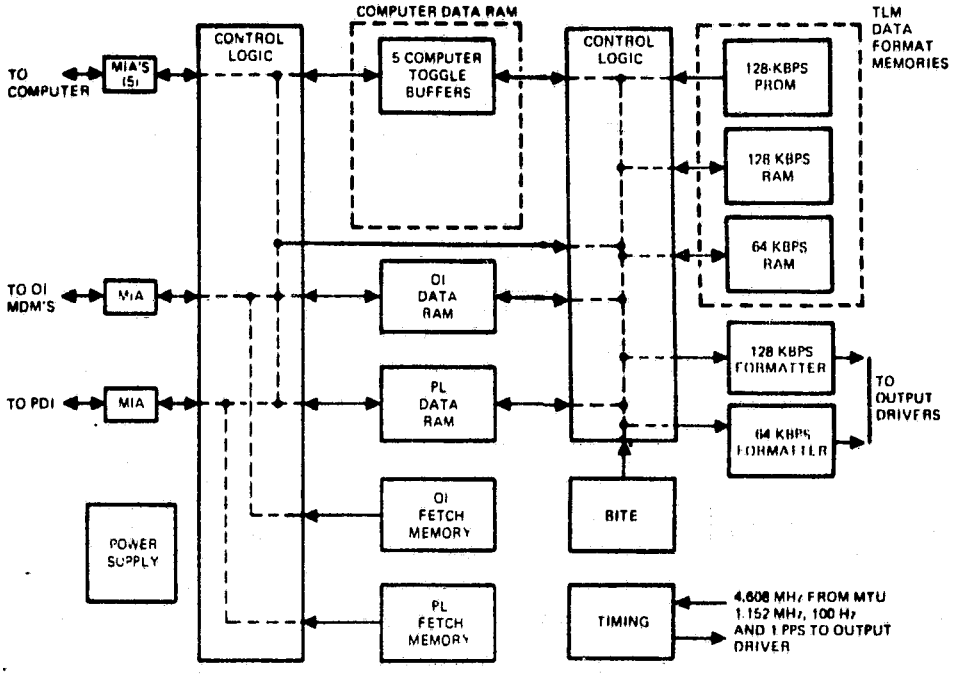


Figure 44. PCMMU Block Diagram

The PCMMU has a maximum output capability of 128 kbps for purposes of telemetry and on-board recording. The PCMMU, on command from the crew, can send 64 kbps of information. This mode is primarily used in conjunction with the low bit rate of the transmission system (S-band or Ku-band) and the TDRSS.

Formats have been developed for the ascent phase, on-orbit phase, entry phase, and ground checkout. As noted in Figure 44, one of the format memories is a 128 kbps PROM, which is a fixed format and cannot be modified by the GPC. This format is used during power-up of the Orbiter and during the ascent phase. A fixed format is necessary because loss of power to the PCMMU would result in loss of information from 64/128 kbps RAMs (volatile memory).

### 7.3.8 Payload Data Interleaver

The programmable PCMMU can be modified from one flight to the next. Since the Shuttle provides transportation for many types of payloads, a programmable PDI was designed to interface with the PCMMU. The PDI (Figure 45) can accept data simultaneously from five different attached payloads and an input from the PSP, then select and individually decommutate the data for storage in a buffer memory. This memory is accessible to the PCMMU, and the data are included with the Orbiter PCM stream. The PDI is programmed on-board from the mass memory through the GPC, which is used to select specific data from each payload PCM signal and transfer them to buffer memory locations. An input switch matrix selects four of the inputs for the bit synchronizers. The "chain" functions of bit synchronization, decommutation, and word selection are provided for up to four simultaneous PCM streams in two possible modes.

Mode 1: In this mode, a chain bit synchronizes, master-frame synchronizes, minor-frame synchronizes, and word synchronizes to the incoming data stream. The word selector blocks data into proper words for storage in the data RAM and/or toggle buffer. PCM code type, bit rate, PCM format, synchronization codes, and word selection are programmable under control of the decommutator format memories. Two word selection capabilities for this mode of operation are as follows:

Type I: The first type selects all, or a subset of, the words in a payload PCM format minor frame (or master frame for formats

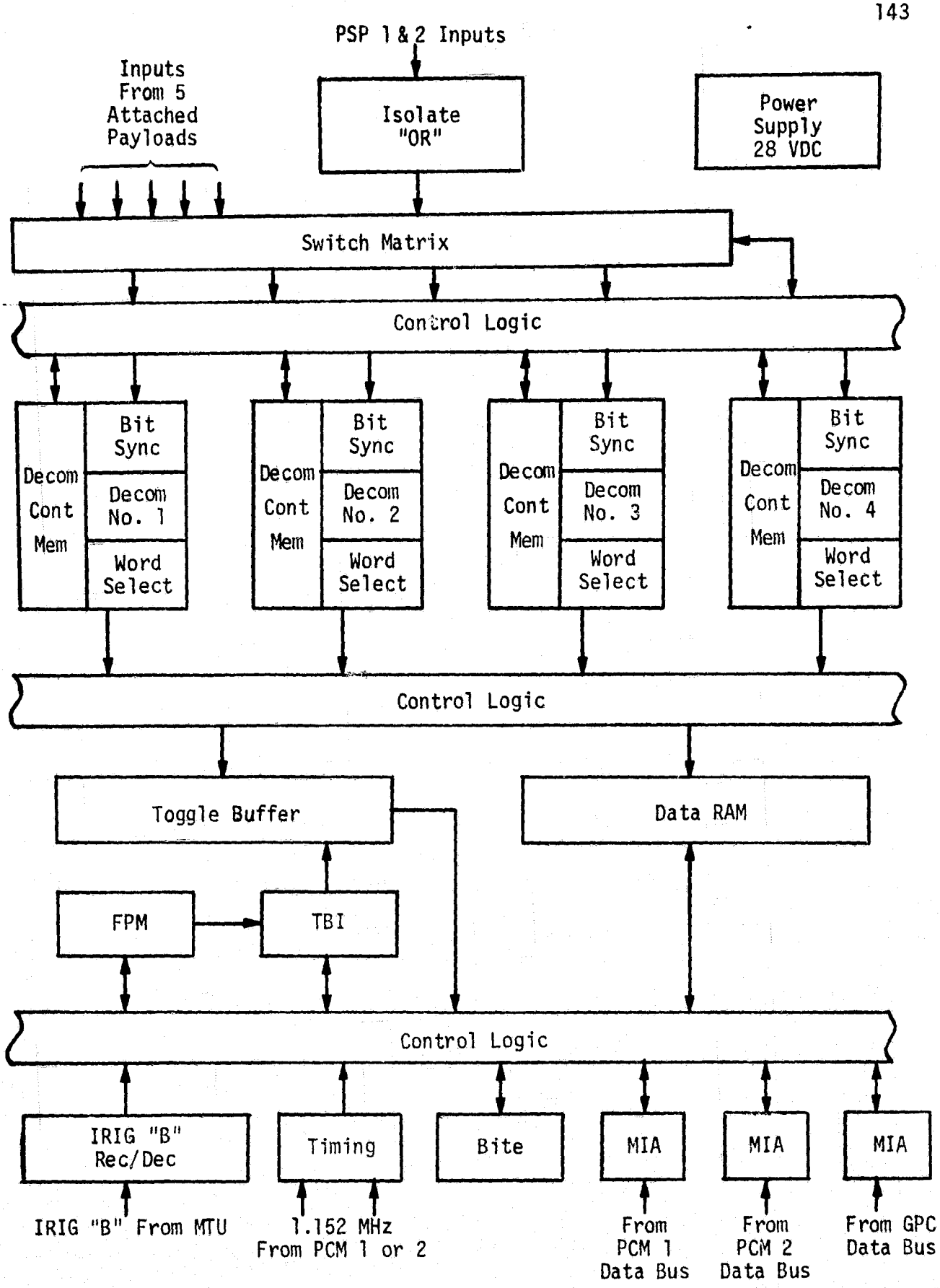


Figure 45. PDI Block Diagram

without minor frames) for storage in the toggle buffer.

Type II: The second type of word selection is by parameter. The specification of a parameter consists of its word location within a minor frame, the first minor frame in which it appears, and its sample rate. The specification is provided as part of the decommutator control memory format load.

Mode 2: In this mode, a chain bit synchronizes to the incoming data, blocks it into 8-bit words, blocks the 8-bit words into frames, supplies synchronization pattern at the start of each frame, and includes the status register as the last three 16-bit words of each frame. A homogeneous data set for this mode of operation is defined as all information within this PDI-created frame. Code type, bit rate, frame length, and synchronization pattern are programmable under control of the decommutator format memories. The frames are supplied to the toggle buffer for storage as homogeneous data sets. No data is supplied to the data RAM in this mode of operation.

A status register containing the status and time for a given chain operation is provided by the word selector to the Toggle Buffer (TB) control logic. This logic regulates access to and from the half buffers by the word selectors and the data buses. All requests for TB data by the data ports are processed through the Fetch Pointer Memory (FPM) and the Toggle Buffer Identifier (TBI). The TB control logic also partitions data from the word selector into homogeneous data sets for access by the data bus ports.

The FPM is used to identify which TB is to be accessed by a data bus port. It also allows access to any location in the data RAM by any of the PDI data bus ports at any time. FPM control logic routes all requests for TB data to the location in the FPM identified by the data bus command word. It further provides for loading and reading of formats to and from the FPM at any time by the data bus ports.

A data RAM for storage of data from the word selector by parameter is provided. The data RAM control logic steers data provided by the word selector into addresses in the data RAM specified by the decommutator control memory.

There are three data bus ports for interface with the Orbiter GPC that have read and write access into the switch matrix, the decommutator control memory, the FPM, the PDI, and the data RAM.

An IRIG "B" receiver/decoder accepts an IRIG "B" code from an external source, decodes time, and supplies it to the four status registers.

### 7.3.9 Payload Experiment Recorder

The data recording system uses wideband digital and analog magnetic tape recorders to record and reproduce digital and analog signals. The magnetic tape recorder data storage system consists of two components. The first component comprises the multitrack coaxial reel-to-reel tape transport and its associated electronics. The tape transport features negator spring tension and contains a minimum of 2400 usable feet of 0.5-inch by 1-mil magnetized tape. The transport can store a minimum of $3.4 \times 10^9$ bits of digital data. The second component contains additional data conditioning circuitry and all other control logic and associated electronics.

Payload experiment data recording is provided via the payload station panel. Predetermined patch panel wiring permits digital data recording in either parallel (up to 14 tracks) or a combination of parallel-serial. Data rates from 25.5 kbps (lowest rate for a tape speed of 6 inches per second [ips]) to 1024 kbps (highest rate for a tape speed of 120 ips) can be selected from four tape speeds provided by premission wiring of recorder program plugs.

Analog data can be recorded on up to 14 tracks in parallel with frequencies from 1.9 kHz (lowest frequency for 6 ips tape speed) to 1.6 MHz (highest frequency for 120 ips tape speed) by premission program wiring. The basic recorder has the following record/playback capabilities:

| Data Range (kbps) | Frequency Range (kHz) | Selectable Tape Speed (ips) | Time Per Track (min) |
|---|---|---|---|
| 64-128 | 1.9-250 | 15 | 32 |
| 128-256 | 3.8-500 | 30 | 16 |
| 256-512 | 7.5-1000 | 60 | 8 |
| 512-1024 | 1.5-1600 | 120 | 4 |

## 7.4 Payload Interface Issues

After reviewing the interfaces between the payload equipment and the Orbiter avionic equipment, a number of areas of concern were found. The following sections identify the major interface issues.

### 7.4.1 Payload Interrogator and Payload Signal Processor Interface

The wideband signal delivered to the PSP from the PI is to be regulated and held constant to a 2V RMS value. The current Rockwell specification adds, in addition, that a 6V peak-to-peak (3V zero-to-peak) linear transfer capability shall exist, outside of which amplitude clipping will take place. This means that any waveform having a peak-to-RMS ratio larger than 1.5 will experience amplitude limiting and will cause SNR performance loss.

Table 7 lists the peak-to-RMS values for typical complex waveforms that may be present at the PI/PSP interface. As can be seen, only the first two entries will be transferred without clipping. Since, for all possible modulations, the output of the PI for weak received signals (< -100 dBm) is essentially Gaussian in character, the output will be clipped.

Table 7. Peak-to-RMS Values of Various Waveforms

| Waveform Type | Peak/RMS Value |
|---|---|
| Square-Wave, Binary Data | 1.0 |
| Single Sinewave Subcarrier | 1.4 |
| Two Equal Amplitude Incoherent Subcarriers | 2.0 |
| Three Equal Amplitude Incoherent Subcarriers | 2.5 |
| Four Equal Amplitude Incoherent Subcarriers | 2.8 |
| Gaussian Noise | 3.0 |
| Five Equal Amplitude Incoherent Subcarriers | 3.2 |

As it is undesirable to clip Gaussian noise peaks below the $3\sigma$ level, a 12V peak-to-peak output amplifier range is required. This capability will also accommodate up to four simultaneous subcarriers without

clipping and five subcarriers with only occasional clipping. It is recommended, therefore, that the requirement be changed to provide a 12V peak-to-peak linear transfer capability.

The PI receiver PLL can be viewed as a highpass filter insofar as the demodulation of the sidebands is concerned. This can be particularly important for direct carrier (no subcarrier) data modulations of the NRZ form. Such conditions could exist for the nonstandard bent-pipe link. The requirement is that the highpass characteristics do not adversely affect the demodulated data waveform by filtering out significant waveform frequency components, nor should the data waveform introduce large tracking jitter within the PLL. This requirement must, therefore, impose specifications on minimum NRZ data rate and the maximum period of transitionless bits.

It is also desirable that the video amplifier which provides the PI receiver wideband output signal to the KuSP have a DC blocking capacitor between its output and the KuSP input. Requirement for this stems from the fact that all the circuits within the KuSP, including those of the FM transmitter, are direct coupled. Thus, any direct voltage offsets arising within the PI receiver output circuits could, without the use of AC coupling, "detune" the FM transmitter. Given that an output coupling capacitor is to be used, it is also desirable to utilize additional capacitive coupling within the PI circuits themselves. The overall net effect is to place a two-pole highpass filter between the PI receiver's wideband phase demodulator and the input to the KuSP.

Subsection 5.4. of [28] contains an analysis which establishes the proper data stream and highpass filter specifications. Direct modulation of the carrier by NRZ data should not introduce more than 10° RMS phase jitter in the PI receiver PLL, and the maximum phase reference slewing due to periods of transitionless data should not exceed 18°. For the TRW maximum PLL noise bandwidth design value of 1460 Hz, the data stream restrictions are:

(1) $R_b$ > 185 kbps, and

(2) Maximum string of nc transition bits = 30 for the bit rate of 185 kbps.

Additionally, the HPF following the PLL should not introduce any more than -0.1 dB of data power loss; therefore, the 3 dB frequency of each of the

two cascade HPFs should be less than 678 Hz. Axiomatix recommends that each of the HPF sections have a 3 dB frequency of 200 Hz.

### 7.4.2 Payload Interrogator and Ku-Band Signal Processor Interface

As discussed in Subsection 7.4.1, the PI employs an RMS regulator as an AGC on the wideband demodulated signal. Originally, this RMS scaled signal was to be output in like manner to the PSP, CIU, and KuSP. This meant that the drive signal into the Ku-band frequency modulator would always be set in proportion to its RMS value, irrespective of its waveform. Axiomatix proceeded to analyze the implications of using the RMS regulating loop for FM bent-pipe signals. Analysis which fully accounted for both noise sources in the Ku-band bent-pipe link model showed that a peak-type regulator would outperform the RMS-type regulator under all conditions and would provide a minimum overall link improvement of 1.1 dB for high data rate NRZ data. Significantly larger improvements can be expected for other qualifications.

Following several round-table technical discussions between NASA, Axiomatix and Rockwell personnel, it was concluded that any necessary signal waveform conditioning required to optimize the Ku-band FM bent-pipe link is properly a function of the KuSP rather than the PI. This conclusion was based primarily upon the fact that attached, as well as detached, payload signals must be regulated and properly scaled within the KuSP. Since the PI is not employed in the attached payload configuration, consigning such regulation to the PI for its signals would also mean that every payload would have to provide similar capability at the payload/KuSP interface. This burden, it was concluded, should not be placed on the user, and it therefore became universally agreed that such regulation and its necessary circuits should be incorporated into the KuSP. The location of the regulator in the wideband FM channel is shown as part of the selector on Figure 36. The nature of such regulation capability, however, was left open, and Axiomatix was requested by Rockwell to further review the requirements and necessary circuit designs and make recommendations. In order to avoid potential problems with tandem regulator circuits (one in the PI and the other in the KuSP), TRW was requested to review the PI receiver wideband output design so that the signal interface to the KuSP circumvents the RMS AGC circuits. The RMS regulator will therefore be used only for the PSP and CIU interfaces.

The conclusion reached by Axiomatix is that a peak-to-peak type of regulator always gives equal or superior performance compared to an RMS type regulator for all of the types of waveforms and SNR conditions that were considered. One expressed concern over a peak regulator is that such a regulating loop may be complex to implement and that proper response time/conditions may be difficult to achieve. Axiomatix has therefore initiated a program to assess what is functionally required of a signal peak regulating loop.

### 7.4.3 Commonality of Payload Signal Processor and Communication Interface Unit Functions

Functional descriptions of the PSP and CIU appear in subsections 7.3.2 and 7.3.3, respectively. As can be seen, each unit interfaces with essentially the same avionic equipment in nearly identical fashion, and internally, very similar (and some identical) functions are performed.

A review in August 1978 of the CIU interface requirements disclosed several CIU specification incompatibilities with respect to the CIU/MDM interface. Digital command data buffering and decoding by the CIU of burst inputs from the MDM proved to be the central problem. It was then suggested that, since the PSP is already designed to perform these functions, a simpler interface could be obtained between the CIU and the PSP, rather than the CIU and the MDM, and that CIU design would be simplified.

Axiomatix believes that such a change of the interface is reasonable and desirable, especially since TRW is the design and production contractor for both units. Whether this can be accomplished without significantly impacting the cost and schedule of either or both units is not clear. Some formal study by TRW should make such an assessment.

# REFERENCES


1. C. L. Weber. "Shuttle Ku-Band and S-Band Communications Implementation Study," Axiomatix Report No. R7809-5, September 30, 1978.

2. T. M. McKenzie and W. R. Braun. "Subcarrier Phase Recovery Performance in Bent-Pipe Mode of Shuttle Data Transmission," Proceedings of ITC, Los Angeles, November 1978, pp. 1097-1105.

3. J. Thomas. Introduction to Statistical Communication Theory. McGraw-Hill, 1970.

4. A. Papoulis. Probability Random Variables and Random Processes. McGraw-Hill, 1965.

5. M. K. Simon. "Output Signal and Noise Statistics of a Bent-Pipe Payload Data Processor for Shuttle Orbiter," Axiomatix Report No. R7704-1, Appendix E, April 13, 1977.

6. M. K. Simon and W. K. Alem. "Tracking Performance of Unbalanced QPSK Demodulators - Part I, Biphase Costas Loop with Passive Arm Filters," IEEE Transactions on Communications, Vol. COM-26, No. 8, August 1978, pp. 1147-1157.

7. L. Franks. Signal Theory. Prentice-Hall, 1969.

8. M. K. Simon and W. C. Lindsey. "Optimum Performance of Suppressed Carrier Receiver with Costas Loop Tracking," IEEE Transactions on Communications, Vol. COM-25, No. 2, February 1977, pp. 215-227.

9. A. J. Viterbi. Principles of Coherent Communication. McGraw-Hill, 1966.

10. I. S. Gradshteyn and I. M. Ryzhik. Table of Integrals, Series, and Products. Academic Press, 1965.

11. M. Abramowitz and I. Stegun. Handbook of Mathematical Functions. National Bureau of Standards, Applied Mathematics Series 55, June 1965.

12. "Shuttle Ku-Band and S-Band Communications Implementation Study," Axiomatix Report No. R7807-4, July 12, 1978.

13. W. C. Lindsey and M. K. Simon. "Optimum Design and Performance of Costas Receiver Containing Soft Bandpass Limiters," IEEE Transactions on Communications, Vol. COM-25, No. 8, August 1977, pp. 822-832.

14. M. K. Simon. "Tracking Performance of Unbalanced QPSK Demodulators - Part II, Biphase Costas Loop with Active Arm Filters," IEEE Transactions on Communications, Vol. COM-26, No. 8, August 1978, pp. 1157-1166.

15. A. Weinberg. "The Impact of TDRSS User and Transponder Constraints on BER, Acquisition and Tracking Performance," STI Report No. E-TR-8013, March 21, 1978.

16. R. S. Orr and L. Schuchman. "The Impact of TDRSS User Constraints Parameters on BER Performance," STI Report No. E-TR-7017, September 20, 1977.

17. M. K. Simon. "Tracking Performance of Costas Loops with Hard-Limited In-Phase Channel," IEEE Transactions on Communications, Vol. COM-26, No. 4, April 1978, pp. 420-432.

18. M. K. Simon. "False Lock Performance of Costas Receivers," Appendix J of Integrated Source and Channel Encoded Digital Communication Systems Design Study, Final Report, Axiomatix Report No. R7607-3, July 31, 1976.

19. G. Hedin, J. K. Holmes, W. C. Lindsey, and K. T. Woo. "Theory of False Lock in Costas Loops," IEEE Transactions on Communications, Vol. COM-26, No. 1, January 1978, pp. 1-12.

20. M. K. Simon. "The False Lock Performance of Costas Loops with Hard-Limited In-Phase Channels," IEEE Transactions on Communications, Vol. COM-26, No. 1, January 1978, pp. 23-34.

21. G. Hedin, J. K. Holmes, W. C. Lindsey, and K. T. Woo. "False Lock Phenomenon in Costas and Squaring Loops," Proceedings of the 1977 National Telecommunications Conference, Los Angeles, California, pp. 34:4-1 - 34:4-6.

22. M. K. Simon. "On the False Lock Behavior of Polarity-Type Costas Loops with Manchester Coded Input," Proceedings of the 1977 National Telecommunications Conference, Los Angeles, California, pp. 30:1-1 - 30:1-5.

23. C. R. Cahn. "Improving Frequency Acquisition of a Costas Loop," IEEE Transactions on Communications, Vol. COM-25, No. 12, December 1977, pp. 1453-1459.

24. M. K. Simon. "Improved Calculation of False Lock Margin in Costas Loop Receivers," Axiomatix Report No. R7803-5, March 31, 1978.

25. K. T. Woo, G. K. Huth, W. C. Lindsey, and J. K. Holmes. "False Lock Performance of Shuttle Costas Loop Receivers," Special Issue of IEEE Transactions on Space Shuttle Communications and Tracking, Vol. COM-26, No. 11, November 1978, pp. 1703-1712.

26. M. K. Simon and J. C. Springett. "The Theory, Design, and Operation of the Suppressed Carrier Data-Aided Tracking Receiver," JPL Technical Report No. 32-1583, June 15, 1973.

27. M. K. Simon. "Further Results on Optimum Receiver Structures for Digital Amplitude and Phase Modulated Signals," International Conference on Communications Record, Toronto, Ontario, Canada, June 1978, pp. 42.1.1 - 42.1.7.

28. J. C. Springett et al. "Shuttle Orbiter S-Band Communications Equipment Design Evaluation," Final Report, Contract NAS 9-15514A, Axiomatix Report No. R7901-3, January 20, 1979.